A SEARCH FOR THE EXOTIC Θ^+ PENTAQUARK IN $\gamma d \to ppK^0K^-$

By

Nathan Adam Baltzell

Bachelor of Science
University of South Carolina 2001

Submitted in Partial Fulfillment of the Requirements

for the Degree of Doctor of Philosophy in

Physics and Astronomy

College of Arts and Sciences

University of South Carolina

2009

Accepted by:

David Tedeschi, Major Professor

Ralf Gothe, Committee Member

Kuniharu Kubodera, Committee Member

Marco Valtorta, Committee Member

James Buggy, Interim Dean of the Graduate School

UMI Number: 3352781

INFORMATION TO USERS

The quality of this reproduction is dependent upon the quality of the copy submitted. Broken or indistinct print, colored or poor quality illustrations and photographs, print bleed-through, substandard margins, and improper alignment can adversely affect reproduction.
In the unlikely event that the author did not send a complete manuscript and there are missing pages, these will be noted. Also, if unauthorized copyright material had to be removed, a note will indicate the deletion.

UMI®

UMI Microform 3352781
Copyright 2009 by ProQuest LLC
All rights reserved. This microform edition is protected against unauthorized copying under Title 17, United States Code.

ProQuest LLC
789 East Eisenhower Parkway
P.O. Box 1346
Ann Arbor, MI 48106-1346

ABSTRACT

The existence of exotic hadrons not allowed by a naive qqq and $q\bar{q}$ quark model would provide an opportunity to study the strong reaction in rare form. The pentaquark state named Θ^+, with minimal constituent quark content $uudd\bar{s}$, has been predicted with a low mass of 1530 MeV/c^2 and width no larger than 15 MeV/c^2. Numerous experiments have since reported evidence of the Θ^+ in both nK^+ and pK^0 decay modes with the predicted characteristics, but the world's data is inconclusive due to limited statistics and background understanding. In this study, quasi-free photoproduction off a neutron in the reaction $\gamma d \rightarrow ppK^0_sK^-$ is exclusively measured using the CLAS detector system at Thomas Jefferson National Accelerator Facililty. Tagged photons with energies from 1.6 to 3.6 GeV are measured in concidence with $p\pi^+\pi^-K^-$ in the spectrometer. A multidimensional model based on Breit-Wigner distributions for the known background resonances is fit to the data with an unbinned likelihood method. No significant evidence of Θ^+ production is found. An upper limit on the integrated total cross section of $\gamma n \rightarrow \Theta^+K^-$ is estimated at $3.3\ nb$ with 95% confidence level.

CONTENTS

LIST OF TABLES

LIST OF FIGURES

CHAPTER 1

INTRODUCTION

The concept of indivisible particles of matter is over 2000 years old. However, it was not until almost the twentieth century that the point-like electron inside atoms was discovered. Soon after came the idea of a compact and massive atomic center, or nucleus. The interaction of negatively charged electrons orbiting around the nuclear sphere of positive charge is well described by the theory of Quantum Electrodynamics. It explains all the chemical properties of atoms and molecules and various other phenomenon involving electrically charged particles.

Like atoms, the nucleus arises only in a discrete spectrum of states. It can transition and decay between states, analagous to electronic transitions between excited atomic states, but with larger energies. The nucleus is then composed of even smaller particles. These constituents, called nucleons, are bound together by the strong nuclear force, 100 times greater than that binding the atomic electrons.

In order to understand the forces inside the nucleus, physicists built machines and detectors to study interactions between nuclei and particles. Collisions result in a spectrum of short lived excited states decaying back to the type found in normal matter, again analagous to the transitions of atoms and nuclei. In the middle of the twentieth century, the notion grew that nucleons are actually composed of truly elementary particles inside them. Physicists continue to develop models to describe their strong interaction and a variety of experimental observations.

1.1. CONSTITUENT QUARK MODEL

The categorization of the spectrum of strongly interacting particles, termed hadrons, began almost fifty years ago with the advent of the constituent quark model (CQM). Officially proposed in 1964, it is a phenomological model characterizing hadrons as bound states of elementary particles termed quarks (Gell-Mann, 1964; Zweig, 1964). All experimentally observed hadrons can be divided into two subsets: baryons, composed of three quarks (qqq), and mesons, composed of quark-antiquark pairs ($q\bar{q}$).

In the constituent quark model, the quantum numbers of the hadron arise only from those of their quarks, shown in Table 1.1, and the angular momentum due to their interactions. For example, the proton and neutron are the lightest baryons and are uud and udd configurations, respectively. The proton's charge of $^{+}1$ and isospin projection of $+\frac{1}{2}$ are just the sum of the three corresponding quark quantum numbers in the table. Ground state pions, π^{+}, π^{-}, and π^{0}, are the lightest mesons, with quark content $u\bar{d}$, $\bar{u}d$, and $u\bar{u} - d\bar{d}$, respectively.

TABLE 1.1. Characteristics of the six quarks according the world's latest estimates (Amsler et al., 2008).

Flavor	Charge	I	I_3	J^{π}	C	S	B	T	Current Quark Mass
u	$+\frac{2}{3}$	$\frac{1}{2}$	$+\frac{1}{2}$	$\frac{1}{2}^{+}$	0	0	0	0	1.5 to 3.3 MeV
d	$-\frac{1}{3}$	$\frac{1}{2}$	$-\frac{1}{2}$	$\frac{1}{2}^{+}$	0	0	0	0	17 to 22 MeV
c	$+\frac{2}{3}$	0	0	$\frac{1}{2}^{+}$	+1	0	0	0	$1.27^{+0.07}_{-0.11}$ GeV
s	$-\frac{1}{3}$	0	0	$\frac{1}{2}^{+}$	0	-1	0	0	104^{+26}_{-34} MeV
t	$+\frac{2}{3}$	0	0	$\frac{1}{2}^{+}$	0	0	0	+1	171.2 ± 2.1 GeV
b	$-\frac{1}{3}$	0	0	$\frac{1}{2}^{+}$	0	0	-1	0	$4.20^{+0.17}_{-0.07}$ GeV

The original constituent quark model approximates the three lightest quark flavors (u, d, s) as symmetric under special unitary transformations in flavor space, the $SU(3)_{flavor}$ group. In the same year of the quark model's inception, the treatment was adapted to spin $\frac{1}{2}$ quarks with $SU(2)_{spin}$ symmetry, creating a larger relationship between states of $SU(6)_{flavor-spin}$ (Gursey and Radicati, 1964). The experimental energies required to produce heavy flavors (c, b, t) was not reached until the 1970s, although predictions of heavier quarks did exist during the inception of the quark model. The CQM has been extended to

include all 6 flavors, but for the purposes of this study, it also is sufficient to limit ourselves to the three lightest flavors.

The possible states resulting from different combinations of the quark flavors can be categorized with group theory. For spinless ground state mesons, this results in 9 states from quark flavor $SU_{flavor}(3) \otimes SU_{\bar{flavor}}(3) = 8 \oplus 1$ decomposed into an octet (shown in Figure 1.1) and a singlet. For ground state baryons, the flavor decomposition is $SU_{flavor}(3) \otimes SU_{flavor}(3) \otimes SU_{flavor}(3) = 10 \oplus 8 \oplus 8 \oplus 1$ which includes the spin $\frac{1}{2}$ octet and spin $\frac{3}{2}$ decuplet in Figure 1.2 and Figure 1.3. All of these states are well confirmed.

An early success of this naive quark model, nicknamed the "Eightfold Way", was the discovery of the Ω^- in 1964 (Barnes et al., 1964a,b; Abrams et al., 1964). It was predicted two years earlier by Gell-Mann with spin $\frac{3}{2}$, strangeness $^-3$ from its sss quark configuration, and a mass of 1680 MeV (Gell-Mann, 1962).

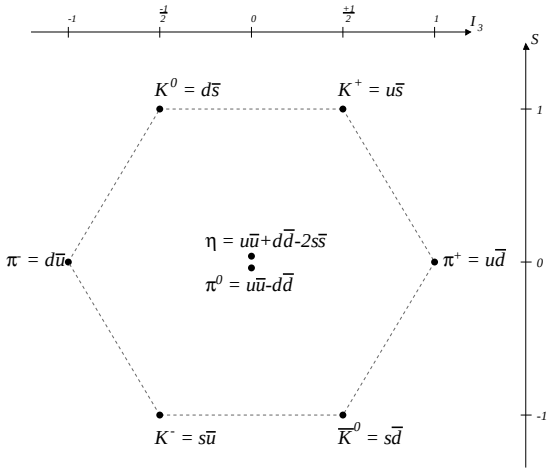

FIGURE 1.1. The ground state, spinless meson octet.

One notable problem the early naive quark model faced was the well known Δ^{++} resonance. Its spin $\frac{3}{2}$ and charge $^+2$ quantum numbers would require a bound state of three identical up-quarks (uuu) with their spins aligned. Since a ground state is expected, there is zero orbital angular momentum, and the quarks would be in identical individual quantum states. The problem is that quarks are fermions with spin $\frac{1}{2}$ and must obey Fermi-Dirac statistics. The total wave function of the state must be antisymmetric under interchange of

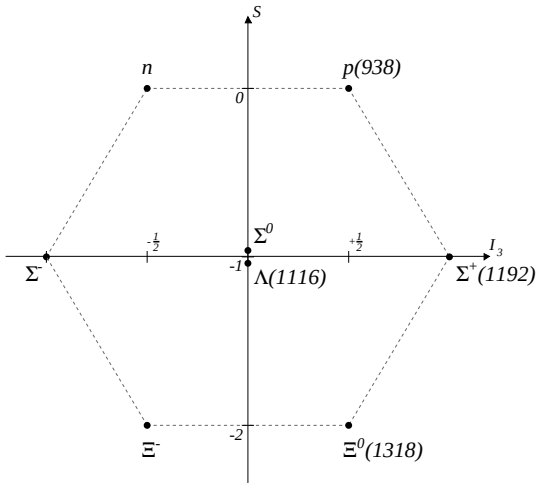

FIGURE 1.2. Octet of ground state spin $\frac{1}{2}$ baryons.

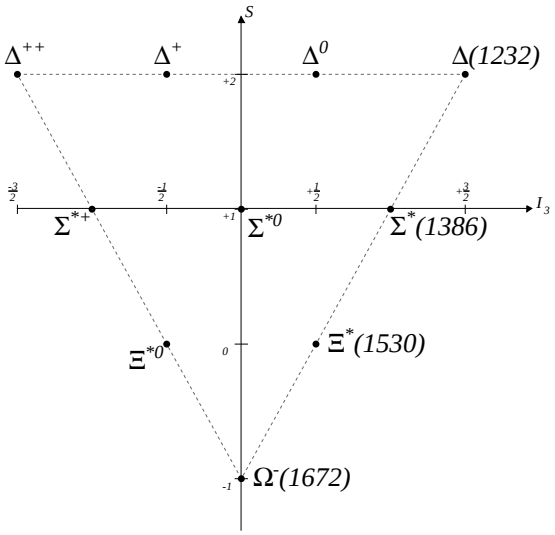

FIGURE 1.3. Decuplet of ground state spin $\frac{3}{2}$ baryons.

any two fermions, $\Psi(q_i, q_j) = -\Psi(q_j, q_i)$, yet this is not possible if any two are in the same state. In other words, the Pauli exclusion principle is violated by having two fermions in the same quantum state.

This led to the introduction of a new quantum number "color", the analog of charge for the strong force, proposed indrectly by Han and Nambu (Han and Nambu, 1965) and more explicitly by Greenberg and Zwanziger (Greenberg and Zwanziger, 1966). There are three

color states of the quark, named red, green, and blue, and their three corresponding anti-color states, proposed to perfectly obey $SU(3)_{color}$ symmtery. The three quarks can then be in the same flavor and spin states, but different color states, thus allowing an antisymmetric wave function and description of the Δ^{++} with a $u_R u_G u_B$ state.

However, without any new restrictions this leads to multiple nucleon states of different net color, something unseen in nature. To reconcile this, all observed particles are assumed to have zero net color. Color neutral mesons can be built from a quark and antiquark with opposite colors, $R\bar{R}$, $G\bar{G}$ and $B\bar{B}$, and baryons are composed of RGB or $\bar{R}\bar{G}\bar{B}$ configurations. This ad hoc introduction of color confinement is an unsatisfactory aspect of the phenomological constituent quark models.

1.2. Quantum Chromo-Dynamics

Quantum Electrodynamics describes the interactions of charged particles by the exchange of photons in the form of a renormalizable gauge field theory. Its extrapolation to the strong force in hadrons is called Quantum Chromodynamics. QCD was developed in the 1970s and is the prevailing theory of the strong interaction (Gross and Wilczek, 1973). The quanta of this gauge field theory are massless, electrically neutral, but colored gluons. The non-Abelian nature of QCD is due to the gluon itself possessing color charge, as opposed to the electrically neutral photon of QED. As a result, physical observeables can only be precisely calculated in full QCD at high energy, perturbatively, and this has inspired numerous approximations to the theory. A few general qualities of the strong force seen in nature can be derived within the framework of QCD, including the lack of free quarks or color and the observations of high energy quark jets in experiment.

The current quark masses shown in Table 1.1 do not apply to the constituent quark model where the hadron is composed only of quarks, but to the bare quark mass. In QCD, the mass of the hadron arises not only from the quark masses, but from additional interactions involving gluons. The bare mass is thus smaller than the constituent quark mass of roughly 300 MeV for u and d quarks.

Many states not fit by a qqq or $q\bar{q}$ constituent quark model description are possible in QCD. However, full calculation of the theory for even the simpler states is still not feasible. QCD can only be accurately calculated perturbatively at relatively high energies. Partially for this reason, various approximations to QCD exist to alleviate calculation problems, and efforts also continue to extend constituent quark models with various interactions in hopes of improving their description of nature.

Bag models alleviate the calculations of QCD by artificially confining the hadronic quarks to a finite region of space while still allowing relative motion and interaction with gluons. The volume of confinement is a parameter of the models and ideally should correspond roughly to the size of the hadron. Bag models can also accomodate multiquark states. It was shown initially in the late 1970s that masses and widths of many established meson staetes can be described with $q^2\bar{q}^2$ in the MIT bag model (Jaffe, 1977a,b). Similarly, ground state spin $\frac{1}{2}$ baryons were well described by a $q^4\bar{q}$ picture (Strottman, 1979). However, many more states than found in nature also emerge; such calculations predict states inherently exotic to the simpler qqq and $q\bar{q}$ configurations, including a six-quark, dihyperon state (Jaffe, 1976).

1.3. Extended Constituent Models

Almost all observed hadrons and many of their properties are well described by only qqq and $q\bar{q}$ states. Conservatively, these configurations are the most significant contributions to the total baryonic wave function. The most naive constituent model treats quarks as point-like particles that live in a mean confining potential described by a harmonic oscillator potential and do not interact with each other. Unfortunately, this approximation is much less valid than when applied to the diffuse electrons in the atom, and there it only succeeds at describing hydrogen.

The model can be extended in a variety of ways to accomodate quark-quark interactions. For example, adding to the Lagrangian a hyperfine interaction between quark spins, inspired by gluon exchange from QCD, was shown to successfully predict the masses of

$S = 0$ and $S = -1$ negative parity baryons using qqq states (Isgur and Karl, 1978). More recently, a constituent model with a flavor-spin hyperfine interaction between quarks was used to predict a stable, exotic $uudd\bar{s}$ pentaquark state with negative parity (Stancu and Riska, 2003).

Constituent models have also been extended to include extra $q\bar{q}$ pairs, which easily preserves most of the quantum numbers of the original state. Some success has been made by treating mesons as $q^2\bar{q}^2$ states via a variational approach extrapolating from known baryon-meson mass relationships (Lipkin, 1986).

Another possibility is to treat two quarks as a single entity, a diquark, interacting with the third one, reducing the problem to two bodies as opposed to three. This was done with some success as an alternative way to describe the ground state baryons in the 1960s (Lichtenberg, 1969). More recently, a diquark-triquark model was developed that employs the same aformentioned hyperfine interaction, but limits it to within the qq and $qq\bar{q}$ systems but not between. Again predicted is an exotic $uudd\bar{s}$ state, but with positive parity (Karliner and Lipkin, 2003).

Of particlar interest are the manifestly exotic states, those with quantum numbers not possible with qqq or $q\bar{q}$ configurations. The leading component of an exotic state's wave function necessarily contains more quarks, such as a tetraquark $qqqq$ or pentaquark $qqqq\bar{q}$ configuration. Such states are attractive experimentally due to the ease in proving the exotic nature of their quantum numbers. A baryon resonance with positive strangeness is necesarily exotic because it would require a strange anti-quark ($\bar{s}$); its minimal quark content is $qqqq\bar{s}$. The absence of any such baryons experimentally is another triumph, or coincidence at least, of the naive quark model's qqq configuration. Discovery of an exotic state could provide for direct study of new quark configurations and highlight different characteristsic of the strong interaction.

1.4. CHIRAL SOLITON MODEL

The soliton model was proposed before QCD in the early 1960s by Skyrme (Skyrme, 1961, 1962). It describes the nucleon as a non-trivial topological soliton of the $q\bar{q}$ pion field resulting with +1 baryon number (Witten, 1983a,b). Bound three-quark states emerge naturally from the model as rotational excitations in $SU(2)$ isospin space to describe the light baryons composed of only u and d quarks. Skyrme's model has success in describing the spectra of well known low-lying nucleon and Δ states (Karliner and Mattis, 1986; Glozman and Riska, 1996).

In the 1990's, Diakanov *et al.* extended the soliton model to the strange sector and $SU(3)$ symmetry. The result was a prediction of an antidecuplet of spin $\frac{1}{2}$ states and their masses and widths as shown in Figure 1.4 (Diakonov, Petrov, and Polyakov, 1997). A similar prediction of only their masses had been made a decade earlier (Jezabeck and Praszalowicz, 1987; Praszalowicz, 2003). The quantum numbers of the three states at the extremes of the antidecuplet are manifestly exotic, the lightest being the Θ^+ with quark content $uudd\bar{s}$ and a predicted mass of 1530 MeV. The striking difference between this prediction and previous exotic states was its narrow width of less than 15 MeV. Most models had predicted large widths for pentaquarks, as they should easily fall apart into a conventioal qqq baryon and $q\bar{q}$ meson.

1.5. DI-QUARK MODEL

Another recent prediction of exotic states comes from the diquark model (Jaffe and Wilczek, 2003). It suggests a quark system of two quark-quark pairs combined with an antiquark: $q^2q^2\bar{q}$. Each diquark is treated as a pair of highly correlated quarks, effectively a composite boson with zero spin. Then the diquarks and antiquark are combined in a naive constituent model. The result is an anti-decuplet of pentaquark states with positive parity.

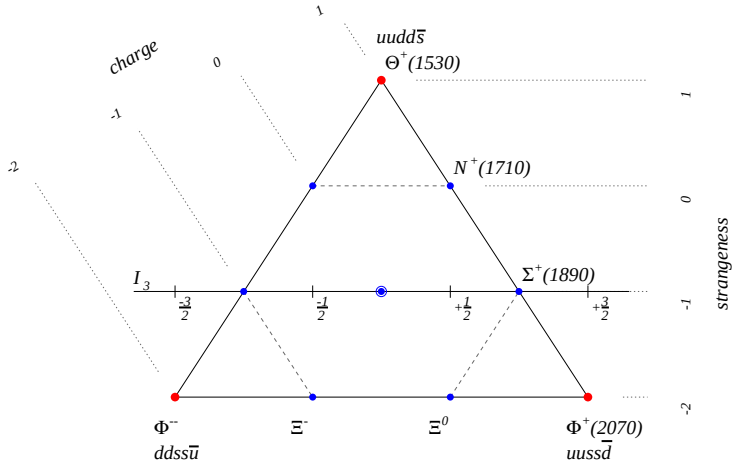

FIGURE 1.4. The predicted anti-decuplet group of $qqqq\bar{q}$ pentaquark states with $J^{\pi} = \frac{1}{2}^{+}$. Masses are shown in parentheses with units MeV/c^2. The blue states are all experimentally confirmed and can be described as a qqq baryon resonances. The three states at the extremes of the anti-decouplet are not possible with a three-quark configuration and are unconfirmed.

Most importantly, this antidecuplet again contains three states whose quantum numbers are not able to be described by three quarks alone, and are thus explicitly exotic. The lightest member is the Θ^{+}, and the authors show that a mass and width similar to Diakanov's prediction could be accomodated within the constraints of the diquark model.

1.6. EXPERIMENTAL MOTIVATION

In light of the predictions, experimental searches have been undertaken to find these exotic pentaquarks. The LEPS Collaboration first reported positive evidence in 2002 in the reaction $\gamma n \rightarrow K^{+}K^{-}n$, shown in Figure 1.5, where the target neutron is bound inside a carbon atom (Nakano et al., 2003). A narrow peak near $1.54\ GeV$ in the missing mass spectrum of the K^{-} was reported. Because the tagged K^{-} has -1 strangeness, and the initial state has none, the peak could correspond to an exotic state of $+1$ strangeness.

The CLAS collaboration followed with positive Θ^{+} sightings in the exclusively measured reactions $\gamma d \rightarrow K^{+}K^{-}np$ and $\gamma p \rightarrow \pi^{+}K^{+}K^{-}n$, shown in Figure 1.6 (Stepanyan et al., 2003; Kubarovsky et al., 2004). Another observation was reported in $\gamma p \rightarrow nK^{+}K^{0}_{s}$

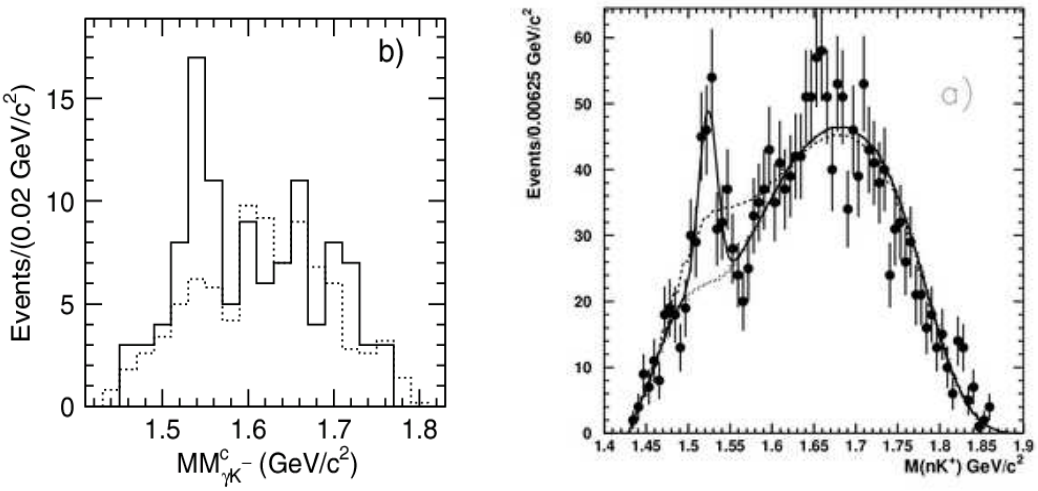

FIGURE 1.5. The LEPS Collaboration's original 2004 publication of $\Theta^+ \rightarrow nK^+$ evidence from (Nakano et al., 2003) (left), and their higher statistics 2009 result (right) with a reported significance of 5.1σ and differential cross-section of $12 \pm 2\ nb/sr$ (Nakano et al., 2009).

by the SAPHIR collaboration (Barth et al., 2003). All of these concern the same nK^+ decay mode of the Θ^+.

Assuming isopsin symmetry, the strong decay of $\Theta^+ \rightarrow NK$ should not favor one of pK^0 or nK^+ over the other. Sightings in the pK^0 decay mode have also been found. Notably, in K^+Xe collisions by the DIANA collaboration (Barmin et al., 2003) and in neutrino-nuclei collisions the ITEP collaboration (Asratyan, Dolgolenko, and Kubanstev, 2004).

Numerous analyses around the world using previuosly acquired data sets have since been performed, but the situation to date elicits verification. It was proposed that the positive sightings are artifacts of intereference, kinematic reflections of known resonances, or spurious ghost tracks in the detector due to tightly correlated kinematics (Dzierba et al., 2004). Furthermore, relating the results, positive and null, is not simple due to differing production mechanisms and kinematic regimes. That not all experiments can report results in terms of cross sections makes comparison even more difficult. Overviews of the situation have been published in the literature (Hicks et al., 2005; Dzierba, Meyer, and Szczepaniak,

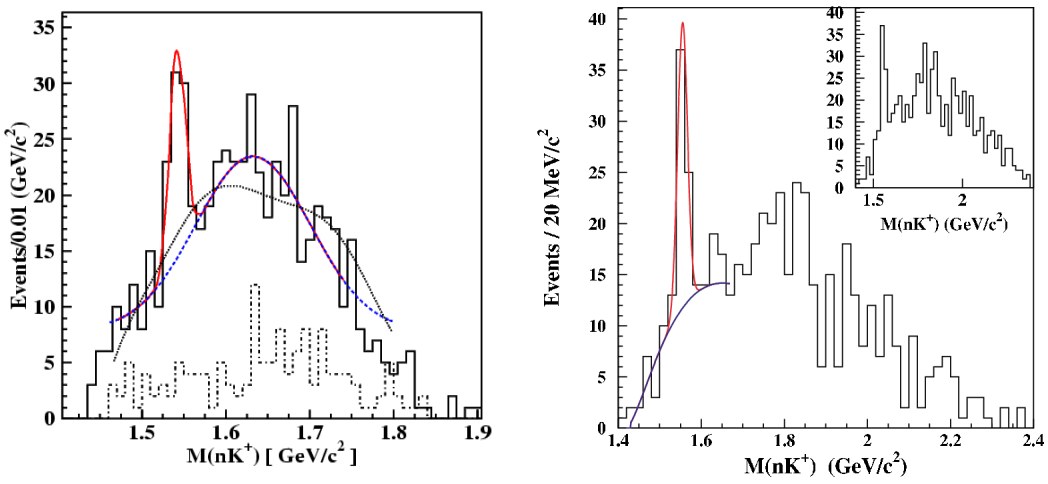

FIGURE 1.6. The nK^+ invariant mass spectra as reported by the CLAS Collaboration in the reactions $\gamma d \to K^+K^-np$ (left) and $\gamma p \to \pi^+K^+K^-n$ (from (Stepanyan et al., 2003; Kubarovsky et al., 2004)). The reported significance of the two signals was 5.8 σ and 7.8 σ respectively.

2005), and a reformatted picture of some of the positive Θ^+ sightings is shown in Figure 1.7.

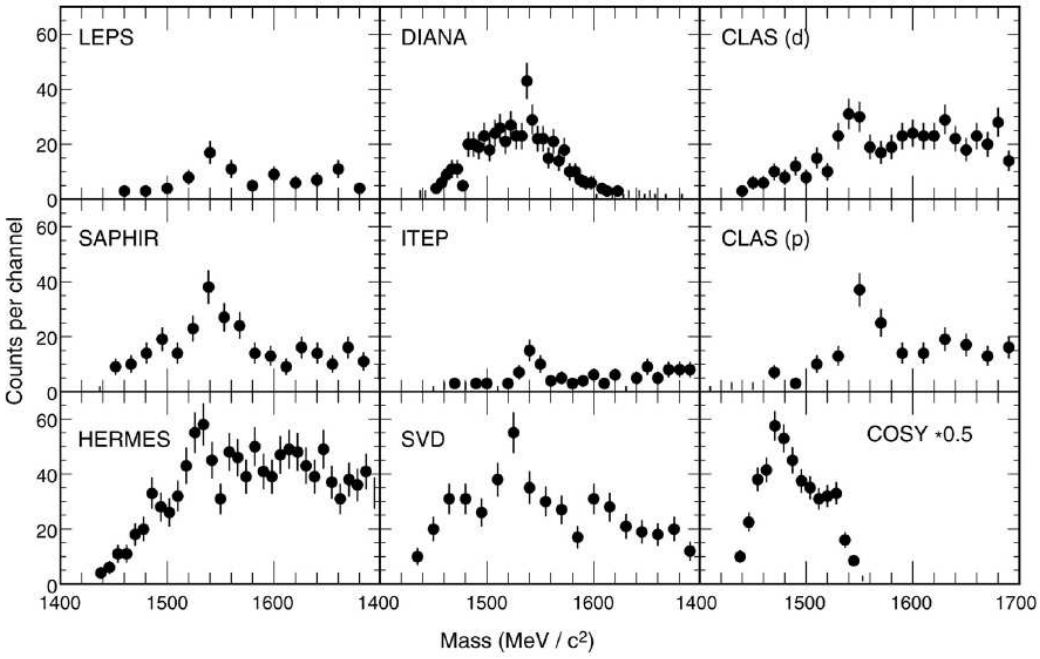

FIGURE 1.7. Some of the world's positive Θ^+ sightings summarized in a pentaquark review article (from (Hicks et al., 2005)). The error bars on the data points are only statistical.

To clarify the situation, in 2004 the CLAS Collaboration performed two experiments at Jefferson Lab dedicated to investigation of the Θ^+. The G10 experiment ran for two months, accumulating almost $5\ pb^{-1}$ of data describing interactions between photons of energies up to $3.6\ GeV$ and a stationary liquid deuterium target. The G11 experiment ran shortly afterwards with a liquid hydrogen target and slightly larger range of photon energies. With the large kinematic coverage of the CLAS detector, these data sets allows for measurement of numerous production and decay modes simultaneously. It also includes a suitable energy range, from threshold up past where some theorists predict a maximum probability of producing the Θ^+ (Azimov and Strakovsky, 2004), at about $2\ GeV$ photon lab energy. Accordingly, Hall-B at Jefferson Lab is a prime facility at which to study pentaquarks.

The $\gamma d \rightarrow pK^-K^0_s(p)$ channel has several advantages compared to other methods of investigating the Θ^+. First, with the large acceptance of the CLAS detector and its photon tagger, the five-particle final state can be fully reconstructed without ambiguity. By measuring the K^-, the neutral kaon's strangeness can be assumed positive, ensuring the pK^0 system to have the same strangeness as the purported Θ^+. In addition, this channel is closely related to that published by CLAS in the $\gamma d \rightarrow K^+K^-np$ reaction, the only difference being the decay mode $\Theta^+ \rightarrow nK^+$. However, the two channels are quite different expermientally. For one, the $K^0_s \rightarrow \pi^+\pi^-$ decay requires the detection of an additional particle, reducing the efficiency. Also, a disadvantage of the exclusive measurement of $\gamma d \rightarrow K^-K^+np$ is that the neutron is left undetected for efficiency considerations. In order to boost the proton into the detector's acceptance, a final state interaction is required.

Most of the publications reporting evidence of a pentaquark lack a physical understanding of the backgrounds and their effect upon the signal. This is due in part to the large number and complexity of all the possible resonant contributions, mesons and baryons. It is much simpler, and maybe less presumptious, to assume a smooth background shape and model it with a polynomial. But that alone is not sufficient to investigate an unconfirmed

resonance. A primary aim of this work is to achieve a more sophisticated backround description by building an amplitude function from the sum of Breit-Wigner distributions for each resonance component, and fitting this model to the data with an unbinned maximum likelihood method.

According to QCD, there is no reason exotic states should not exist, while according to the naive constituent quark model, they are not necessary to describe nature. Of course, if experimentalists can find them, then a proper physics model must accomodate and predict them. On the other hand, if they are nowhere to be found, then QCD must contain an explanation for that, too. Either way it provides physicists with more information on which to base our understanding of the strong interaction.

If an irrefutable pentaquark is found experimentally, then the next task is to measure its properties, notably parity and spin. That will differentiate between the accuracy of the predicting models. If, as has been the case, experiments cannot unambiguously detect an exotic state, creedence to the naive constituent quark model is maintained and explanation is due as to why various models accomodate states not seen in nature.

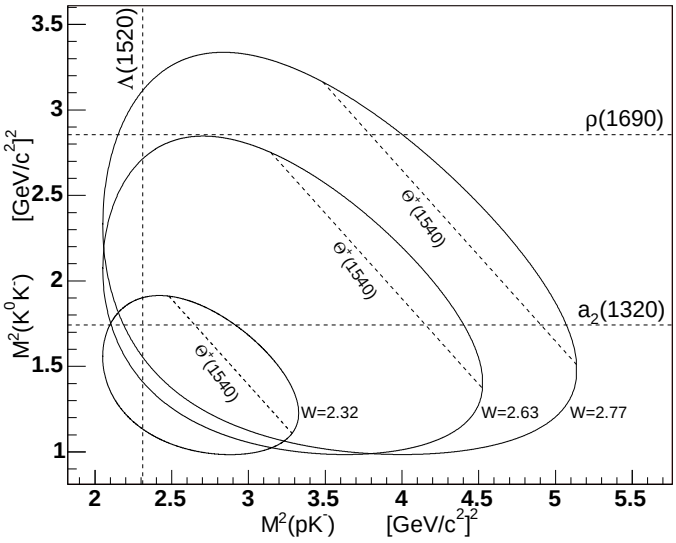

FIGURE 1.8. Phase-space boundaries for the three particles pK^-K^0 evaluated at three values of the total energy W. Dashed lines represent the masses of the $\Lambda(1520)$, $a_2(1320)$, $\rho_3(1690)$, and $\Theta^+(1540)$ resonances.

CHAPTER 2

EXPERIMENT

The data used in this analysis was acquired in Hall-B at Thomas Jefferson National Accelerator Facility (TJNAF). The physical layout is shown in Figure 2.1. The facility's recirculating electron accelerator system can deliver beam simultaneously to three experimental halls with independent detector systems for fixed target nuclear physics experiments. Hall-A contains two high resolution, low acceptance spectrometers for a variety of electron beam physics. Hall-B has a large acceptance, multiple particle spectrometer and utilizes both electron and photon beams with a photon tagger. The program in Hall-C is more varying, with many different collaborations and their experiments and detectors over time.

2.1. CONTINUOUS ELECTRON BEAM ACCELERATOR FACILITY

The accelerator system (CEBAF) roduces a continuous electron beam of energy up to $6\ GeV$ by recirculation. The electrons acquire an additional $1.2\ GeV$ per pass around the entire loop. By delivering beam to the halls from different passes, different energies can be delivered to the three halls simultanesouly.

2.2. CEBAF LARGE ACCEPTANCE SPECTROMETER

The CEBAF Large Acceptance Spectrometer (CLAS) is a symmetrical system of detectors layered around a nuclear target. In this analysis, only the timing scinitillators and drift chambers are used and will be discussed. Additional systems include Cherenkov

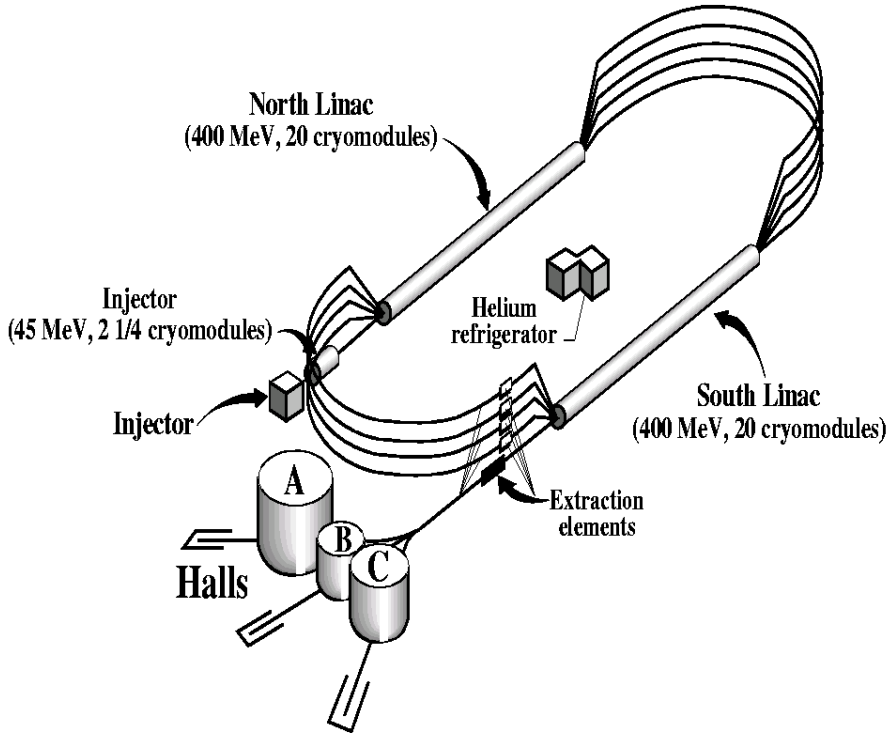

FIGURE 2.1. The layout of Thomas Jefferson National Accelerator Facility, showing relative locations of the injector, linear accelators, recirculating arcs, and three experimental halls.

calorimeters (CC) for e/π separation, electromagnetic calorimeters (EC) for electron energy measurement with electron beam, and hadronic calorimeters (LAC) for neutron energy measurement.

The basis of any spectrometer is its ability to separate particles of different momenta by their curvature in a magnetic field. CLAS's magnetic field is toroidal; in normal operation, as in this analysis, it bends positively charged particles away from the beamline and negatively charged particles towards it. Since no detector can be reliably situated directly in the beamline due to radiation, this means a signifant acceptance hole exists in the forward region for negatively charged tracks. Aside from this, CLAS can measure multiple particle final states in 4π solid angle.

The innermost layer of CLAS, just outside the target, is a coarsly segmented scintillator "start counter" (ST). It is used in the data acquisition (DAC) event trigger due to its proximity to the reaction region. The outermost layer is the time-of-flight scintillators (SC), and its six sectors is shown in Figure 2.4.

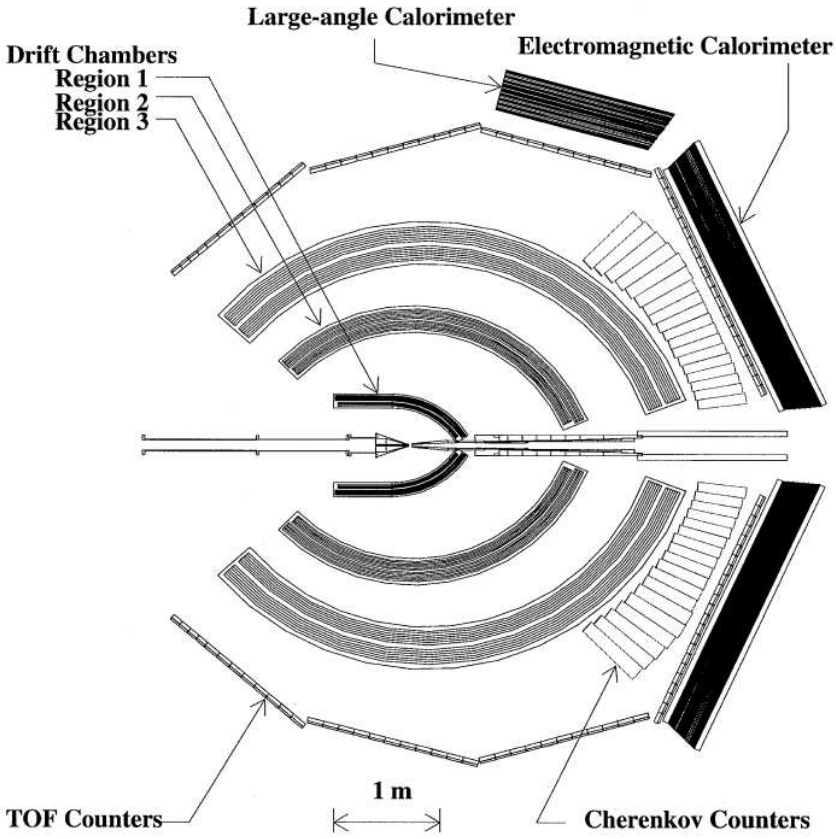

FIGURE 2.2. A schematic cross-section of the CLAS detector system showing two opposing detector sectors. The beamline is in the center pointing towards the right.

2.3. HALL-B PHOTON TAGGER

The photon tagging system in Hall-B provides the ability to use the CLAS system with a photon beam. In this case, the accelerator still delivers an electron beam to the hall, but it is then converted to a photon beam by Bremsstrahlung radiation. In this process, the electron radiates a photon through an electromagnetic interaction with a thin nuclear target. The electron thereby loses some of its initial energy, E_0, to a photon of energy k, and is

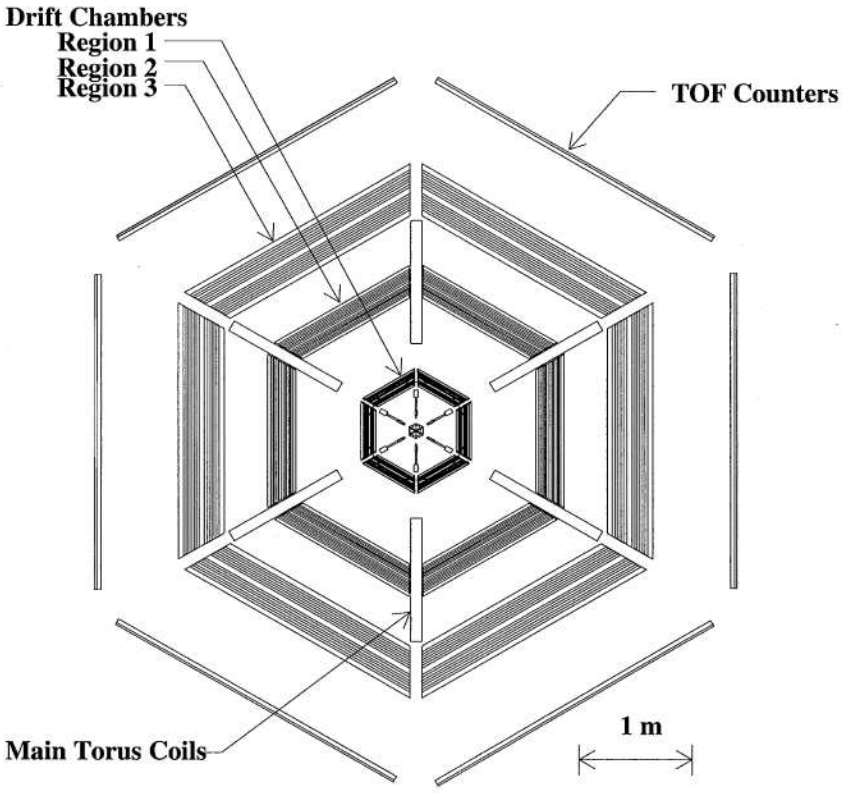

FIGURE 2.3. A schematic cross-section of the CLAS detector system in the $x - y$ coordinate plane showing all six detector sectors. The beamline is in the center and perpindicular the page.

left with energy $E = E_0 - k$. By bending the scattered electron through an homogenous magnetic field and measuring the curvature of its path, its momentum can be measured. Since these are few-GeV electrons, they are relativistic with $\beta \sim 1$ and $p = E$. By also measuring the electron's time, it can be traced back to its coincident photon-produced event in CLAS. This is the purpose of CLAS's photon tagger, shown in Figure 2.5.

2.4. CORRECTIONS

The G10 group has developed corrections for the CLAS detector system and its photon tagger. All corrections have been applied to the data analysis in this work.

2.4.1. Energy Loss. CLAS energy loss corrections for charged particles account for all the materials up to the drift chambers: target materials, start counter scintillators, and an air gap. A thorough comparison was performed between the ELOSS calculation and the

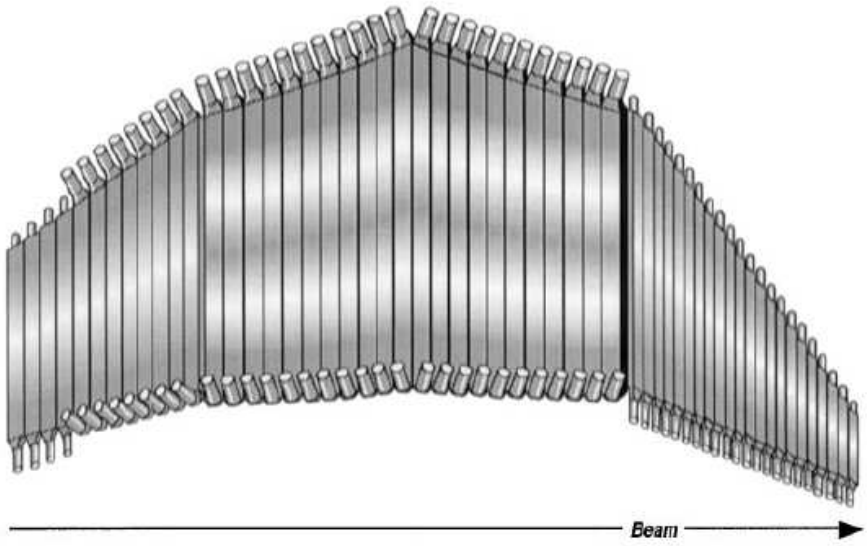

FIGURE 2.4. A drawing of one sector of CLAS's time-of-flight detector system, showing the parallel scintillator bars, each with two photomultiplier tubes. The segmentation is finer on the downstream side of CLAS.

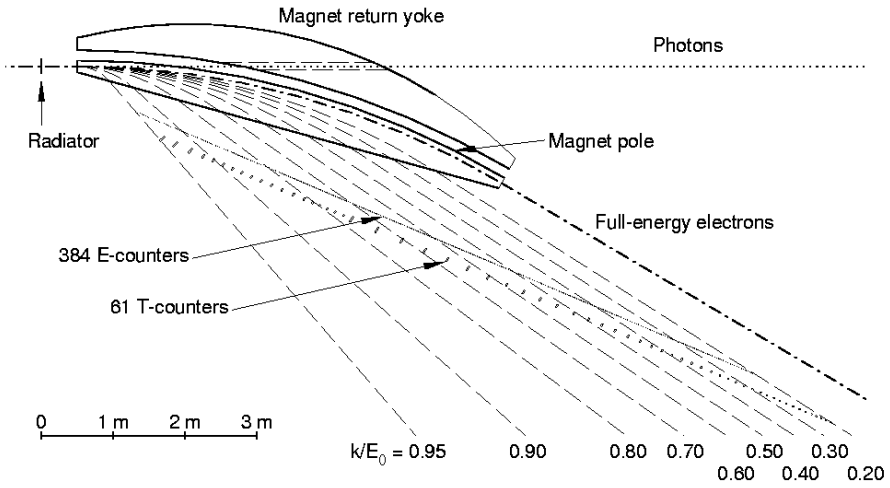

FIGURE 2.5. Schematic of CLAS's photon tagging system, composed of scintillators for electron detection after its curved passage through an homogenous magnetic field.

corresponding energy lost in GEANT simulation, illustrated in Figure 2.7 (Baltzell, 2005). In this analysis of $\gamma d \rightarrow pK^0K^-(p)$, the correction is applied to the proton and K^- as if their tracks originated from the primary vertex in Section 3.2, and to the pions from their detached $K^0_s \rightarrow \pi^+\pi^-$ vertex.

2.4.2. Momentum Corrections. CLAS momentum corrections derived from the deuterium data are used to account for energy loss in the drift chambers. Methods using the invariant mass constraint of $K_s^0 \rightarrow \pi^+\pi^-$ decay (Figure 2.8) and total and transverse momentum conservation in $\gamma d \rightarrow pp\pi^-$ were studied and combined (Mibe, Mirazita, and Baltzell, 2005).

2.4.3. Tagger Energy Spectrum Corrections. A special data set was taken during the G10 run period to study and correct the energy distribution of the photon tagging system. The photon energies were measured independently of the tagger by measuring the spatial distribution of Bremsstrahlung e^+e^- pairs from the photon beam with a silicon micro-strip detector. (Stepanyan et al., 2007).

2.4.4. Electron Beam Energy Corrections. The energy of the electron beam delivered by the accelerator has small fluctuations over the duration of the data acquisition. We can measure the relative energy changes for every run of the data, each which cover roughly two hours time. By using $\gamma d \rightarrow pp\pi^-$ reactions with the final state fully detected, the beam energy can be adjusted to conserve the z-component of the total momentum (equivalent to E_γ in the initial state). Included in this correction are known beam energy shifts from Hall A logs in Table 3.2.

2.4.5. Tagger Multiplicity Correction. Events with more than one electron of the same energy in timing coincidence in the photon-tagging system are rejected during the analysis to ensure a clean measurement. A correction factor to the photon flux compensates for this fraction of lost events.

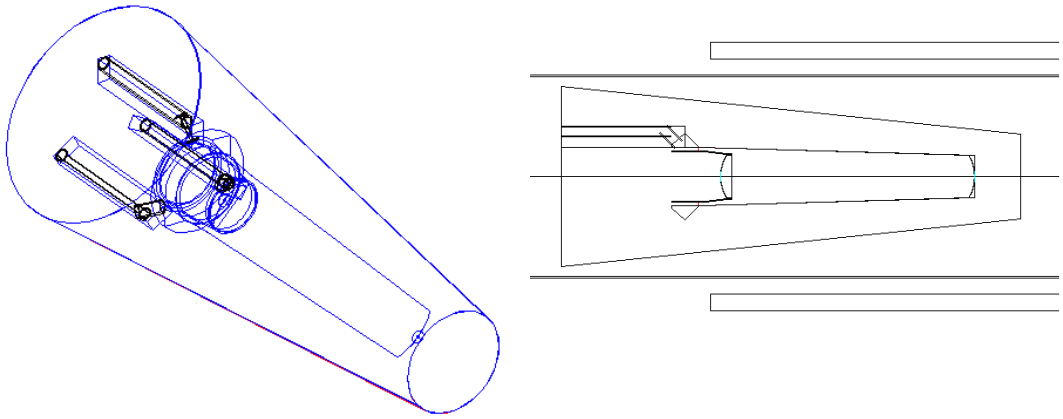

FIGURE 2.6. Drawings of the target cell from GEANT simulation.

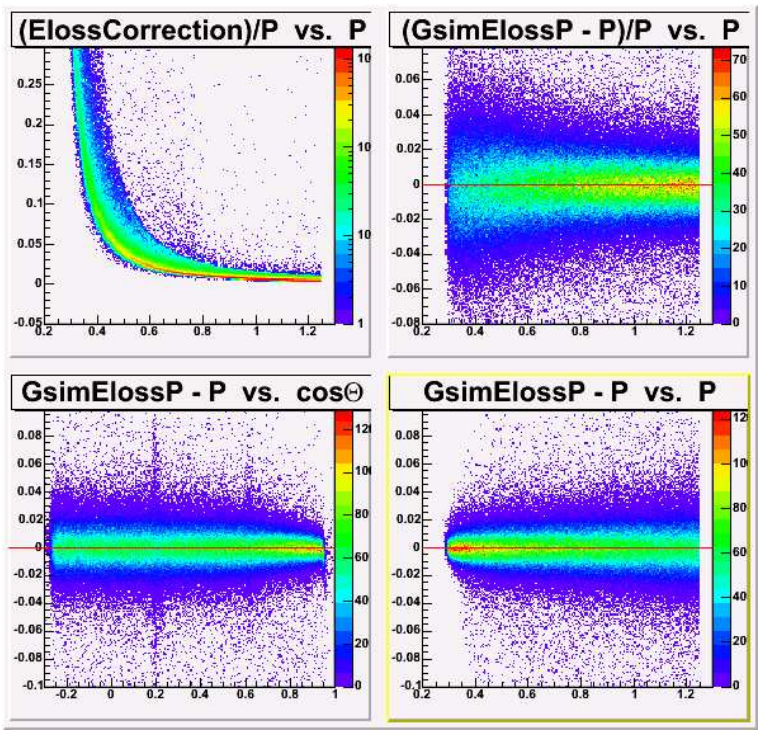

FIGURE 2.7. The upper left plot shows the relative energy loss correction versus momentum for simulated protons. The other three are the residual after applying the correction versus momentum and polar angle, and are centered around zero.

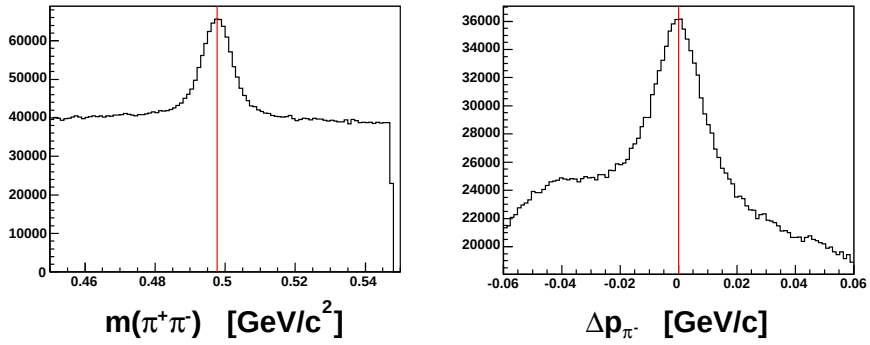

FIGURE 2.8. The invariant mass of the $\pi^+\pi^-$ system (left) integrated over all kinematics from the "Kplusneg" skim. A red line denotes the PDG value of the K_s^0 mass, and it has a measured Gaussian sigma of $4.3\ MeV$. On the right is the calculated shift in π^- momentum necessary to put the invariant mass at its nominal K_s^0 value.

CHAPTER 3

EVENT SELECTION

The selection of events for this analysis begins with the "2pos2neg" skim. This contains all events with at least two positively charged and two negatively charged tracks according to time-based tracking. Then events with all four final state particles $pK^-\pi^+\pi^-$ identified in the PART bank are selected for further analysis. The cuts used in this analysis are summarized in this section and the number of surviving events are summarized in Table 3.1.

3.1. PHOTON SELECTION AND VERTEX TIMING

The selection of beam photons begins by requiring a status flag of 7 or 15 in the TAGR bank. This means the scattered electron which produced the photon was reconstructed in coincidence in both the energy and timing scintillators of CLAS's photon tagging system. Photons corresponding to $T_{id} = 39$ or $T_{id} = 40$ when $E_{id} < 190$ are also ignored, removing a region of artificial multiple hits caused by geometrical overlap in the tagger (Figure 3.19). The most accurate "clock" is the radio frequency (RF) of the accelerator.

For each event, the RF times of the tagged photons at the event vertex are compared to particle timing in CLAS. Both time-of-flight (SC) and start-counter (ST) detectors are used, and the photon which minimizes the timing difference is chosen as the best one. Photons from the same beam bucket, $\pm 1ns$, are counted as "good photons". Events with only one such photon are considered for further analysis.

To further enhance the event selection, a combination of vertex time difference cuts is used, including the time difference between incident photon and outgoing hadrons and between the final-state hadrons themselves. The mean and width of the SC-RF vertex time difference is parameterized as a function of momentum and particle type. This is

done by fitting Δt in momentum slices with a Gaussian peak on a 2^{nd} order polynomial background. Timing cuts of $\pm 3\sigma$ around the parameterized mean values are applied. For the ST, the mean is parameterized, but the cut width is a flat $1\ ns$. The same logic is applied to ST and SC cuts, and then an OR of the two is used.

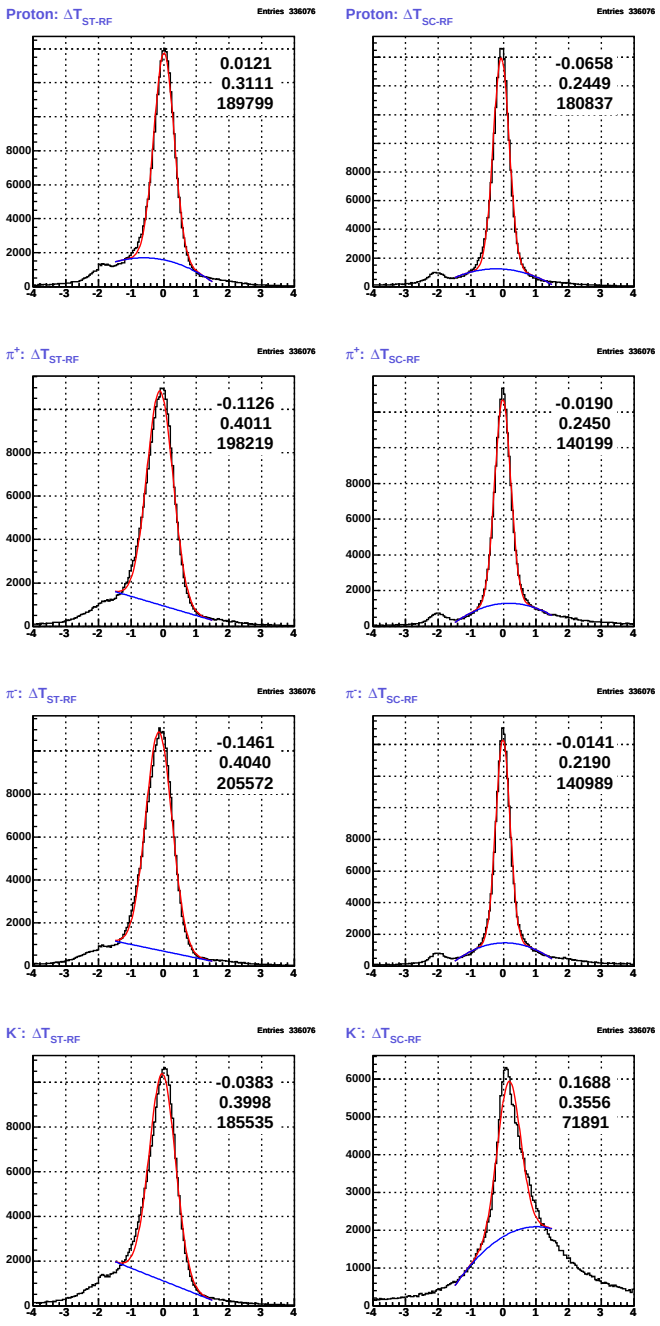

FIGURE 3.1. Left: Photon–particle ST vertex time differences. Right: Photon–particle SC vertex time differences.

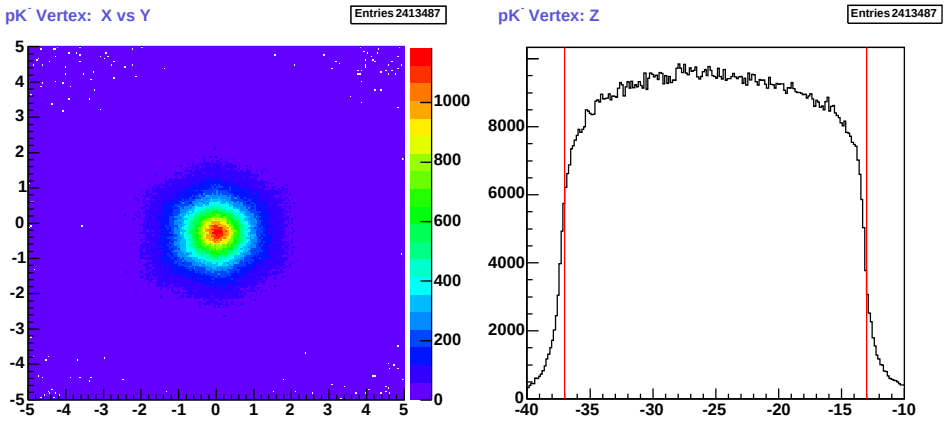

FIGURE 3.2. Reconstructed position of the primary pK^- vertex in the CLAS coordinate system: v_x versus v_y (left) and v_z projections (right). The vertical red lines denote the ends of the target.

3.2. VERTEX POSITION

The primary reaction vertex is determined by averaging the three γpK^- two-particle vertices. The two pion tracks from the neutral kaon decay are not used here because their vertex is expected to be slightly detached. The primary vertex is required to be within the target cell defined by $\sqrt{x^2+y^2} < 2\ cm$ and $-37 < z < -13\ cm$ in the CLAS coordinate frame, else the event is discarded (Figure 3.2).

The $\pi^+\pi^-$ vertex is also calculated, but it is only used for the energy loss correction for the pions. It was investigated whether the distance of closest approach of the two pions or the path length of their mother K^0_s could discriminate between signal and background. However, event selection based on those quantities did not increase the signal/backround ratio of the K^0_S mass peak. Presently, CLAS does not have sufficient vertex resolution to investigate the detached vertex of $K^0_S \rightarrow \pi^+\pi^-$ with its small $c\tau$ of only $2.7\ cm$. The K^0_L case is ignored because the efficiency for its detection is much smaller due to its three pion decay and larger decay length of $c\tau = 15.5\ m$.

3.3. K^-/π^- MISIDENTIFICATION

The primary source of particle misidentification occurs when the detected K^- is really a misidentified π^-. This background is shown in the $MM(pK^-\pi^+\pi^-)$ spectrum below the

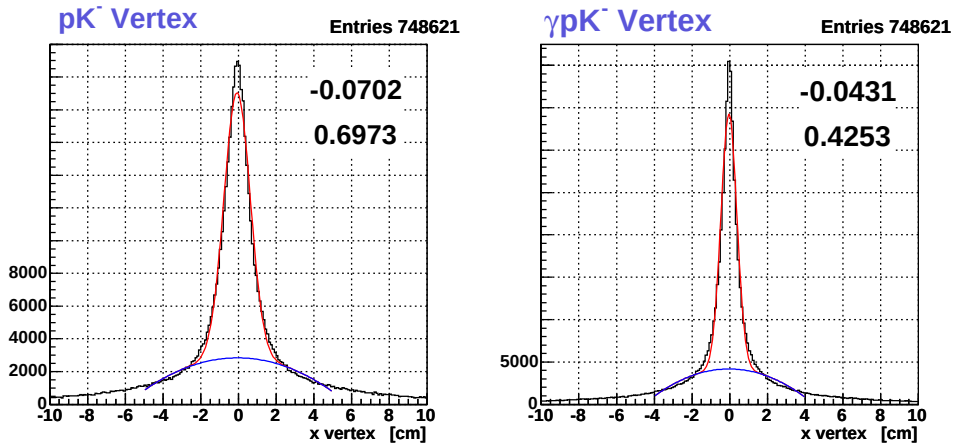

FIGURE 3.3. The pK^- vertex position projected into the x-direction. The right plot includes the beamline as a constraint.

proton mass in Figure 3.4 and Figure 3.5. After selecting events in the K^0_s peak, it is largely reduced and well separated from the signal. Events with $MM(p\pi^-_{misid}\pi^+\pi^-)$ less than 980 MeV/c^2 are removed from the sample, as designated by the horizontal line in Figure 3.4. Additional K/π misidentifications are addressed with kinematic fitting in Section 3.6.

3.4. K^0_s AND MISSING PROTON IDENTIFICATION

The K^0_S is reconstructed by measuring its two daughter pions. We place a $\pm 3\sigma$ cut around the gaussian peak in the $M(\pi^+\pi^-)$ spectrum, which amounts to $\pm$ 13 MeV/c^2. A missing proton is also selected with $\pm 3\sigma$, $\pm$ 31 MeV/c^2, cut on the signal in the $MM(pK^-K^0_S)$ spectrum. In order to determine the mean and width of their Gaussian distributions, either one of the two peaks is selected and the other one fitted with a 2^{nd} order polynomial and Gaussian peak. Those distributions are shown in the yellow histogram of Figure 3.6.

3.5. SPECTATOR MOMENTUM

The missing momentum in the reaction is defined as $\vec{P}_{miss} = \vec{P}_\gamma - \vec{P}_p - \vec{P}_{K^-} - \vec{P}_{\pi^+} - \vec{P}_{\pi^-}$. If this momentum is to be carried away from the interaction by one spectator proton, its distribution should be peaked near 40 MeV/c according to the Bonn potential's wave

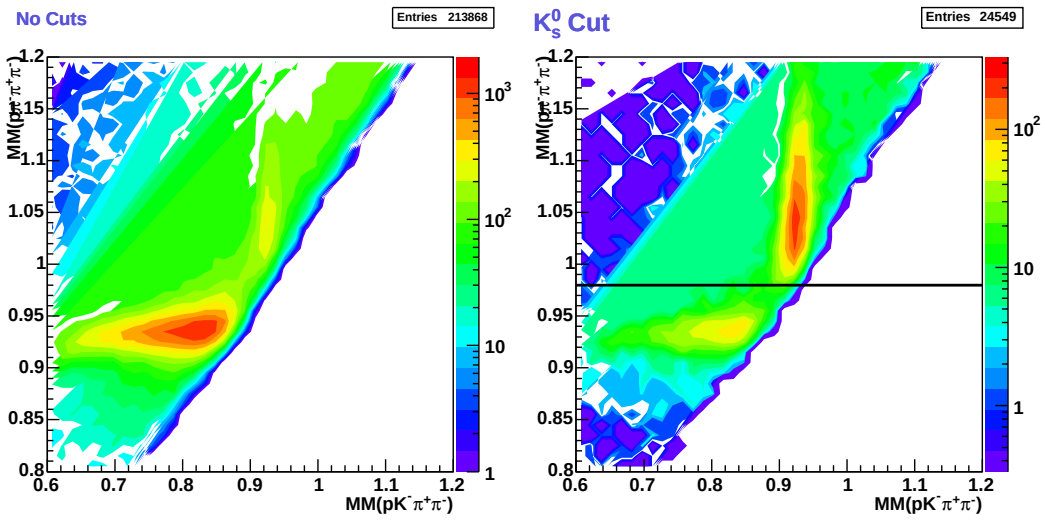

FIGURE 3.4. $MM(p\pi^+\pi^-\pi^-_{misid})$ versus $MM(p\pi^+\pi^-K^-)$ before (left) and after (right) selecting the K^0_s mass peak.

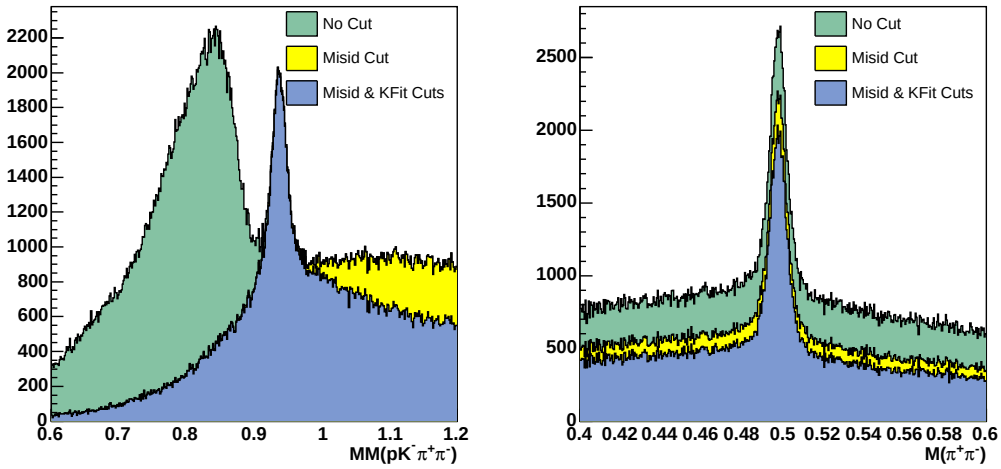

FIGURE 3.5. The effect of K/π misidentification cuts on the missing proton mass (left) and the $\pi^+\pi^-$ invariant mass (right). The yellow histogram is after the cut on $MM(p\pi^+\pi^-\pi^-_{misid})$ shown in Figure 3.4, and the least populated histogram is after a cut on the χ^2 from 1-C kinematic fits to misidentified particles.

function description of deuterium. A cut is placed requiring the momentum of the undetected proton to be less than $120\ MeV/c$, as shown in Figure 3.8. A further reason for this cut is that detector simulation using protons generated from a Bonn potential does not provide enough strength in the high momentum tail to describe the data. This is due at least

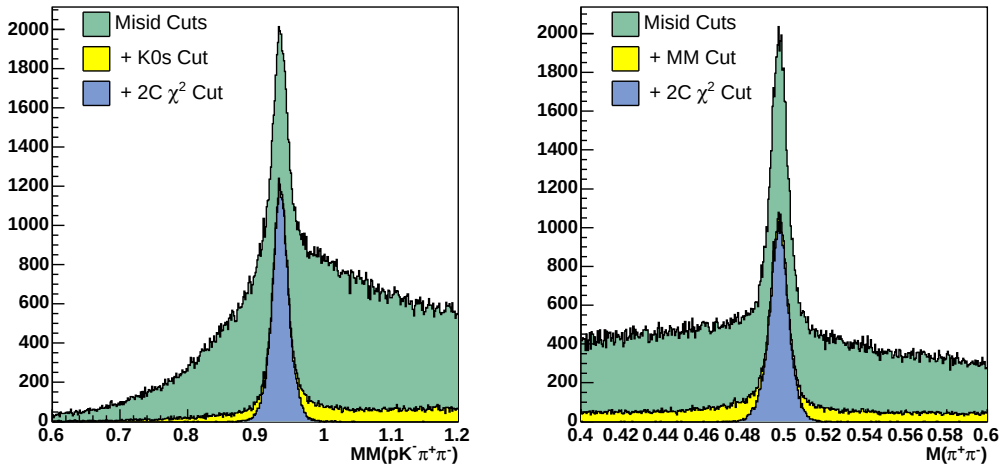

FIGURE 3.6. The missing proton's reconstructed mass (left) and $\pi^+\pi^-$ invariant mass (right) after all K/π misidentification cuts. The yellow histogram adds a $\pm 3\sigma$ cut on the other's mass peak, and the blue histogram also adds a χ^2 cut on the 2-C kinematic fit.

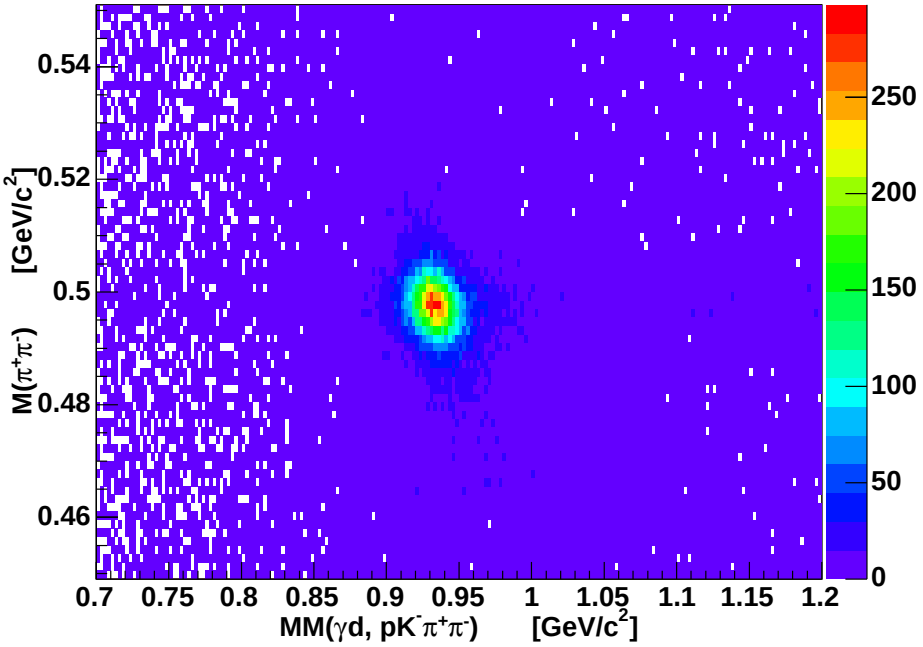

FIGURE 3.7. The $\pi^+\pi^-$ invariant mass (y-axis) versus the missing proton's mass (x-axis) after all misidentification cuts, clearly showing the $\gamma d \rightarrow pK_s^0K^-(p)$ signal. These are the same events as those in the most populated histogram in Figure 3.6.

partially to final state interactions between outgoing hadrons, which we desire to minimize in this analysis.

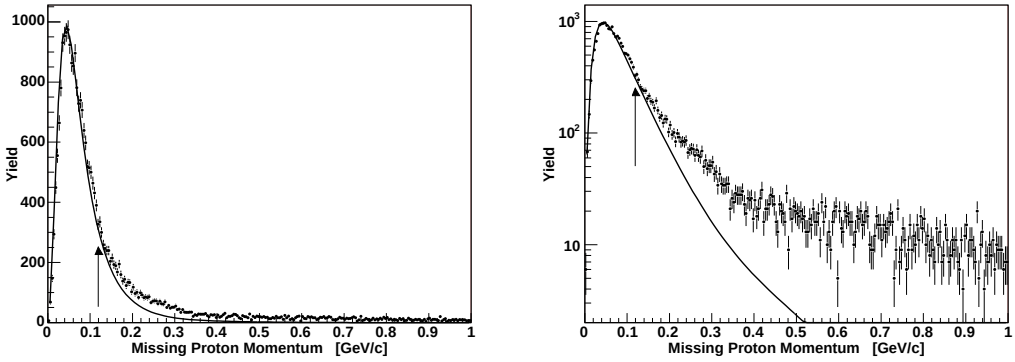

FIGURE 3.8. Reconstructed momentum of the undetected proton in linear and log scales, where an arrow denotes the cut location of $120\ MeV/c$ and solid line represents the Bonn model for deuterium.

3.6. KINEMATIC FITTING

The CMU kinematic fitter is employed to better identify the channel and conserve four-momentum. The fitting code was written to work for any final state, so it can be used to fit to background processes with misidentification or the desired signal channel, $\gamma d \rightarrow ppK^0K^-$. Event by event, the four-momenta of the initial and final state particles are fit to determine the probability the event corresponds to a given channel.

3.6.1. Calibrating the Kinematic Fitter with $\gamma d \rightarrow pp\pi^-$. Calibration of the kinematic fitter requires the determination of the CLAS resolution for the momentum and angle determination of detected particles. The reaction used to calibrate the kinematic fitter is $\gamma d \rightarrow pp\pi^-$ and the method follows that described in CLAS-NOTE 04-017. The incoming photon is detected in the Hall-B tagger and the three final state particles are detected in CLAS. This overly determines the kinematics, allowing the comparison of measured quantities with expected values determined by four-momentum conservation. This difference in quantities is the resolution.

The resolution of CLAS for a particular variable can depend on momentum and angle of detection, thus it is optimal to determine the resolution parameter for a range of kinematics. Figure 3.9 shows the coverage of the reaction $\gamma d \rightarrow pp\pi^-$. The tops plots are proton momentum versus angle. By combining information from both the fast and slow proton, the resolution of CLAS is determined from threshold of detection to 1.4 GeV/c and over all detection angles. The bottom left plot shows the pion momentum versus angle and the bottom right plot the proton-proton correlations in momentum.

3.6.1.1. *Resolution Determination.* The resolution for a particular variable is determined by comparing the measured value to the kinematically determined value. For example, the kinematic fit is performed while excluding one of the protons, and its momentum is determined by the fit. This "fit" momentum is compared to the detected momentum in bins of detection angle as show in Figure 3.10. The spread in momentum (Δp) is plotted as a function of proton momentum.

The resolution data of Figure 3.10 is then fit with a gaussian in vertical slices to determine the mean and width (σ). The results for the width σ are shown in Figure 3.11. The trend of the resolution parameter σ are then parameterized by a linear fit that is represented by the solid black line in the figure. The red curves in the top 3 panels are the original parameterization using g1c data $\gamma p \rightarrow p\pi^+\pi^-$. The g10 data provide a much wider range of resolution determination due to the wider kinematic coverage of $\gamma d \rightarrow pp\pi^-$. This procedure was duplicated for the pion momentum as well and the information has been coded into the kinematic fitting routines to provide the best possible fit to the g10 data.

The resolution for the angle determination is determined from the TBER bank. The tracking coordinated are used and the the angles are designated as λ and ϕ. The resolution in these angles (σ_λ and σ_ϕ are shown as a function of momentum in the left panels of Figure 3.12. The right panels plot the centroid of a gaussian fit to vertical slices (points) and a fit to the centroid (solid line) is used to parameterize the resolution as a function of momentum. This parameterization has been coded into the kinematic fitting routine.

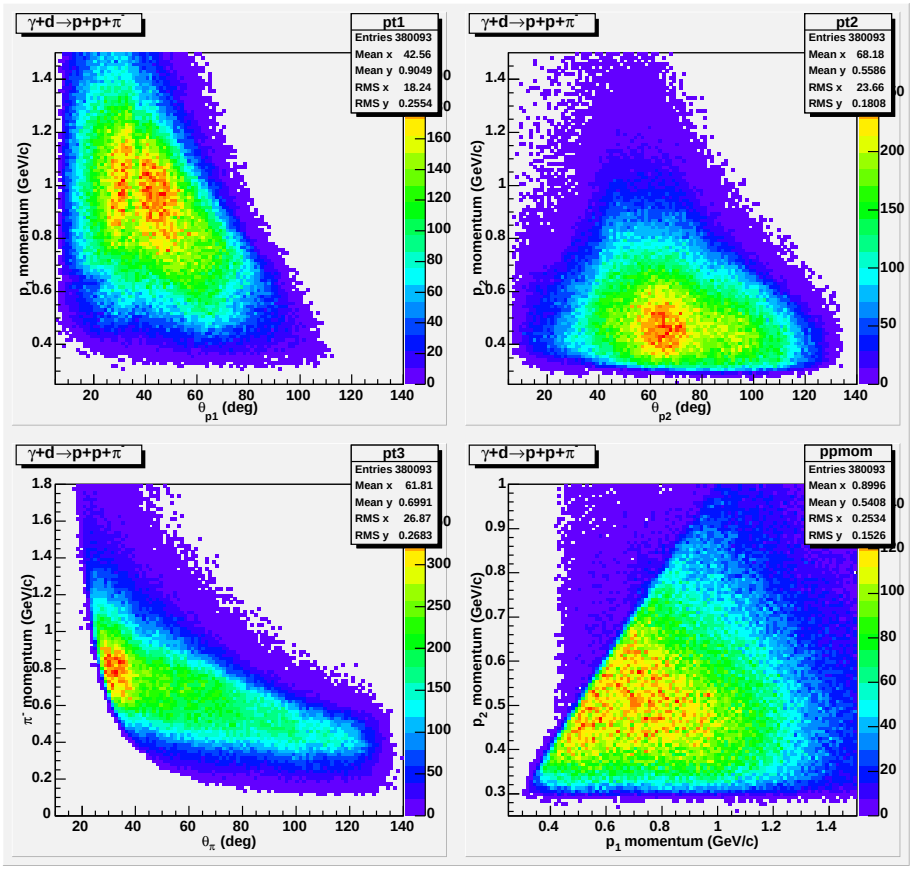

FIGURE 3.9. Kinematics of the reaction $\gamma d \to pp\pi^-$.

3.6.1.2. *Pulls and Confidence Levels.* Calibration quality for a kinematic fitter is determined by pull distributions and confidence level distributions. Pull distributions should be centered around zero and have a width of one. The confidence level of the fit should be as flat as possible indicating uniform probability of correct event reconstruction. The rise at low probabilities indicated background events or problems in the kinematic fit quantities. Typically a cut is put on the confidence level to remove the poorly reconstructed events. Figure 3.13 and Figure 3.14 show the good quality of the pulls and confidence level distributions for the two magnetic field settings of the g10 data.

3.6.2. K/π **Misidentification (1 Constraint).** The confidence levels from 1-C kinematic fits to some K/π misidentifications are shown in Figure 3.17. The effect on mass spectra of removing these backgrounds with a 1% probability cut is shown in Figure 3.5.

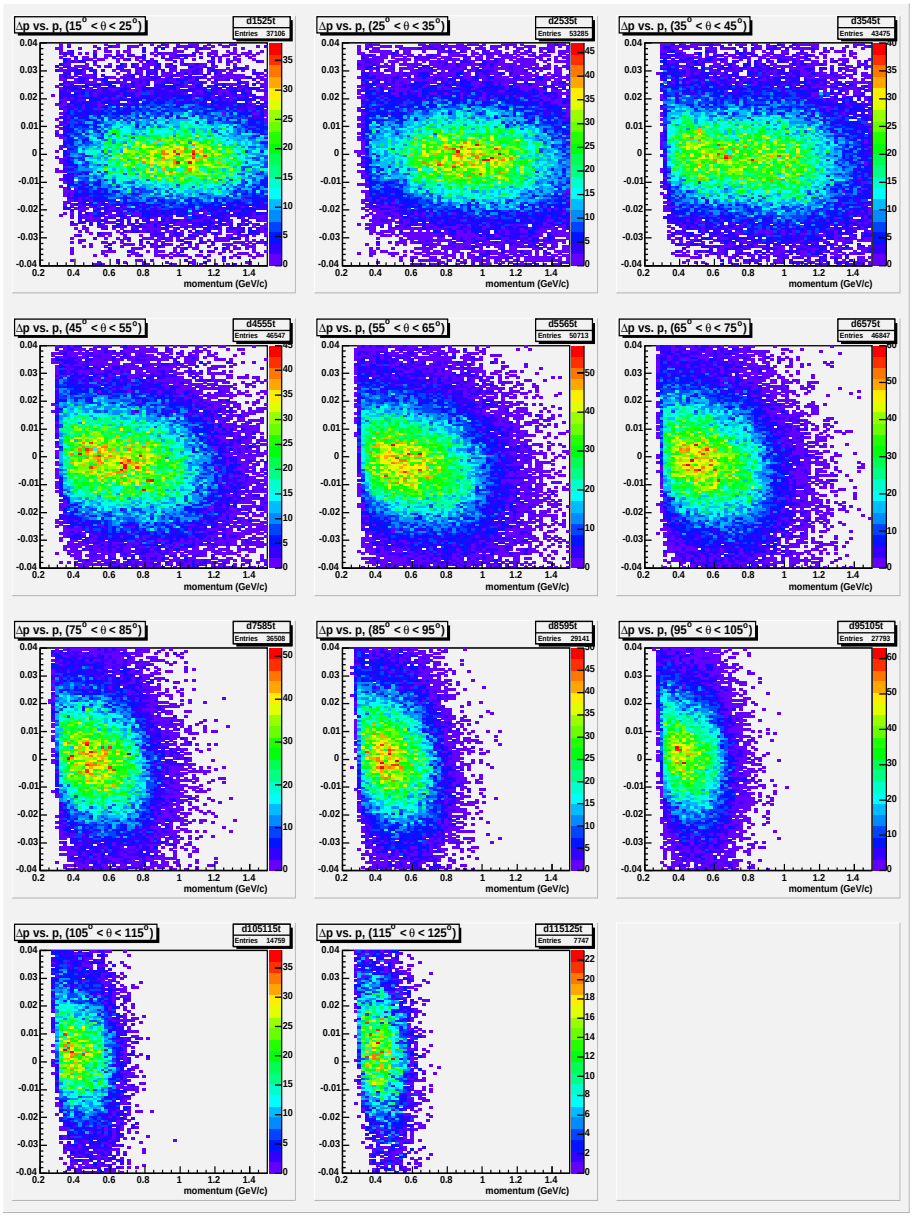

FIGURE 3.10. Difference between fit momentum and detected momentum for protons in θ bins.

The case when both the K^- and π^- are misidentified is not used because it is kinematically indistinguishable from our signal channel when the pion and kaon have similar momentum.

3.6.3. $\gamma d \to pK^0_s K^-(p)$ **(2 Constraints).** A 2-C kinematic fit is employed. This constrains the masses of the missing proton and K^0_s to their known values by adjusting three-momenta of the final state particles and the energy of the photon. A confidence level for

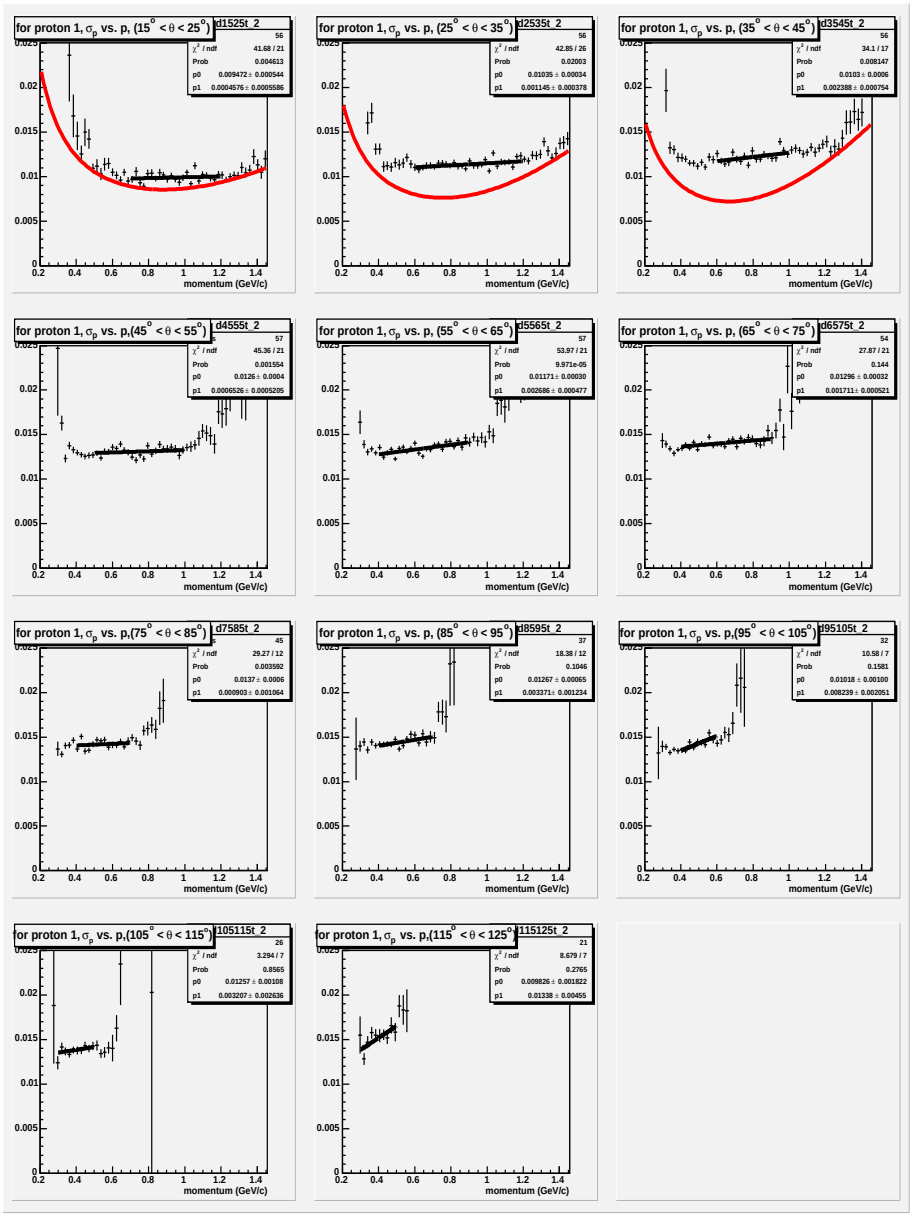

FIGURE 3.11. Evolution of the width (σ) with momentum for different angle bins of Figure 3.10. Red curve in panels in the top row is the resolution parameterization from g1c. The solid black curves are linear fits used to extract the trend.

each event provides a global means of selecting good $\gamma d \rightarrow pK^0_s K^-(p)$ events, and Figure 3.6 shows the effect of a requiring at least a 1% confidence level.

The "pulls" for momentum, λ, and ϕ (similar to ϕ and θ lab angles respectively) for each particle are shown in Figure 3.15 and Figure 3.16. If the tracking covariance matrix

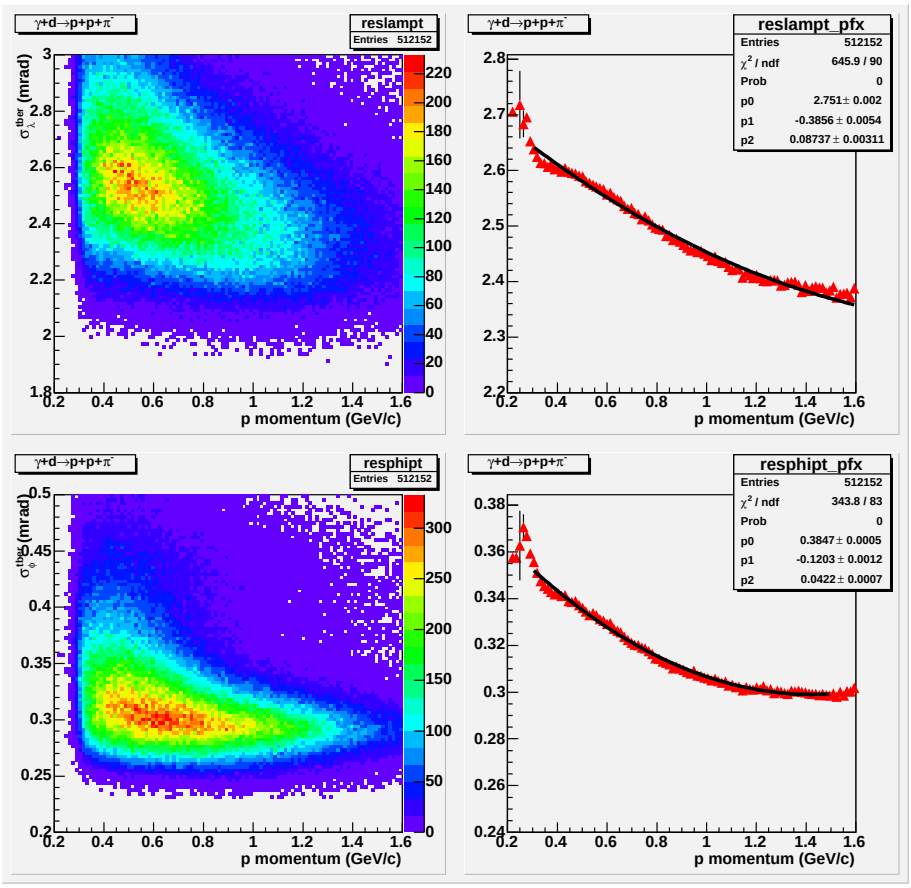

FIGURE 3.12. Resolutions from the TBER bank.

is accurate, the pulls should be centered at zero with sigmas of 1, and a study of this was conducted with G10 data and the fully constrained reaction $\gamma d \rightarrow pp\pi^-$.

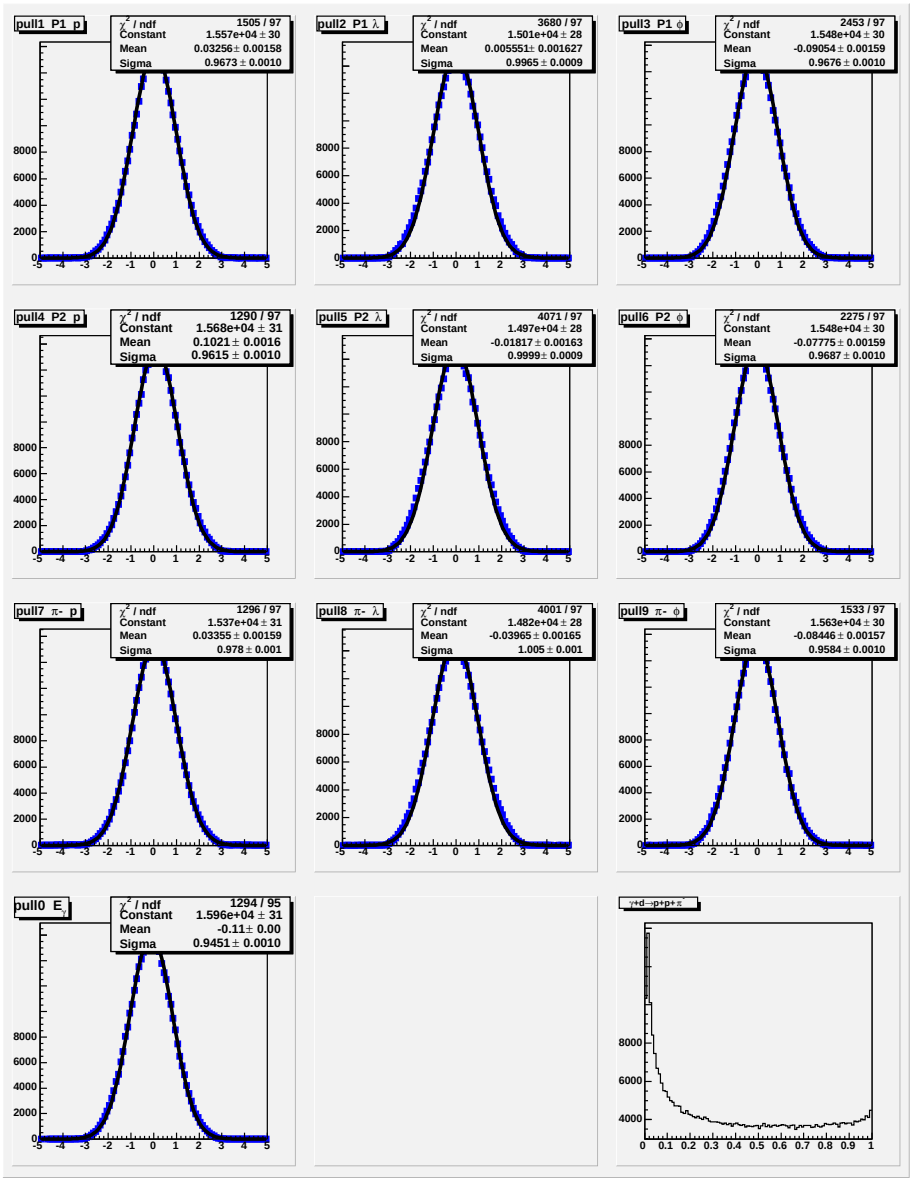

FIGURE 3.13. Pulls of a $4-C$ kinematic fit of the reaction $\gamma d \rightarrow pp\pi^-$ for 3375A Data.

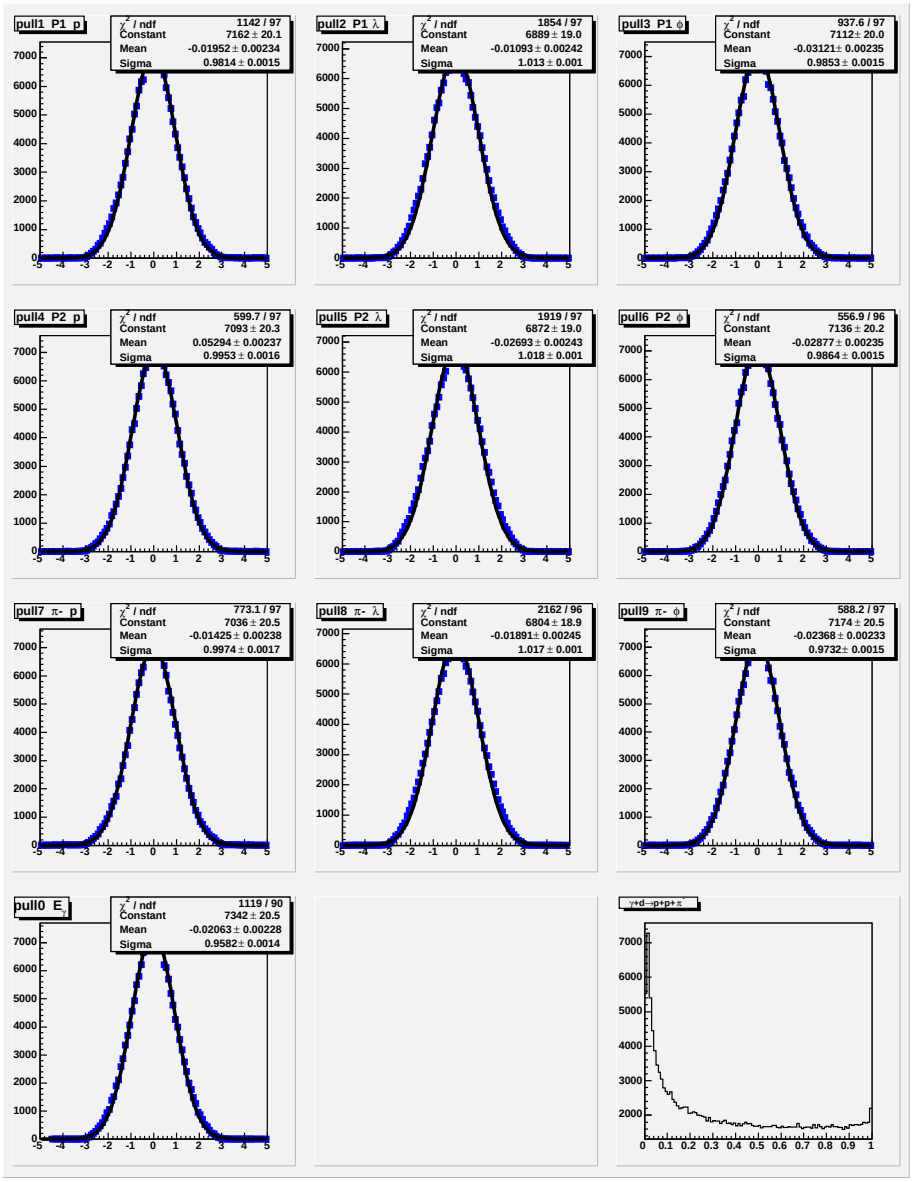

FIGURE 3.14. Pulls of a $4-C$ kinematic fit of the reaction $\gamma d \rightarrow pp\pi^-$ for 2250A Data.

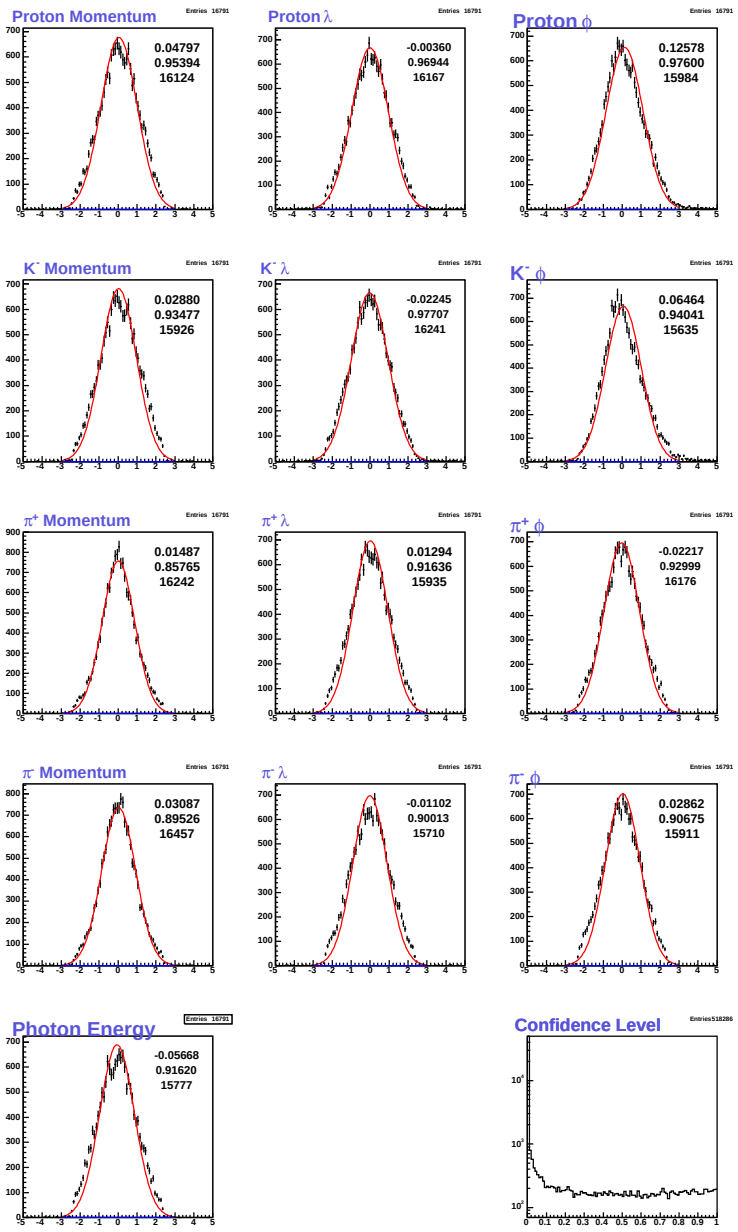

FIGURE 3.15. Pulls of a $2-C$ kinematic fit of the reaction $\gamma d \rightarrow pK_s^0K^-(p)$ for 2250A Data.

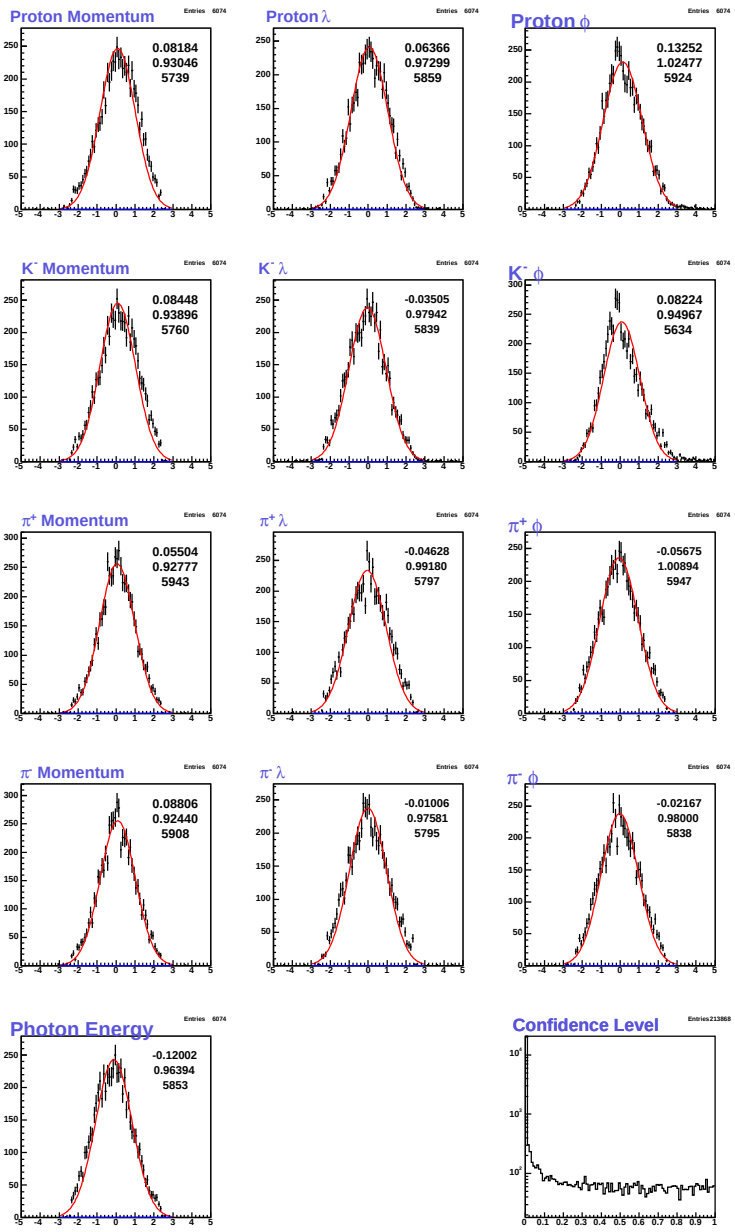

FIGURE 3.16. Pulls of a $2-C$ kinematic fit of the reaction $\gamma d \rightarrow pK_s^0K^-(p)$ for 3375A Data.

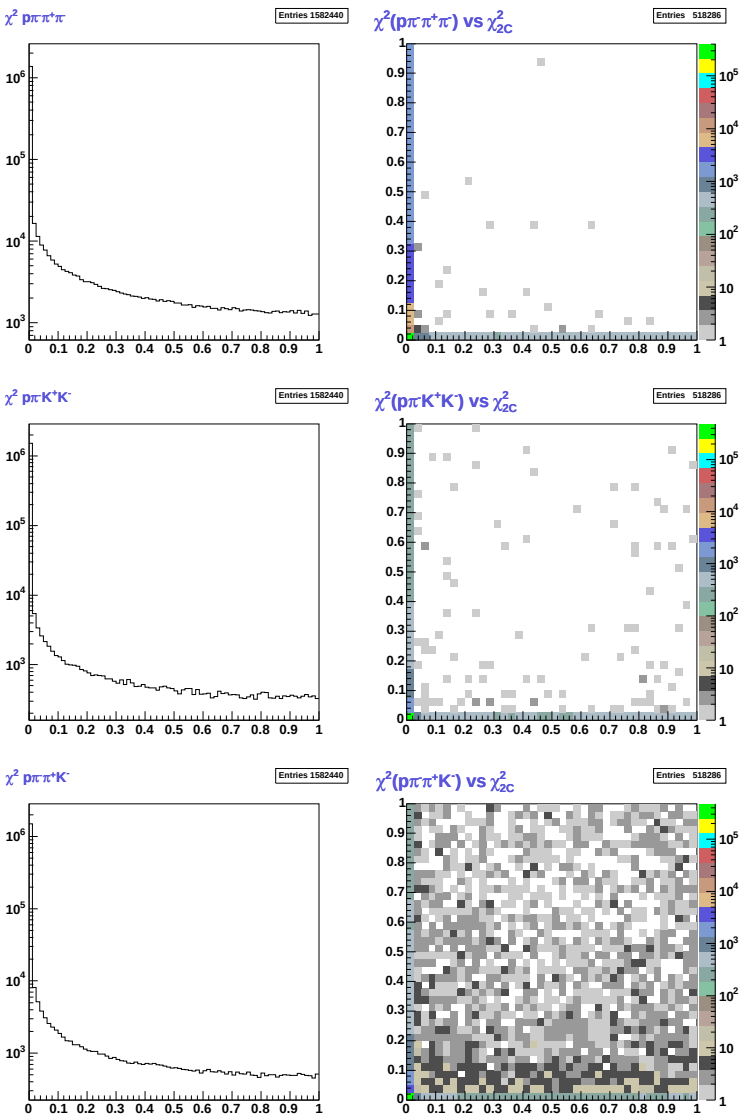

FIGURE 3.17. Confidence levels for 1-C kinematic fits to final states containing different combinations of misidentified kaons and pions ($p\pi^+\pi^-\pi^-$, $p\pi^-K^+K^-$, and $p\pi^-\pi^+K^-$ by row). The right column shows the density of overlap with the 2-C probability for the signal channel $\gamma d \to pK^0K^-(p)$ on the x-axis. The bottom row is the case where π^- and K^- are misidentified as each other, i.e. the rest masses of the two are reversed in the kinematic fit.

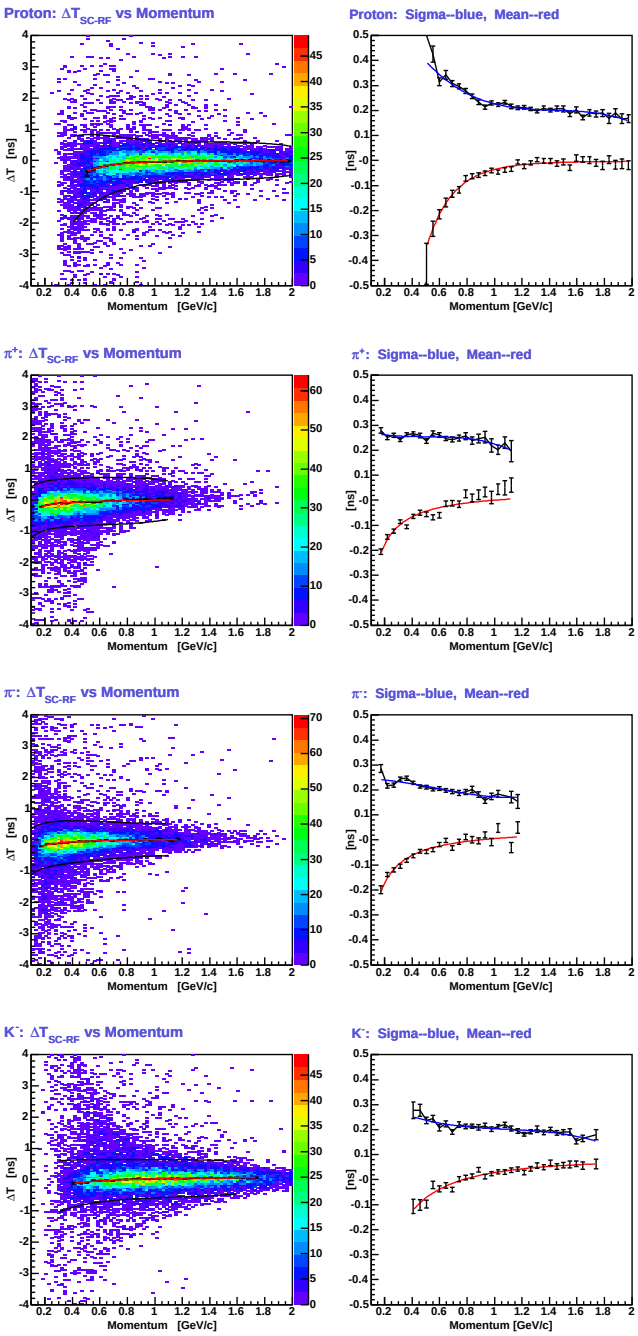

FIGURE 3.18. Momentum dependence of $SC - RF$ vertex timing for each final state particle type. The right column shows the Gaussian means and sigmas as a function of momentum calculated by fitting slices of the two-dimensional histograms.

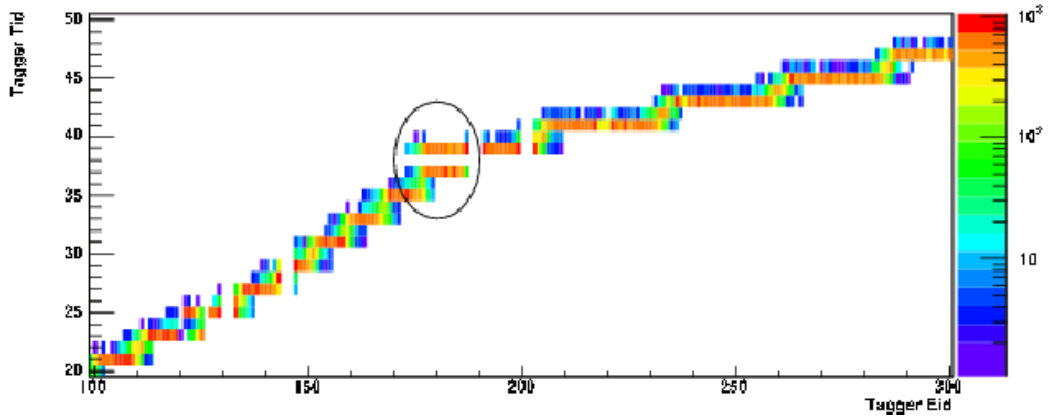

FIGURE 3.19. Number of events in the photon tagger as a function of timing versus energy scintillators. Caused by a geometrical overlap in the detector, two timing channels cover the same energy counter, and the doubly-counted hits in the upper time channel are ignored.

		# Surviving Events	
Description	Requirement	$3375A$	$2250A$
PID - PART Bank	$p\pi^+\pi^-K^-X$	727229	1582440
#photons within 1 ns of CLAS	$N_\gamma = 1$	678863	1396890
SC/ST-RF Time Difference	$< 1.5\ ns$	444206	905666
pK^- Vertex Position	In Target Cell	213868	518286
$MM(p\pi^-_{misid}\pi^+\pi^-)$	$> 0.98\ GeV/c^2$	122154	326310
K^0_s - $M(\pi^+\pi^-)$	$\pm 3\sigma$	18576	48853
Missing Proton - $MM(pK^-K^0_s)$	$\pm 3\sigma$	20668	49119
K^0_s and Missing Proton	$\pm 3\sigma$	7213	17716
Missing Proton Momentum	$< 0.15\ GeV/c$	6013	11842
$\Lambda(1520)$ Removal - $M(pK^-)$	$> 4\sigma$ above peak	3687	9696
2-C Kinematic Fit Probability	> 0.005		

TABLE 3.1. Data selection sequence and the number of surviving events for each setting of the torus magnet field. The yields for the two field settings differ by approximately a factor of two.

CLAS Run Numbers	Correction Scale Factor
$42300 - 42716$	1.0003
$42908 - 42909$	1.0005
$42912 - 42934$	1.0005
$42937 - 42953$	1.0005

TABLE 3.2. Beam Energy Shifts from Hall A Logs

CHAPTER 4

MODEL AND FITTING DEFINITIONS

A simple t-channel model is developed that simulates the numerous resonant backgrounds. Baryon (qqq) and meson ($q\bar{q}$) resonant states can be produced from the photon-neutron interaction. Most notable is the $\Lambda(1520)$, a four-star hyperon state. A t-channel exchange particle is denoted by a vertical dotted line in the Feynman diagrams.

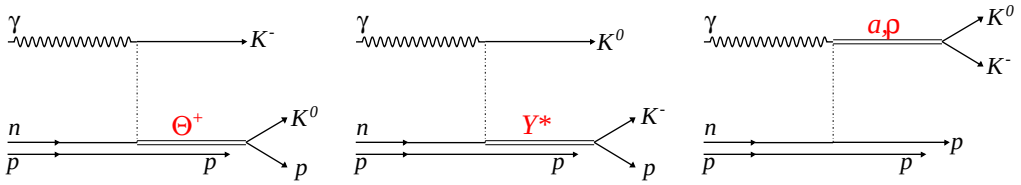

FIGURE 4.1. Diagrams for the photo-production of the Θ^+ pentaquark, Y^* hyperons, and mesons off a quasi-free neutron inside deuterium. The "spectator" proton is not involved in the reaction.

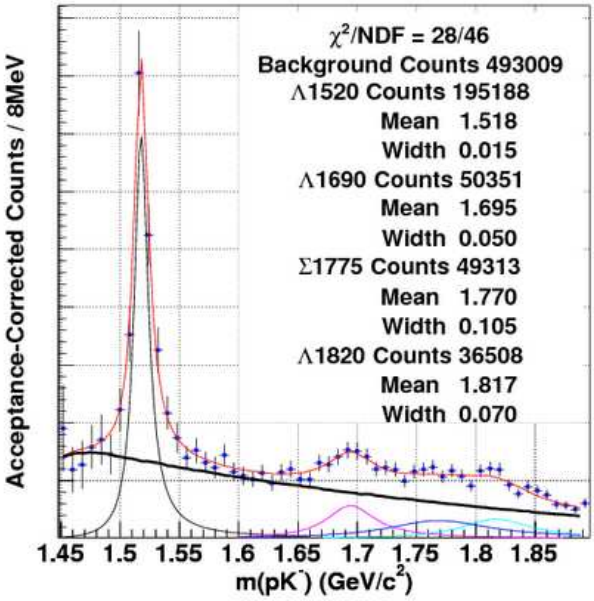

FIGURE 4.2. One dimensional fit (red line) to the data's efficiency-corrected pK^- invariant mass spectrum (data points). The fit function includes contributions from relativistic Breit-Wigner distributions for hyperon resonances (colored lines) added coherently to a phase-space component (thick black line).

4.1. KINEMATICS

The initial state is described by the energy of the beam photon, E_γ, and the momentum vector of the target neutron. The deuterium nucleus is at rest in the lab frame. The proton inside that deuterium is assumed a "spectator" and not involved in the photon-neutron reaction that produces the detected pK^0K^- final state. This undetected "spectator" proton carries away the same momentum it had in the initial state, and the photon interacts with a "quasi-free" neutron. Due to conservation of momentum inside deuterium, the proton's momentum is assumed antiparallel that of the neutron in the initial state. The center-of-mass energy, W, is the mass of the energy-momentum four-vector of the $\gamma - n$ system. After forcing energy and momentum conservation with a kinematic fit, W computed from the four-momenta of the final state particles is equivalent.

$$\begin{aligned} W^2 &= (\gamma + n)^\mu (\gamma + n)_\mu = E_\gamma E_n - \vec{p}_\gamma \cdot \vec{p}_n \\ &= (p + K^0 + K^-)^\mu (p + K^0 + K^-)_\mu \end{aligned} \tag{1}$$

In the final state, invariant masses are calculated as the mass of the energy-momentum four-vector of the corresponding two-particle system:

$$M_{ij}^2 = (p_i + p_j)^\mu (p_i + p_j)_\mu = E_i E_j - \vec{p}_i \cdot \vec{p}_j. \tag{2}$$

Two momentum transfers are considered, that from the beam photon to the K^0K^- system, and from the target neutron to the pK^- system:

$$\begin{aligned} t_{K\bar{K}} &= (\gamma - K\bar{K})^\mu (\gamma - K\bar{K})_\mu, \\ t_{pK^-} &= (n - pK^-)^\mu (n - pK^-)_\mu. \end{aligned} \tag{3}$$

The helicity frame is used to investigate the angular distribution of resonance decays. Its z-direction is parallel that of the resonance's flight in the total center of mass system. The y-direction is normal to the production plane and can be written as $\hat{\gamma} \times \hat{z}$ (Schilling, Seyboth, and Wolf, 1970), where $\hat{\gamma}$ is the unit vector parallel to the direction of the beam photon ($\hat{z}_{lab}$). The x-direction follows naturally as $\hat{x} = \hat{y} \times \hat{z}$. One of the two decay

particles is chosen for which to calculate the azimuthal and polar helicity angles, ϕ^* and θ^*. For the pK^- system, it is the K^- whose angles are calculated, and for K^0K^- the neutral kaon is chosen.

4.2. AMPLITUDE FUNCTION

The probability of transition from initial to final state is described by a complex amplitude dependent upon the kinematic event variables and resonance parameters. The amplitude for one resonance in our model is composed of production and decay factors:

$$A = C\left[e^{b(t-t_0)}\right]\left[B_l(\mu)\cdot Y_m^l(\theta^*,\phi^*)\right] \tag{4}$$

The complex coefficient C is an overall normalization accounting for both production and decay probabilities. The exponential term describes a t-channel production mechanism. The strength of its t-dependence is controlled by the parameter b, the t-slope. The expression $t-t_0$ is the difference between the momentum transfer and its minimum kinematically allowed value, which depends on the beam energy.

The decay term contains a fully relativistic, complex Breit-Wigner amplitude, B_l. It is a function of the invariant mass, μ, of the two daughter particles:

$$B_l(\mu) = \frac{\mu_0\,\Gamma_0 F_l(q)}{\mu_0^2-\mu^2-i\mu\,\Gamma_l(\mu)}. \tag{5}$$

The parameters μ_0 and Γ_0 are the nominal mass and width of the resonance, and l is the angular momentum quantum number of the decay mode. The momentum of the daughters in the resonance's rest frame is the variable q, the "decay momentum". Following from four-momentum conservation, it can be written as a function of only the invariant mass and the daughter masses, μ_1 and μ_2:

$$q(\mu) = \frac{\sqrt{(\mu^2-(\mu_1+\mu_2)^2)(\mu^2-(\mu_1-\mu_2)^2)}}{2\mu}. \tag{6}$$

The fully relativistic form of the Breit-Wigner contains a functional width dependent on the mass and orbital angular momentum state of the decay:

$$\Gamma_l(\mu) = \Gamma_0 \cdot \frac{\mu_0}{\mu} \cdot \frac{F_l(q)}{F_l(q_0))} \left(\frac{q}{q_0}\right)^{2l+1} . \tag{7}$$

The parameter q_0 is the value of the decay momentum corresponding to the nominal resonance mass. The Blatt-Weisskopf barrier factors, F_l, appear in the Breit-Wigner and its functional width. The first few barrier factors are shown below, where $z = (p/p_r)^2$ and $p_r = 0.1973\ GeV/c$ corresponds to the distance scale of one femtometer (Chung, 1993).

$$\begin{aligned} F_0(z) &= 1 \\ F_1(z) &= \sqrt{\frac{2z}{z+1}} \\ F_2(z) &= \sqrt{\frac{13z^2}{(z-3)^2+9z}} \\ F_3(z) &= \sqrt{\frac{277z^3}{z(z-15)^2+9(2z-5)^2}}. \end{aligned} \tag{8}$$

A spherical harmonic Y_m^l represents the possible decay angular momentum states and their distribution in the helicity frame. As a function of the polar and aziumathal angles, the spherical harmonics can be written in terms of the associated Legendre polynomials, P_l^m:

$$Y_l^m(\theta^*, \phi^*) = \sqrt{\frac{2l+1}{4\pi}\frac{(l-m)!}{(l+m)!}}\ P_m^l(\cos\theta^*)\, e^{im\phi^*}. \tag{9}$$

$$P_l^m(x) = \frac{1}{2^l l!}\frac{d^l}{dx^l}\left([x^2-1]^l\right) \tag{10}$$

4.3. AVAILABLE RESONANCES

There are many possible background resonances that can contribute to this channel according to the world's data. Due to their narrower widths, the most obvious resonant contributions in the data are hyperons decaying to pK^-. However, a few meson resonances

that decay to $K\bar{K}$ are also possible. A third type of contribution considered is a non-interfering phase-space term constructed in the amplitude function as an extremely broad and spinless $K\bar{K}$ resonance.

TABLE 4.1. Notable hyperon resonances states that decay to pK^- and their masses and widths according to the Particle Data Group (Eidelman et al., 2004). All except the $\Lambda(1600)$ are four-star states.

	$L_{I,2J}$	Mass $[MeV]$	Width $[MeV]$
$\Lambda(1520)$	D_{03}	1519.5 ± 1.0	15.6 ± 1.0
$\Lambda(1600)$	P_{01}	$1560 - 1700$	$50 - 250$
$\Lambda(1670)$	S_{01}	$1660 - 1680$	$25 - 50$
$\Sigma(1670)$	D_{13}	$1665 - 1685$	$40 - 80$
$\Lambda(1690)$	D_{03}	$1685 - 1695$	$50 - 70$
$\Sigma(1775)$	D_{15}	$1770 - 1780$	$105 - 135$
$\Lambda(1820)$	F_{05}	$1815 - 1825$	$70 - 90$
$\Lambda(1830)$	D_{05}	$1810 - 1830$	$60 - 110$

TABLE 4.2. Notable meson resonances decaying to K^0K^- and their masses and partial widths according to the Particle Data Group (Eidelman et al., 2004). The last row is an artifical phase-space $K\bar{K}$ state used in this analysis.

	J^{PC}	Mass $[MeV]$	Width $[MeV]$
$a_0(980)$	0^{++}	984.7 ± 1.2	$50 - 100$
$a_2(1320)$	2^{++}	1318.1 ± 0.7	109.8 ± 2.4
$\rho_3(1690)$	3^{--}	1696 ± 4	204 ± 18
$KK(1200)$	0^{++}	$1000 - 1300$	> 1000

4.4. COMBINING AMPLITUDES

To describe the data, a sum of single amplitudes corresponding to different resonances is used. They correspond to well known hyperons which decay to pK^- and meson resonances decaying to $\bar{K}^0K^-$. The other component is a phase-space term, which assumes the same mathematical form as the meson resonances but with zero spin and a very large Breit-Wigner width.

A characterstic of likelihood fits is they cannot determine the value of an overall multiplicative parameter because the function being minimized is necessarily normalized to be

a probability density function with integral of unity. Thus, while each amplitude has its complex coeffecient C, the number of free real number parameters corresponding to those coeffecients is reduced by one to accomodate the unity integral. Another model parameter is removed by considering that only relative complex phases are relevant.

The single amplitudes defined in the previous section are complex numbers and can be added as such, allowing full interference between all resonances as in Equation 11. We also consider adding them all coherently, with equal complex phases and no interference as in Equation 12. A third possibility is to only allow mesons to interfere with mesons, and hyperons with hyperons, a combination of the two equations.

$$|A|^2 = |A_1 + A_2 + A_3 + \cdots|^2 \tag{11}$$

$$|A|^2 = |A_1|^2 + |A_2|^2 + |A_3|^2 + \cdots \tag{12}$$

4.5. LIKELIHOOD FITTING

To fit the model to the data, an unbinned, event-based maximum likelihood technique is used. The likelihood is a function of the model's parameters, $\vec{p}$, and the data's variables, $\vec{x}$, and is defined as the product of the probability density over all N data events.

$$\mathcal{L}(\vec{p}) = \left[\frac{N_0^N}{N!}e^{-N_0}\right]\prod_{i=1}^{N} pdf(\vec{p}, \vec{x}_i) \tag{13}$$

The bracketed coefficient is the Poisson probability of measuring N events given an expectation value of N_0 events. N_0 is calculated from the integral of the probability distribution function.

The probability density for one event is proportional to the model amplitude's magnitude squared, with an effeciency factor, ϵ, dependent on the kinematic variables. The

normalization integral in the denominator assures the propability density function's integral over the entire phase-space to be one.

$$pdf\,(\vec{p},\vec{x}) = \frac{|A(\vec{x},\vec{p})|^2\,\epsilon(\vec{x})}{\int |A(\vec{x}\,',\vec{p})|^2\,\epsilon(\vec{x}\,')\,d\vec{x}\,'} \tag{14}$$

In order for the parameter uncertainties to be correct, the quantity minimized by Minuit is actually twice the negative of the likelihood's logarithm (James and Roos, 1975). Then the product over events in Equation 13 becomes a summation, and the denominator's normalization integral can be written as a separate term:

$$\log \mathcal{L}(\vec{p}) = \sum_{i=1}^{N} \log\left(|A(\vec{x}_i,\vec{p})|^2\,\epsilon(\vec{x}_i)\right) - N \log \int |A(\vec{x}\,',\vec{p})|^2\,\epsilon(\vec{x}\,')\,d\vec{x}\,' \tag{15}$$

The normalization integral in the second term is calculated via numerical methods. It can first be rewritten as a sum over N_g Monte Carlo events generated uniformly thoughout the phase-space volume, $\int d\vec{x}\,'$.

$$\int |A(\vec{x},\vec{p})|^2\,\epsilon(\vec{x})\,d\vec{x} \simeq \left[\frac{1}{N_g}\sum_{i=1}^{N_g} |A(\vec{x}_i,\vec{p})|^2\;\epsilon(\vec{x}_i)\right] \int d\vec{x}\,' \tag{16}$$

The effeciency, ϵ, is accounted for by processing the phase-space events through CLAS's GEANT detector simulation. Events that are successfully reconstructed are assigned an effeciency of one, otherwise zero. The normalization integral can then be written as a sum over the N_r reconstructed phase-space events:

$$\int |A(\vec{x},\vec{p})|^2\,\epsilon(\vec{x})\,d\vec{x} \simeq \left[\frac{1}{N_g}\sum_{i=1}^{N_r} |A(\vec{x}_i,\vec{p})|^2\right] \int d\vec{x}\,' \tag{17}$$

The $\int d\vec{x}\,'$ volume integral is dependent only on the kinematic boundaries, and thus only need be calculated once; the standard accept-reject integration technique is employed here.

The full form of the logarithm of the likelihood can then be written as

$$\log \mathcal{L}(\vec{p}) = \sum_{i=1}^{N} \log(|A(\vec{x}_i,\vec{p})|^2) - N \log\left[\frac{1}{N_g}\sum_{i=1}^{N_r} |A(\vec{x}_i,\vec{p})|^2\right] \int d\vec{x}\,'. \tag{18}$$

As they are dependent on the values of the model parameters, the sums over N data events and N_r simulated events must be recalculated for every minimization step by Minuit. The size of the data is small enough to allow all these events' kinematics to be stored in computer memory during the minimization and not reread from disk. The fit convergence quality can be estimated by plotting the likelihood as a function of the parameters. The χ^2 can also be calculated, but that quantity is not necessarily minimized when the likelihood is maximized and is only an estimate of the fit quality.

CHAPTER 5

APPLYING THE MODEL

5.1. TESTING THE METHOD

To fit the model to the data, an unbinned event-based technique is desirable in order to use information from multiple dimensions. This also avoids binning complications. The unbinned maximum-likelihood formalism is described in Section 4.5. Before attempting to fit the real data with a complex multi-dimensional model, the likelihood technique is tested against the standard χ^2 minimization using simpler probability distribution functions. Fake data is generated according to a known distribution, $g(\vec{x}, \vec{p})$, and then that same distribution with free parameters is fit to the data using both methods. In this case, there is no detector and thus the effeciency is one, resulting in a simpler form of the likelihood:

$$\log \mathcal{L}(\vec{p}) = \log \sum_{i=1}^{N} g(\vec{x}_i, \vec{p}) - N \log \int g(\vec{x}\,', \vec{p})\, d\vec{x}^{\,prime} \tag{19}$$

The χ^2 function to be minimized can be written as follows, where n_i is the number of events in the i^{th} bin of the histogram and σ_i its uncertainty.

$$\chi^2 = \sum_{i=1}^{N} \frac{(n_i - g(\vec{x}_i, \vec{p}))^2}{\sigma_i} \tag{20}$$

One practical difference between the χ^2 and likelihood methods is that the latter requires evaluation of the distribution's integral (the second term in Equation 19). This is because the likelihood is necessarily a function of a probability distribution with integral one. This integral is calculated using different methods and compared. When the integral can be written analytically, it is used to compare with numerical methods.

The test functions include an exponential, $e^{-\tau x}$, a two-parameter ratio of polynomials $(1 + \alpha x + \beta x^2)/(1 + \beta/3)$, a Gaussian, and both non-relativistic and relativistic Breit-Wigner distributions. In all cases the likelihood method tends to find the real parameters more precisely than the χ^2 method.

Additionally, a two-dimensional case is tested using the likelihood method with a Breit-Wigner distribution in each of two Dalitz mass variables simultaneously. This is done first with an artificial square phase-space and then with the a physical phase-space distribution of a two-particle decay.

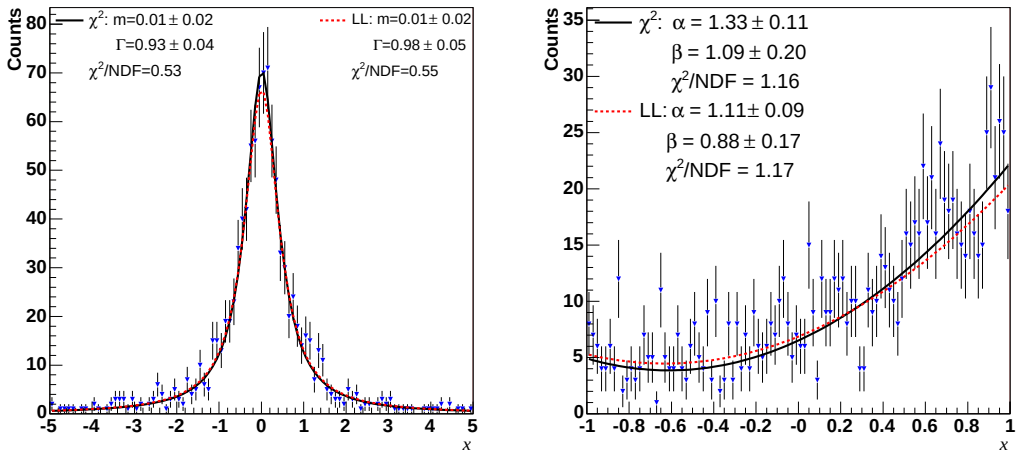

FIGURE 5.1. A sample fit of a non-relativistic Breit-Wigner distribution (left) and a ratio of polynomials (right) using binned χ^2 minimization and unbinned likelihood maximization.

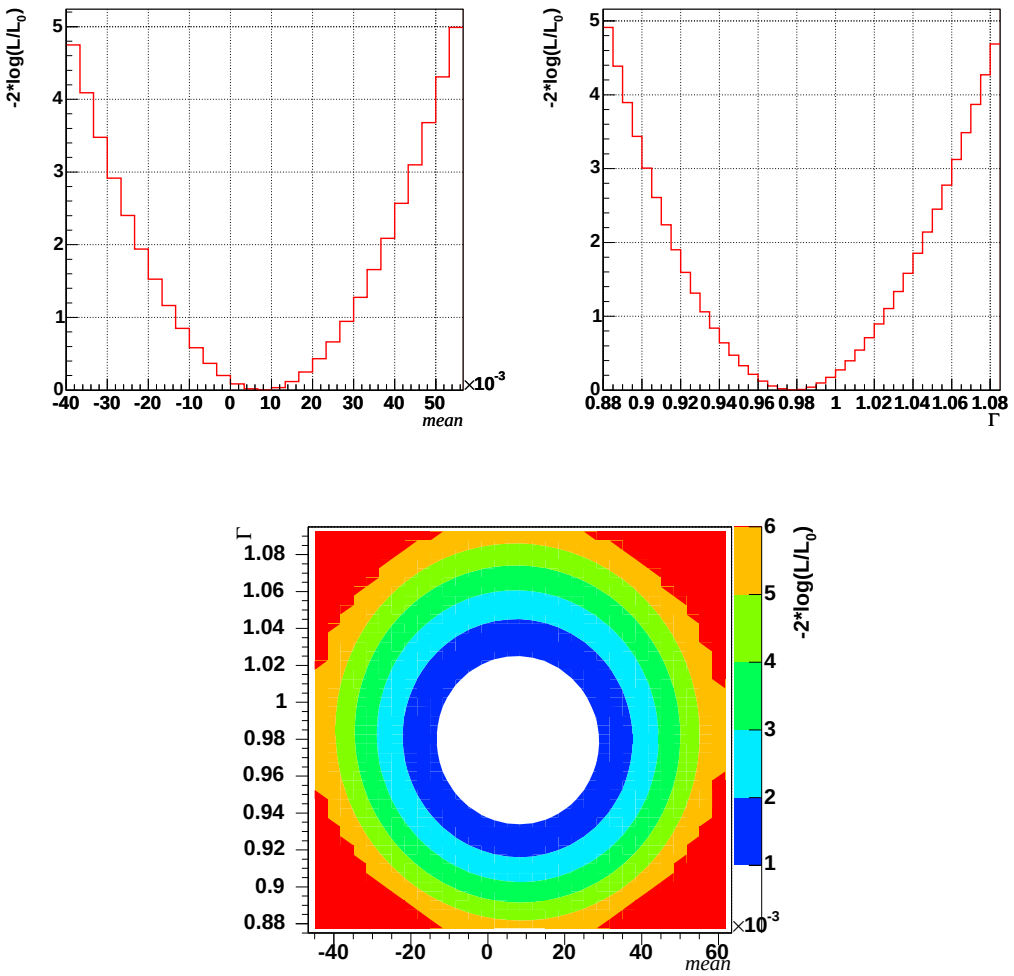

FIGURE 5.2. The likelihood for a single test experiment as function of the two Breit-Wigner fit parameters, the mean and width (Γ). The N-σ confidence level contours are shown in the two-dimensional plot.

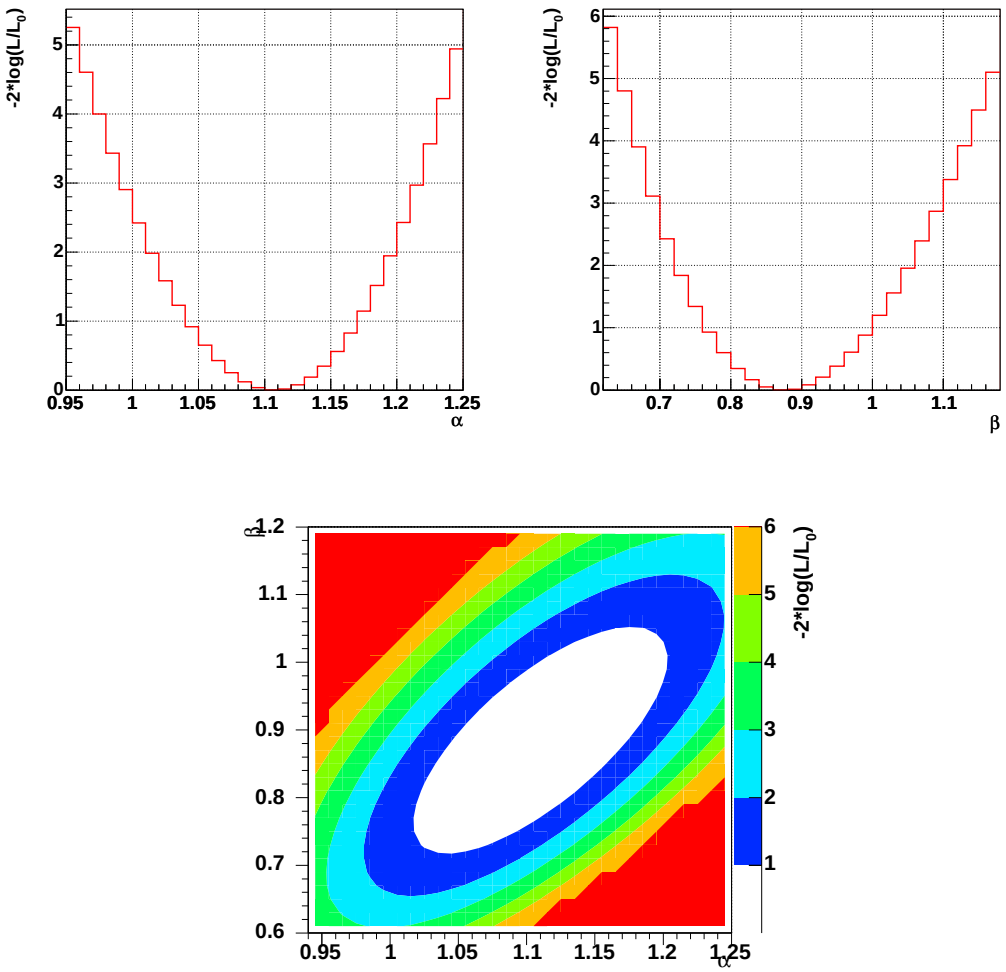

FIGURE 5.3. The likelihood for a single test experiment as function of the two polynomial fit parameters, α and β. The N-σ confidence level contours are shown in the two-dimensional plot.

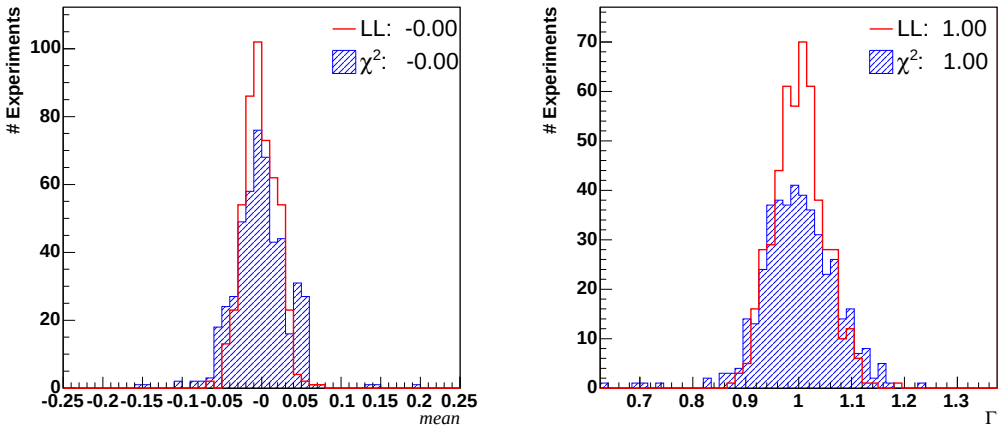

FIGURE 5.4. The parameter results of generating and fitting 500 Monte Carlo data sets with a Breit-Wigner distribution. Both the likelihood and χ^2 methods give parameter distributions centered around the expected value, but the unbinned likelihood method gives more precise results.

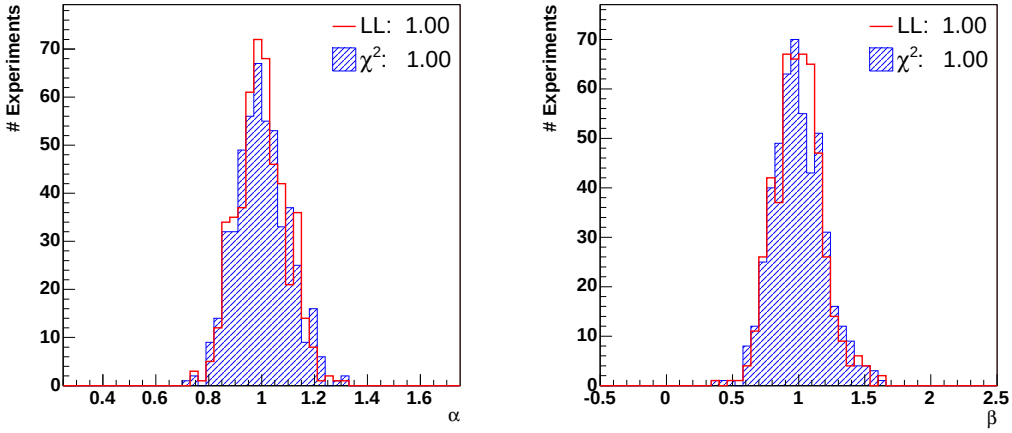

FIGURE 5.5. The parameter results of generating and fitting 500 Monte Carlo data sets with a ratio of polynomials distribution.

5.2. PDF NORMALIZATION

The likelihood function requires our model description to be a probabilty density function with unity integral. Thus, the integral of our amplitude function, the last term in Equation 18, must be recalculated every time the parameters change. As explained in 4.5, the detector effeciency can be accounted for in this integral by using phase-space events that have been processed through CLAS's GEANT detector simulation.

The phase-space events for normalization calculation are designed to be similar to the real setup. Three-body phase-space event kinematics are generated by sampling the known beam and target conditions. First, the energy spectrum of the Bremsstrahlung beam photons is sampled according to a $1/E_\gamma^2$ distribution in the range $1.6 < E_\gamma < 3.6\ GeV$. The target neutron momentum is sampled according to the Bonn potential. This determines the $\gamma - n$ rest frame from which 3-body phase-space kinematics are generated for pK^0K^- according to ROOT's TGenPhaseSpace class (Brun and Rademakers, 1997). The two pions decaying from K_s^0 are generated isotropically with equal and opposite momenta of $206\ MeV/c$ in their mother's rest frame.

The distribution of phase-space events are shown in Figure 5.6 as a function of the Dalitz variables and total center of mass energy. These generated events can then be processed through CLAS's GEANT detector simulation and reconstruction analysis. They are then ready for use in the likelihood's nomalization integrals and detector efficiency calculations.

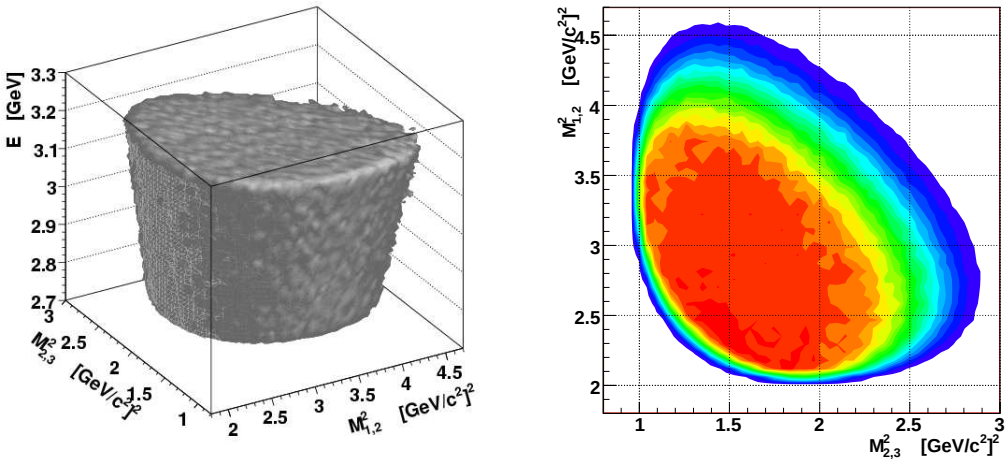

FIGURE 5.6. Uniformly distributed phase-space events as a function of the two Dalitz mass variables and the total center of mass energy.

5.3. DETECTOR EFFECIENCY

The background model as defined in Chapter 4 is our description of what enters the spectrometer as a result of $\gamma - n$ interactions. The yields of the raw data as measured in the anlysis are seen through the "eyes" of the detector. The link between the two is the detector effeciency, and it must be accounted for in order to compare the data and model. In the fitting technique, the efficiency was incorporated by performing the normalization integrals over detector-simulated phase-space events.

The detector efficiency is defined as the ratio of the number of events that are detected and reconstructed with the spectrometer system and analysis software to the number of events that were actually generated by the beam-target interaction. The real data only contains direct information about the former type of events, those that successfully "pass" through the reconstruction algorithm. With a Monte-Carlo simulation of the detector system, we also know how many events fail to get reconstructed, N_{fail}. Assuming the "fail" and "pass" events are independent, the efficiency and its uncertainty can be written as:

$$\epsilon = \frac{N_{pass}}{N_{fail} + N_{pass}}, \tag{21}$$

$$\Delta\epsilon = \sqrt{\frac{(1-\epsilon)\epsilon}{N_{fail} + N_{pass}}}\,. \tag{22}$$

The "phase-space" model's efficiency is calculated using Equation 21 and Equation 22 and a three-body phase-space simulation from Section 5.2. In calculating the efficiency for our physics model, there are two weighting methods available. One is to generate a sufficient number of phase-space events already weighted by the amplitude, and then apply the detector simulation. The other is to use simulated phase-space events, but then weight the generated and reconstructed events independently. The latter method is preferable because the efficiency can be recalculated as the model changes without requiring additional computer simulations. The effective difference is due primarily to binning effects, which should be negligible in the case of a four-particle final state covering a large range of kinematics.

In the following plots, the “old” model’s efficiency is calculated using the full simulation method, while the “new” model’s efficiency uses the post-simulation weighting of phase-space events.

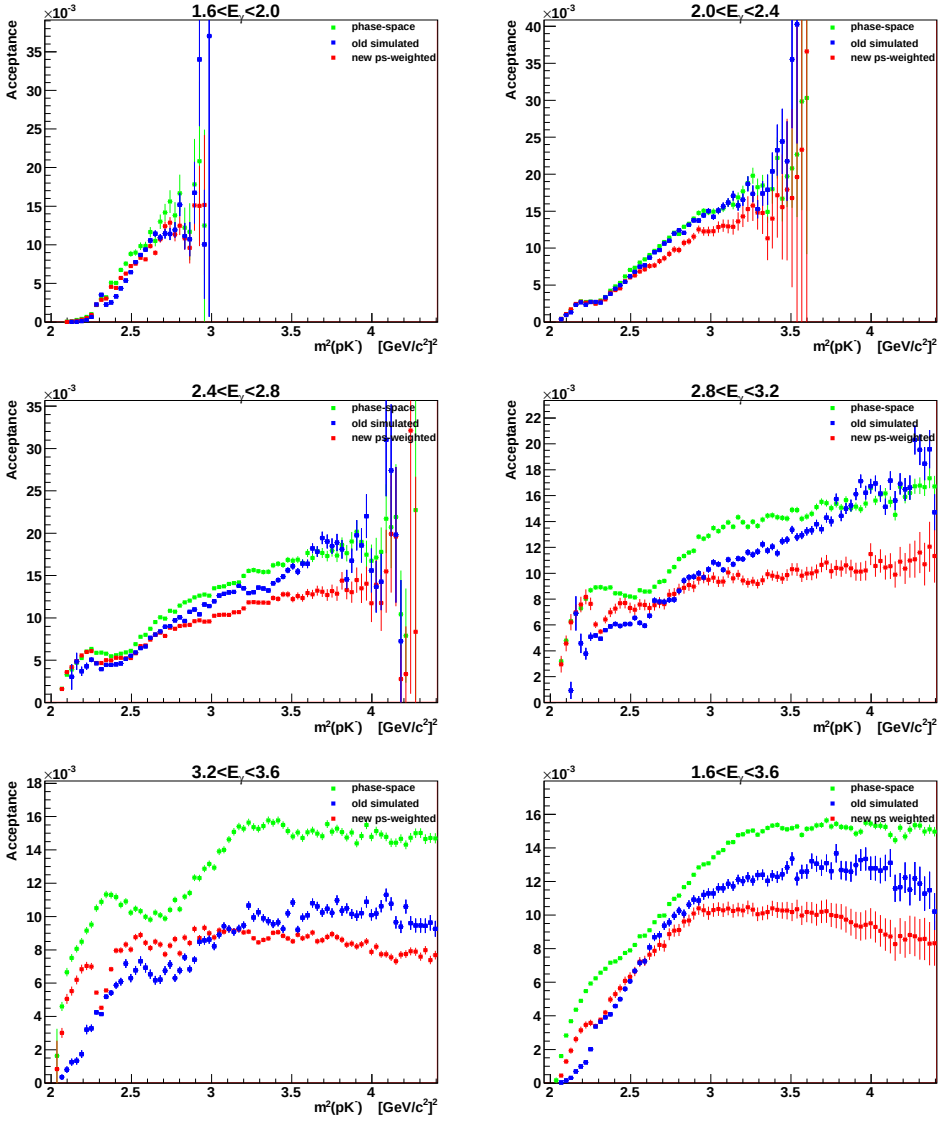

FIGURE 5.7. Efficiency as a function of the invariant mass of the pK^- system for 3-body phase-space (green), the “old” model (blue), and the “new” model (red).

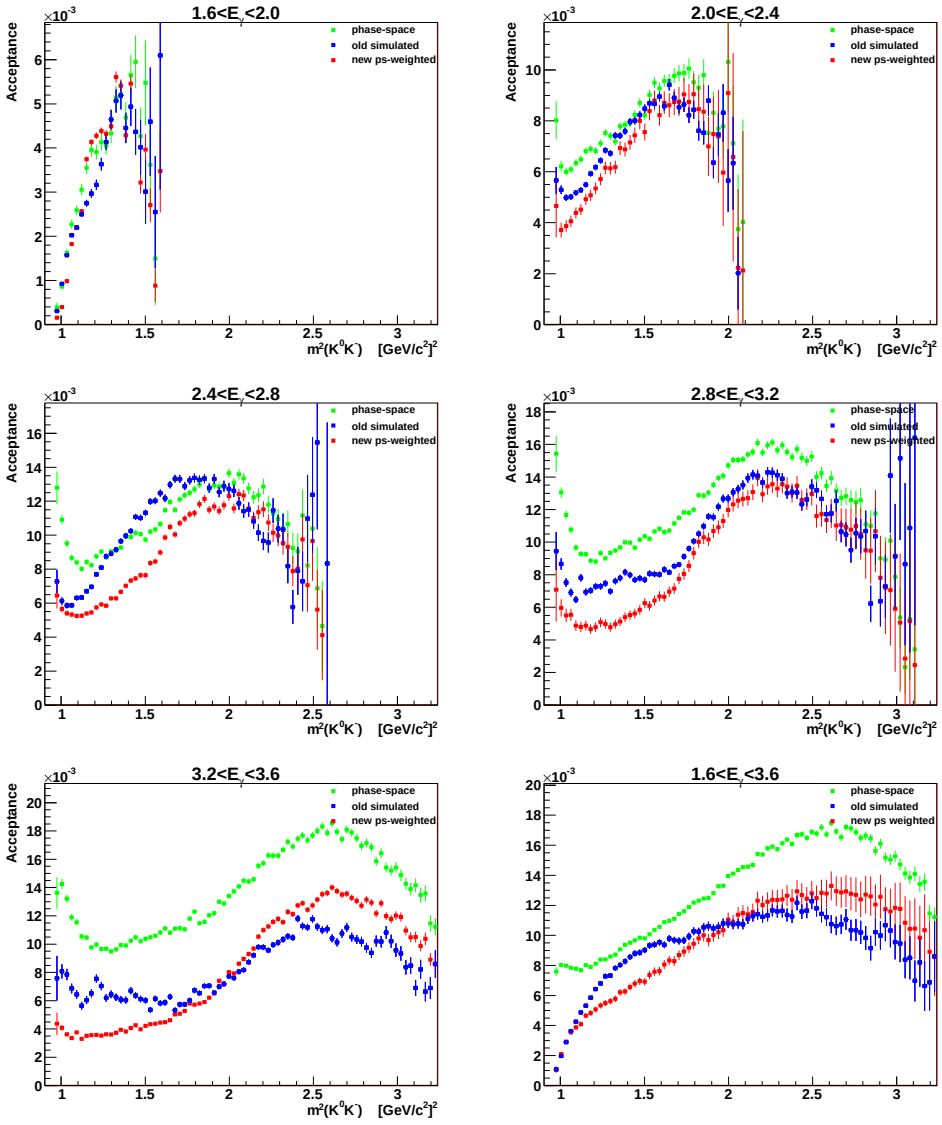

FIGURE 5.8. Efficiency as a function of the invariant mass of the K^0K^- system for 3-body phase-space (green), the "old" model (blue), and the "new" model (red).

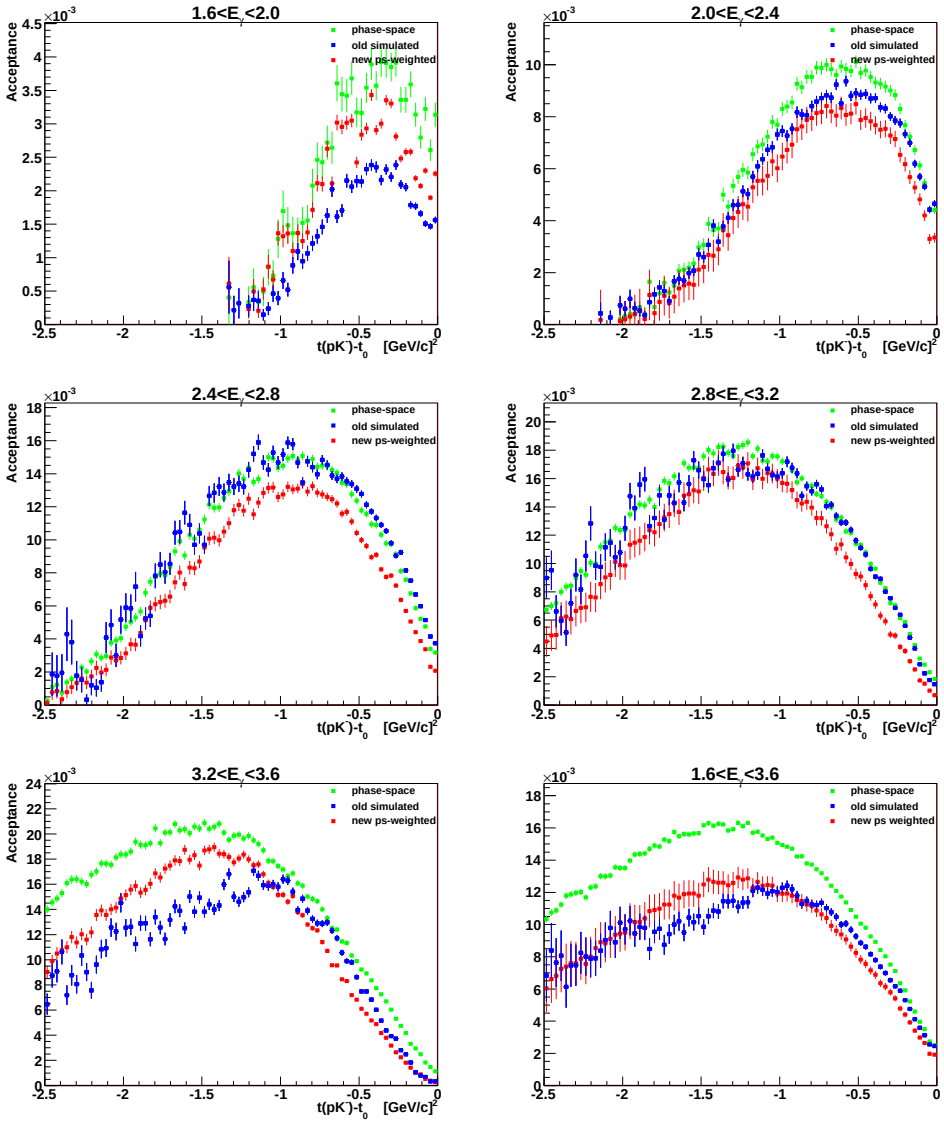

FIGURE 5.9. Efficiency as a function of the momentum transfer from the target nucleon to the pK^- system for 3-body phase-space (green), the "old" model (blue), and the "new" model (red).

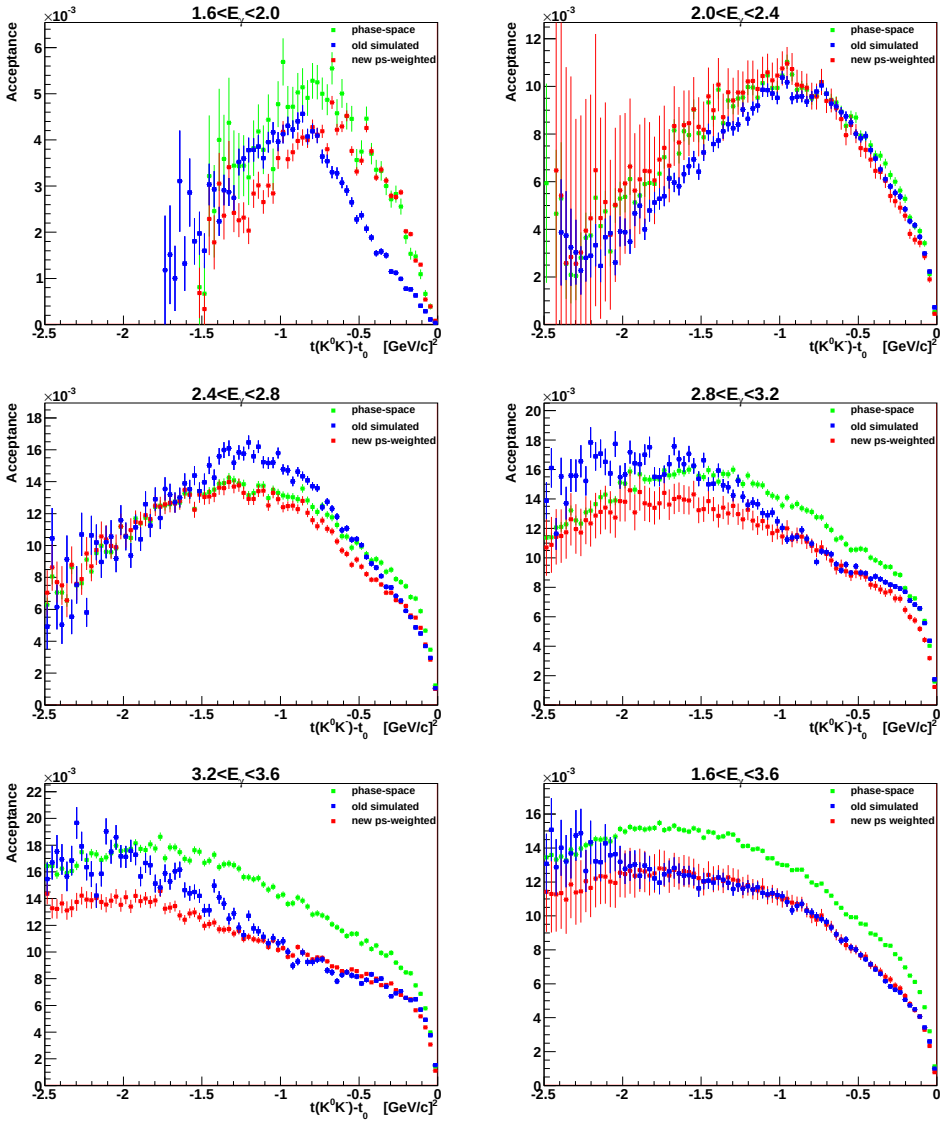

FIGURE 5.10. Efficiency as a function of the momentum transfer from the beam photon to the K^0K^- system for 3-body phase-space (green), the "old" model (blue), and the "new" model (red).

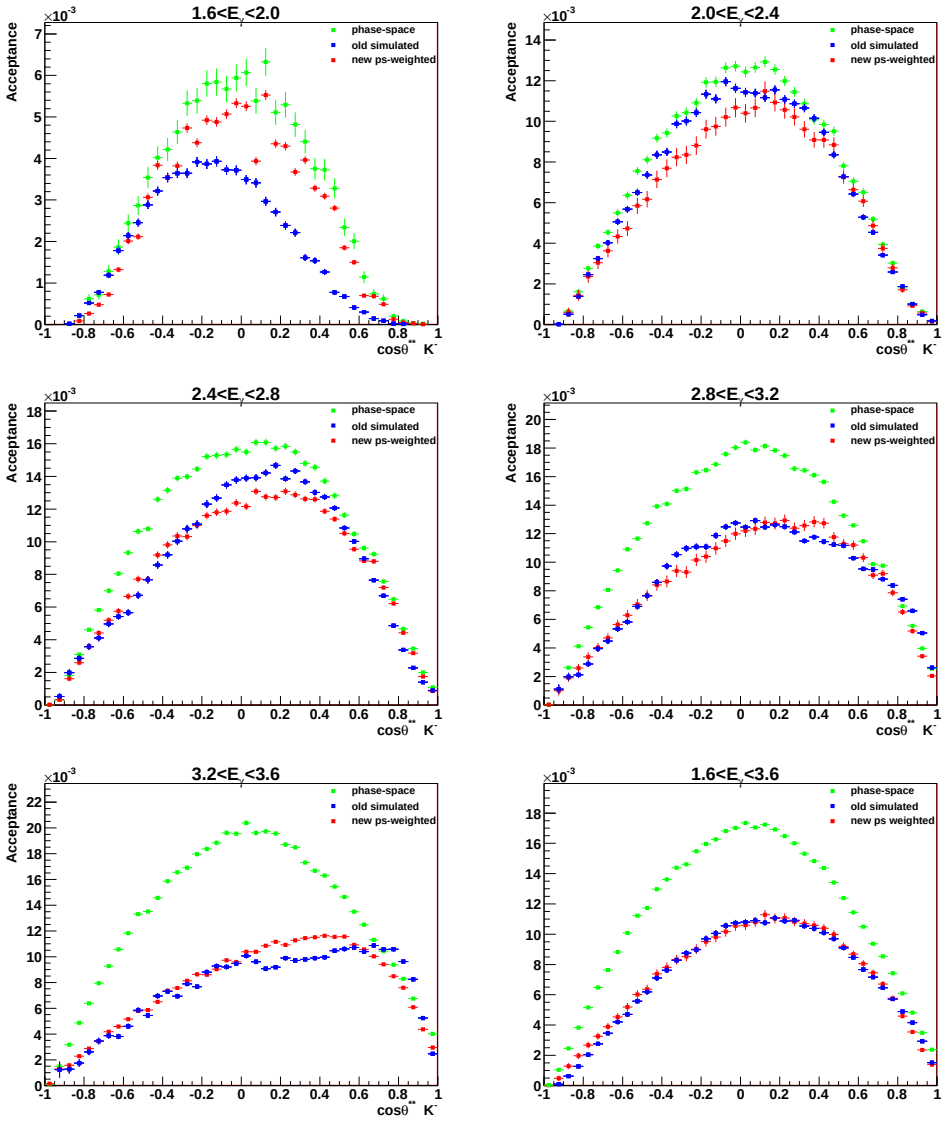

FIGURE 5.11. Efficiency as a function of the polar angle of the K^- in the pK^- helicity frame for 3-body phase-space (green), the "old" model (blue), and the "new" model (red).

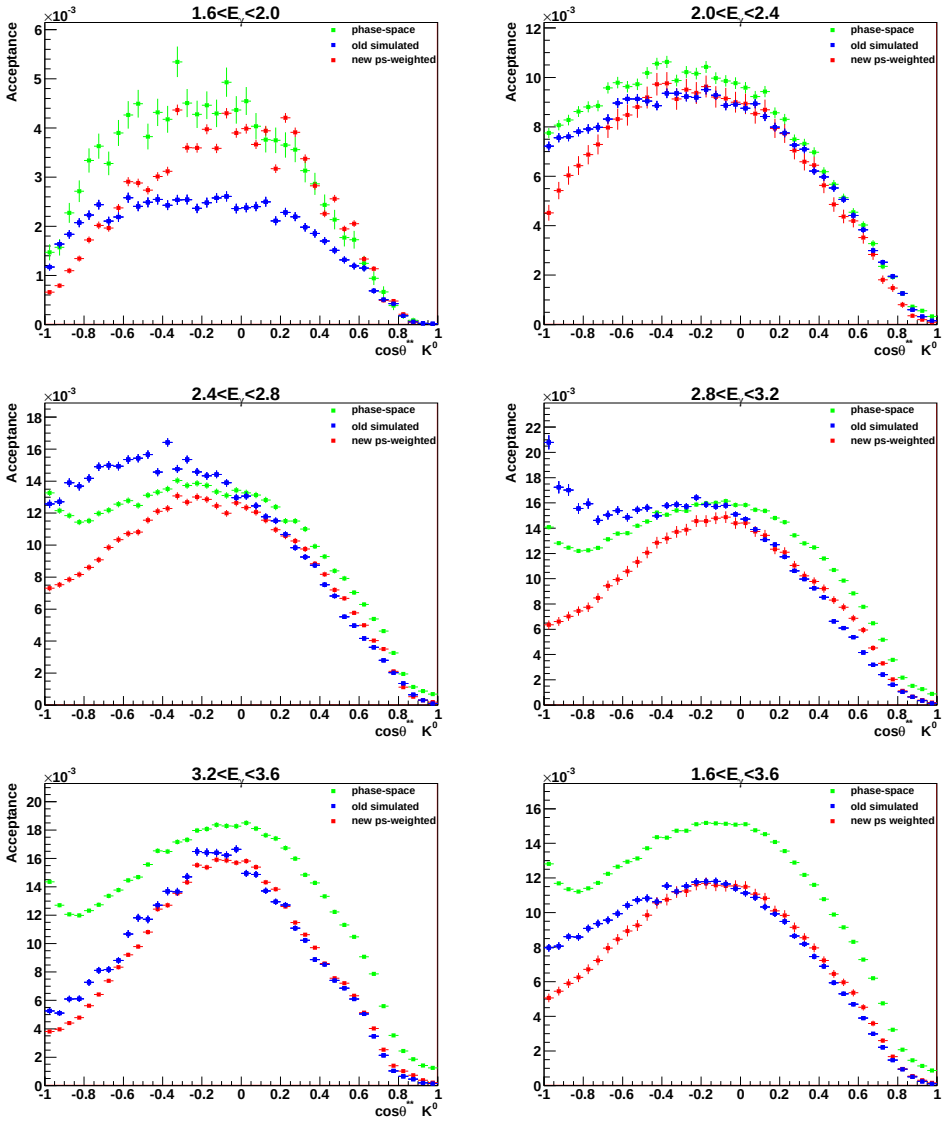

FIGURE 5.12. Efficiency as a function of the polar angle of the K^0 in the K^0K^- helicity frame for 3-body phase-space (green), the "old" model (blue), and the "new" model (red).

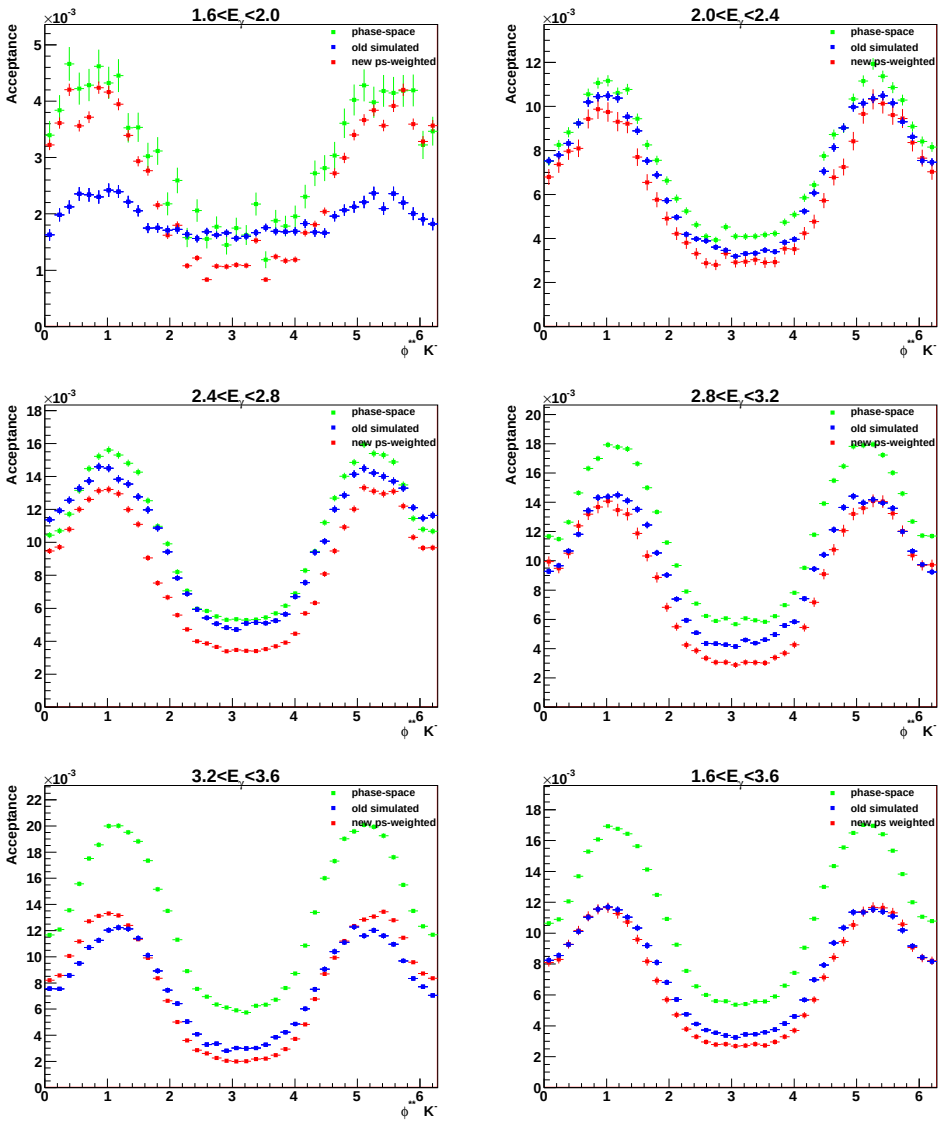

FIGURE 5.13. Efficiency as a function of the azimuthal angle of the K^- in the pK^- helicity frame for 3-body phase-space (green), the "old" model (blue), and the "new" model (red).

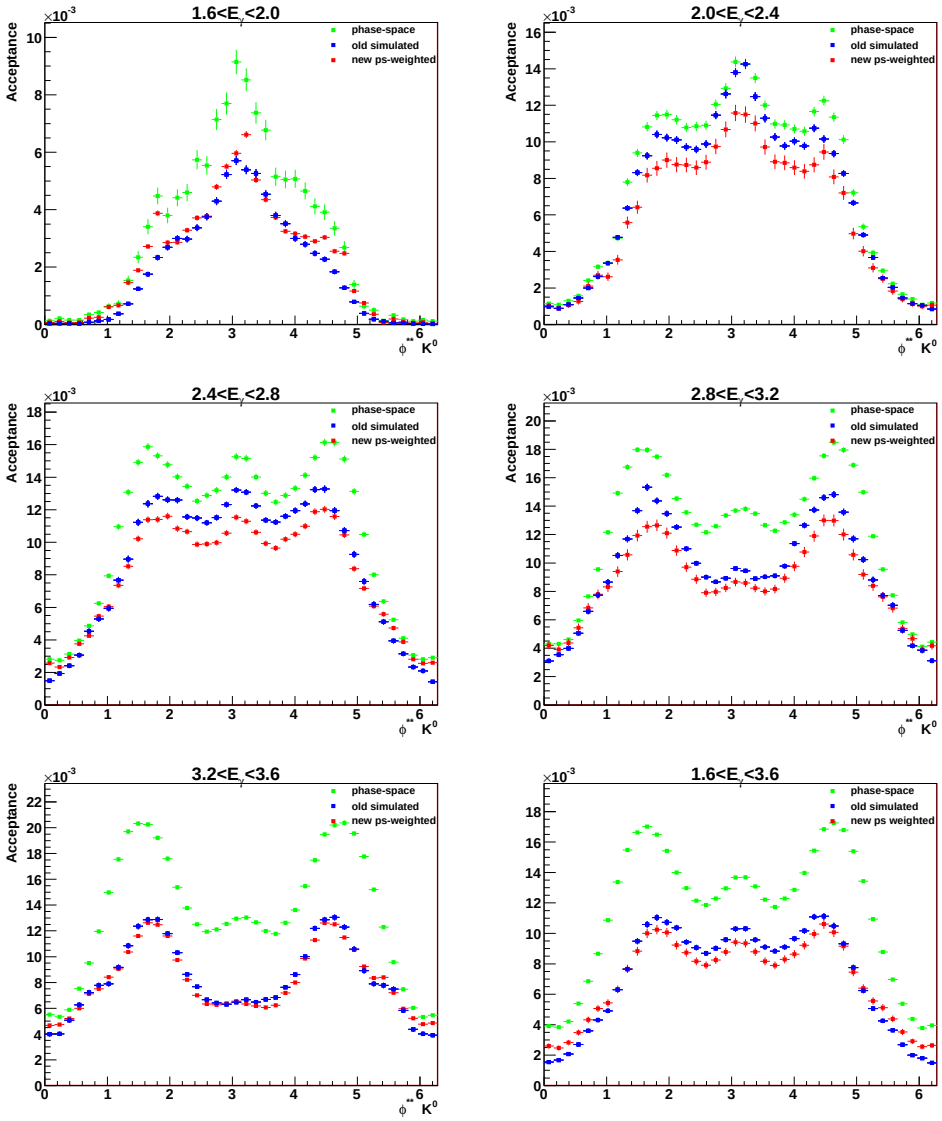

FIGURE 5.14. Efficiency as a function of the azimuthal angle of the K^0 in the K^0K^- helicity frame for 3-body phase-space (green), the "old" model (blue), and the "new" model (red).

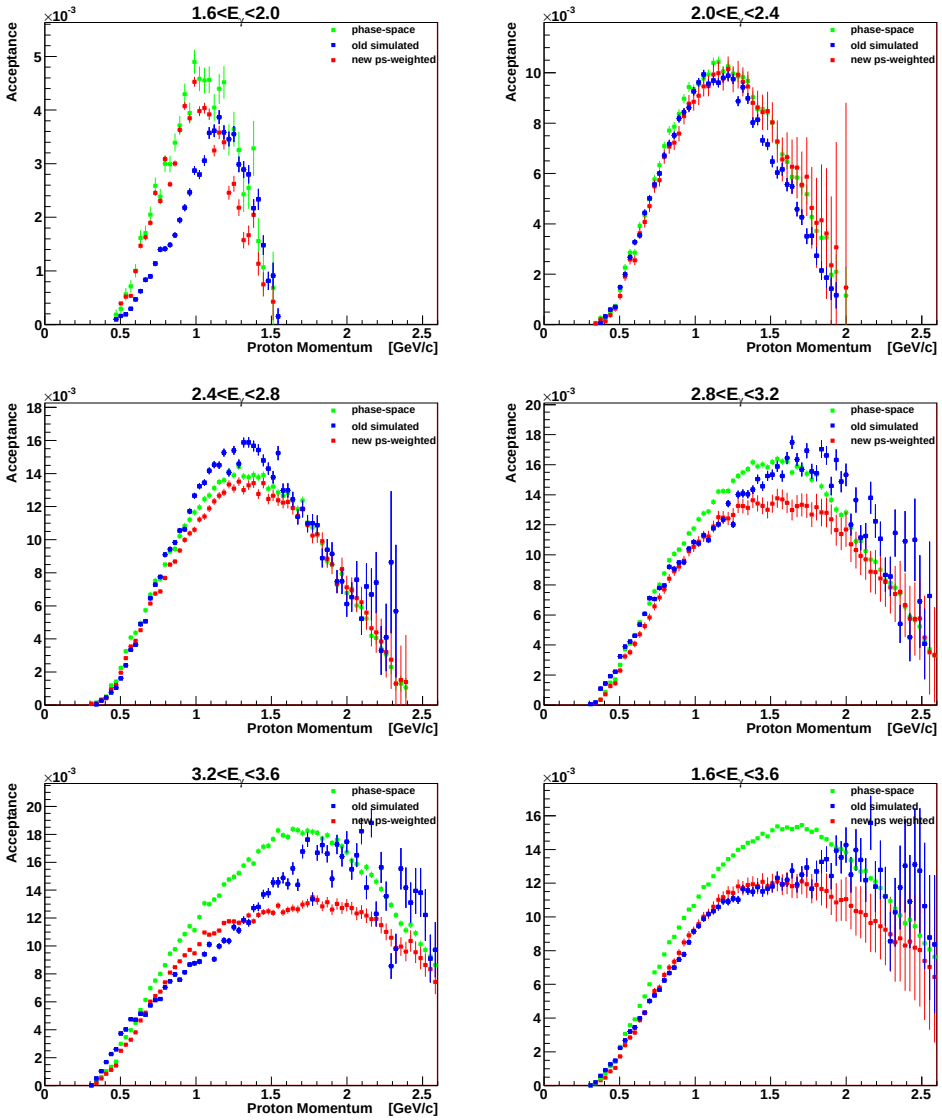

FIGURE 5.15. Efficiency as a function of the lab momentum of the detected proton for 3-body phase-space (green), the "old" model (blue), and the "new" model (red).

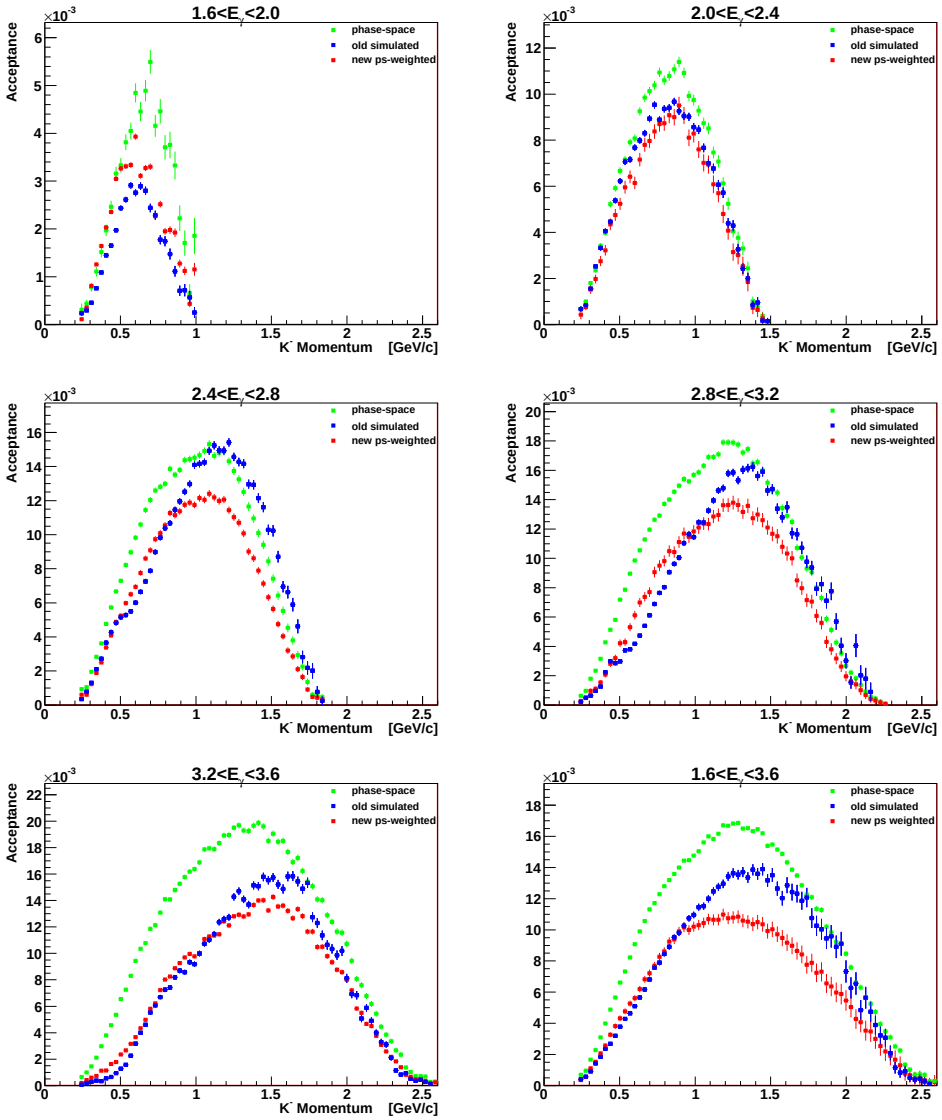

FIGURE 5.16. Efficiency as a function of the lab momentum of the K^- for 3-body phase-space (green), the "old" model (blue), and the "new" model (red).

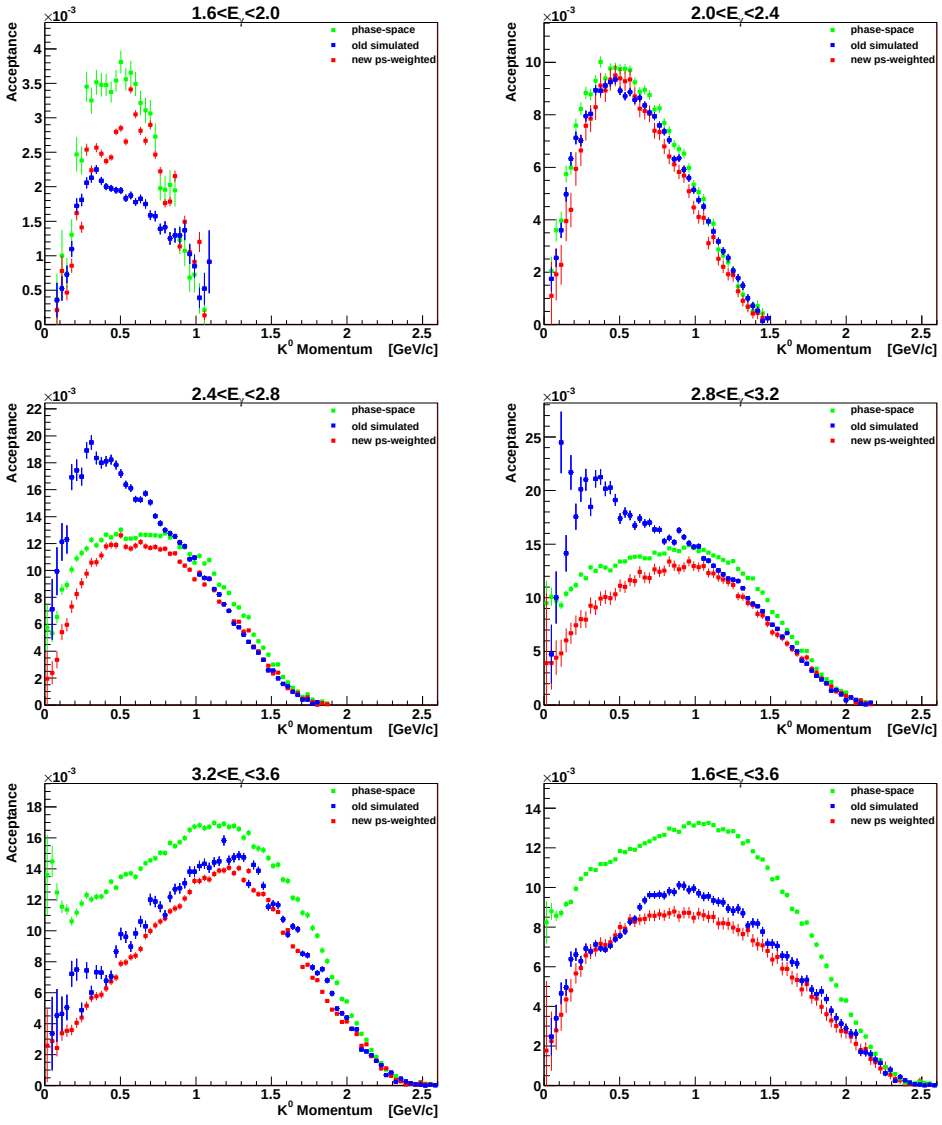

FIGURE 5.17. Efficiency as a function of the lab momentum of the K^0 for 3-body phase-space (green), the "old" model (blue), and the "new" model (red).

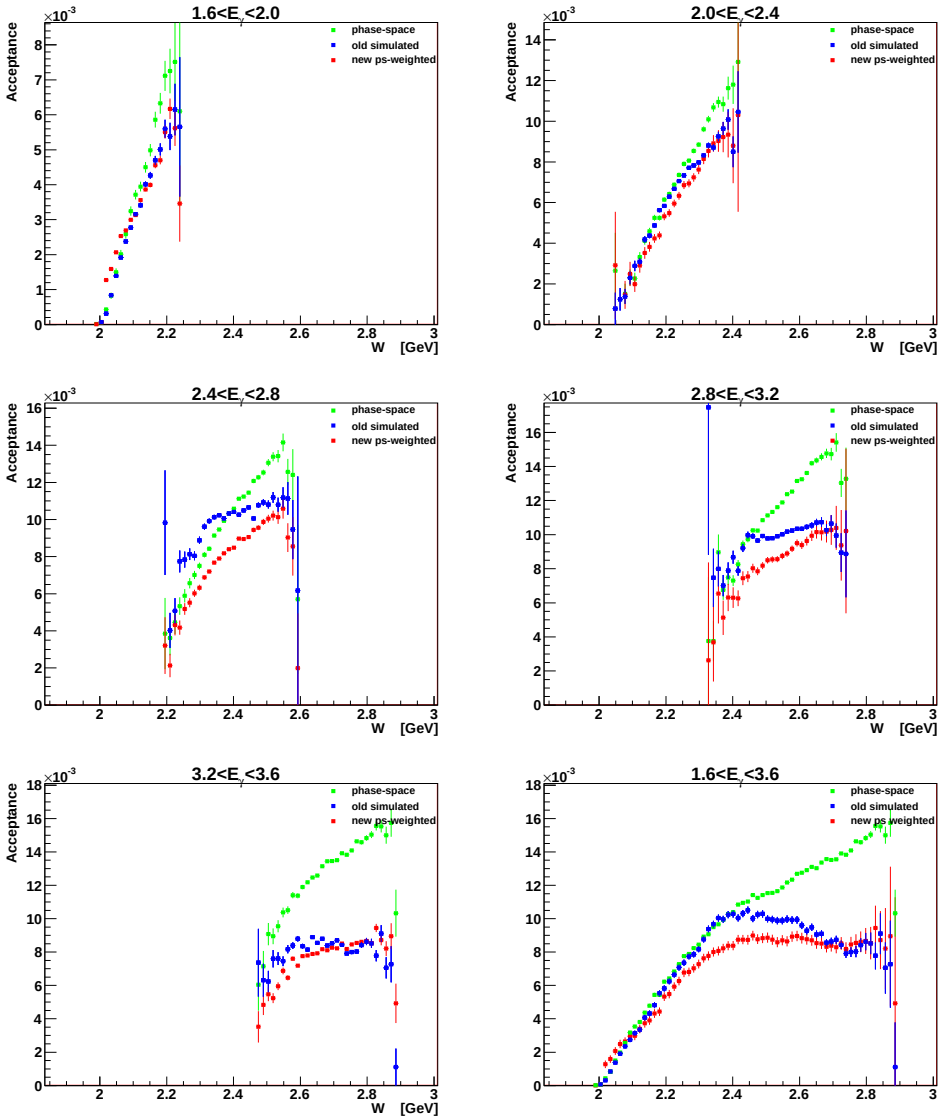

FIGURE 5.18. Efficiency as a function of the total energy $w = \sqrt{s}$ of the reaction $\gamma n \rightarrow pK^0K^-$ for 3-body phase-space (green), the "old" model (blue), and the "new" model (red).

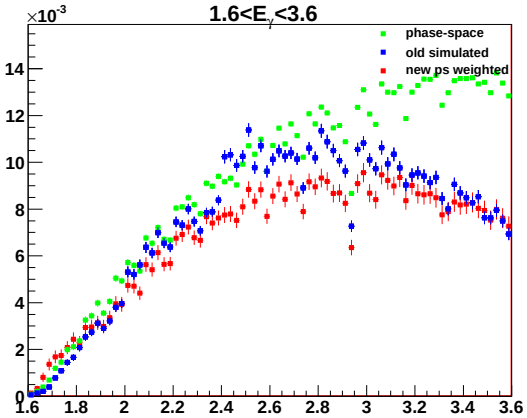

FIGURE 5.19. Efficiency as a function of the lab photon energy for 3-body phase-space (green), the "old" model (blue), and the "new" model (red).

5.4. FITTING THE REAL DATA

The model has no explicit dependence on the total energy of the reaction. Including one would increase the number of free parameters; there could even be a separate energy dependence for each resonance. Instead, it was chosen to divide the data into energy bins and fit each set of events independently. The bin size is chosen at $400\ MeV$, starting at $1.6\ GeV$, near threshold for $\Theta^+(1540)$ production, up to the maximum beam energy of $3.6\ GeV$. Statistics prevent using a smaller bin size.

The lowest photon energy bin ($1.6 - 2.0\ GeV$) is below threshold for all the possible resonances except $\Lambda(1520)$ and $\rho(980)$. This makes for a simple amplitude function relative to the higher energies. Thus, this lowest energy bin is fit first, and the resulting parameters are used as a starting point for the next higher energy bin. This algorithm is then applied iteratively for increasing energy bins with the inclusion of additional resonances.

The momentum trasfer factor $e^{\beta(t-t_0)}$ contains one parameter, β. This parameter is manually adjusted by scanning through possible values and calculating the likelihood. A mapping of the likelihood as a function of β for hyperons and mesons. Values of 1.5 and 2.0 respectively are chosen and remain fixed in the model.

5.4.1. "Old" Complex Model. Ideally, the full complex model amplitude of Equation 4 and all resonances from Table 4.1 and Table 4.2 with all their allowed m-states would be included in the fitting function. Minuit would be free to determine all of the coeffecients. However, the large width of the photon energy bins and limited statistics makes this impractical. Instead, the fit is initially performed with a small subset of the possible m-states, and combination with the largest value of the likelihood after minimization is taken as the best fit.

Interference is allowed between hyperons and mesons separately, but not between the two subsets of resonances. For reference, this model is named "old". In the bins of largest energy, the number of amplitudes becomes large and the resulting fit unsatisfactory and unstable. This lead to further modification of the model in the next section.

TABLE 5.1. Resonant states in the "old". The hyperons are all four-star PDG states listed with their partial wave $L_{I,2J}$, and the mesons are listed with their J^{PC} quantum numbers.

$\Lambda(1520)$	D_{03}
$\Lambda(1600)$	P_{01}
$\Lambda(1670)$	S_{01}
$\Sigma(1670)$	D_{13}
$\Lambda(1690)$	D_{03}
$\Sigma(1775)$	D_{15}
$\Lambda(1820)$	F_{05}
$\Lambda(1830)$	D_{05}
$a_0(980)$	0^{++}
$a_2(1320)$	2^{++}
$\rho_3(1690)$	3^{--}

5.4.2. "New" Simplified Model. There is no obvious evidence of resonances in the integrated $K\bar{K}$ invariant mass. Some of its shape is found to be due to the narrow $\Lambda(1520)$ reflecting into large values of $m(K\bar{K})$, as seen in Figure 5.24. When meson resonances are included in the model, the fit result is visually unsatisfactory in the $K\bar{K}$ invariant mass, especially in the highest photon energy bins. This lead to using only one very broad $K\bar{K}$ Breit-Wigner to approximate all possible meson resonance contributions.

This final model choice includes no real meson resonances, but only a very broad, spinless $K\bar{K}$ state. The hyperon amplitudes are added as in Equation 12 such that there is no interference. In addition, the spherical harmonic term is dropped from the amplitude function. Remaining is the relativistic Breit-Wigner multiplied by an exponential momentum trasfer factor for each resonance. This model will be referred to as "new".

5.5. DATA AND MODEL COMPARISONS

5.5.1. Raw Yields. The raw data yields can be directly compared to an efficiency-corrected model. To compute the efficiency for the "new" model, the phase-space effeciency is reweighted as in Section 5.3. For the "old" model, the phase-space events were weighted before detector simulation. The following plots contain the raw data superimposed with three model descriptions, each corrected by its own efficiency.

TABLE 5.2. Resonant states allowed in the "new" model. The hyperons are all four-star PDG states listed with their partial wave $L_{I,2J}$.

$\Lambda(1520)$	D_{03}
$\Lambda(1600)$	P_{01}
$\Lambda(1670)$	S_{01}
$\Sigma(1670)$	D_{13}
$\Lambda(1690)$	D_{03}
$\Sigma(1775)$	D_{15}
$\Lambda(1820)$	F_{05}
$\Lambda(1830)$	D_{05}
$KK(1200)$	

TABLE 5.3. Parameter values for the "new" model and photon energy range $1.6 < E_\gamma < 2.0\,GeV$ after fitting to the data.

	Mass $[MeV]$	Width $[MeV]$	Normalization	t-slope
$\Lambda\ D_{03}$	1515	13.6	1.000	2.0
KK	1100	2000	3.383	1.5

TABLE 5.4. Parameter values for the "new" model and photon energy range $2.0 < E_\gamma < 2.4\,GeV$ after fitting to the data.

	Mass $[MeV]$	Width $[MeV]$	Normalization	t-slope
$\Lambda\ D_{03}$	1519	12.6	0.213	2.0
$\Lambda\ D_{03}$	1701	55.4	0.169	2.0
$\Sigma\ D_{15}$	1762	75.0	0.131	2.0
KK	1300	2000	1.000	1.5

TABLE 5.5. Parameter values for the "new" model and photon energy range $2.4 < E_\gamma < 2.8\,GeV$ after fitting to the data.

	Mass $[MeV]$	Width $[MeV]$	Normalization	t-slope
$\Lambda\ D_{03}$	1518	12.6	0.465	2.0
$\Lambda\ D_{03}$	1698	88.3	0.255	2.0
$\Sigma\ D_{15}$	1760	75.0	0.265	2.0
$\Lambda\ D_{05}$	1820	108.9	0.434	2.0
KK	1300	2000	2.000	1.5

TABLE 5.6. Parameter values for the "new" model and photon energy range $2.8 < E_\gamma < 3.2\ GeV$ after fitting to the data.

	Mass $[MeV]$	Width $[MeV]$	Normalization	t-slope
$\Lambda\ D_{03}$	1518	12.6	0.287	2.0
$\Sigma\ D_{15}$	1760	119.0	0.193	2.0
$\Lambda\ F_{05}$	1800	86.7	0.193	2.0
$\Lambda\ D_{05}$	1835	87.0	0.216	2.0
$K\bar{K}$	1400	2000	1.000	1.5

TABLE 5.7. Parameter values for the "new" model and photon energy range $3.2 < E_\gamma < 3.6\ GeV$ after fitting to the data.

	Mass $[MeV]$	Width $[MeV]$	Normalization	t-slope
$\Lambda\ D_{03}$	1520	12.6	0.870	2.0
$\Lambda\ F_{05}$	1805	110.0	0.650	2.0
$\Lambda\ D_{05}$	1842	135.3	0.951	2.0
$K\bar{K}$	1400	2000	3.000	2.0

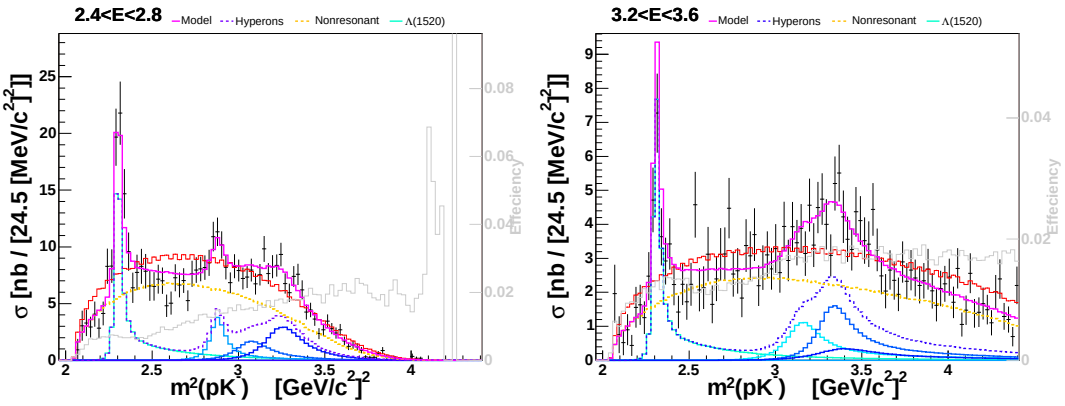

FIGURE 5.20. Invariant mass of the pK^- system, showing the decomposition of individual resonance contributions for the "new" model. The total fit is drawn in magenta, the individual hyperon resonances are shades of blue, and the nonresontant $K\bar{K}$ component is orange.

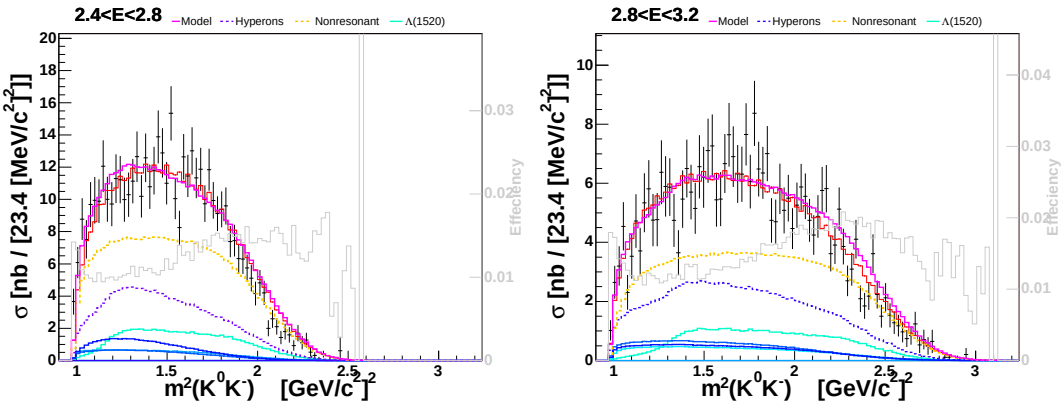

FIGURE 5.21. Invariant mass of the K^-K^0 system, showing the decomposition of individual resonance contributions for the "new" model. The total fit is drawn in magenat, the individual hyperon resonances are shades of blue, and the nonresontant $K\bar{K}$ component is orange.

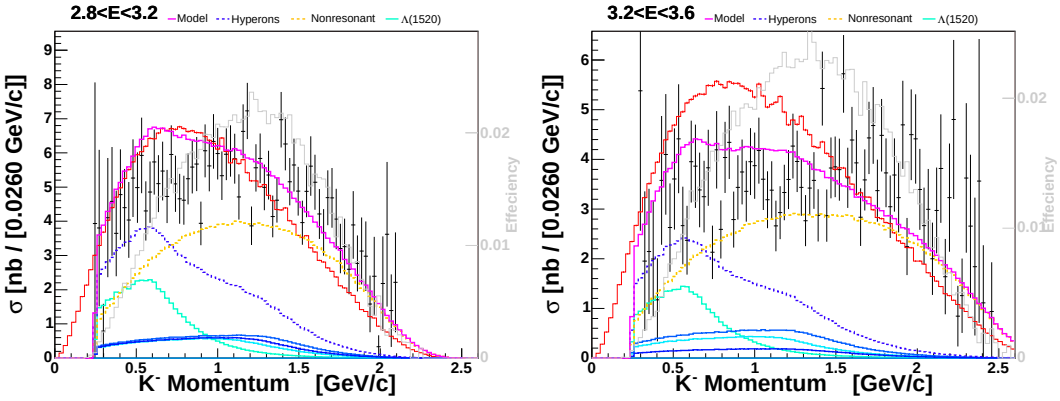

FIGURE 5.22. Lab momentum of the K^-, showing the contribution of individual resonances in the "new" model. The total fit is drawn in magenta, the individual hyperon resonances are shades of blue, and the nonresontant $K\bar{K}$ component is orange.

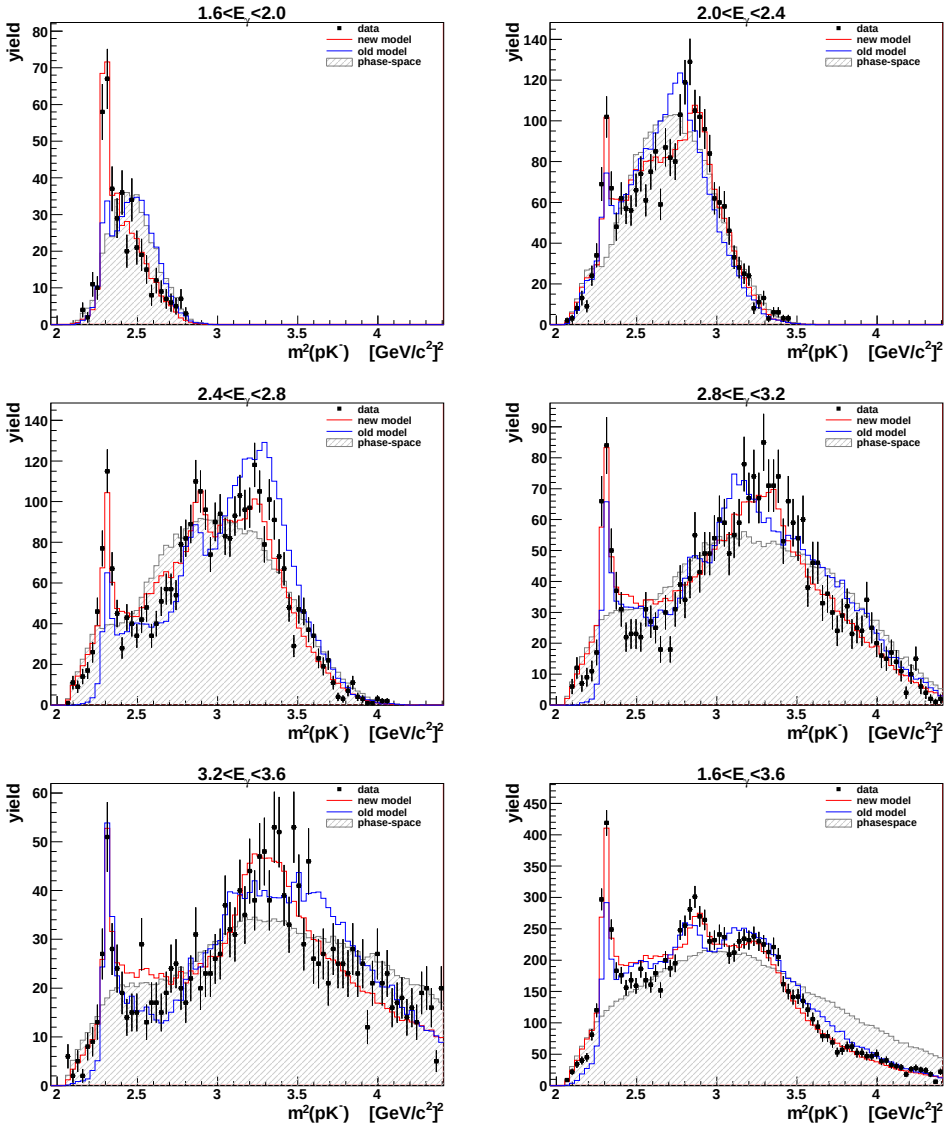

FIGURE 5.23. Invariant mass of the pK^- system. The raw data is represented by the points with error bars. The three models, "new" (red), "old" (blue), and phase-space, are corrected by their respective acceptances from Section 5.3.

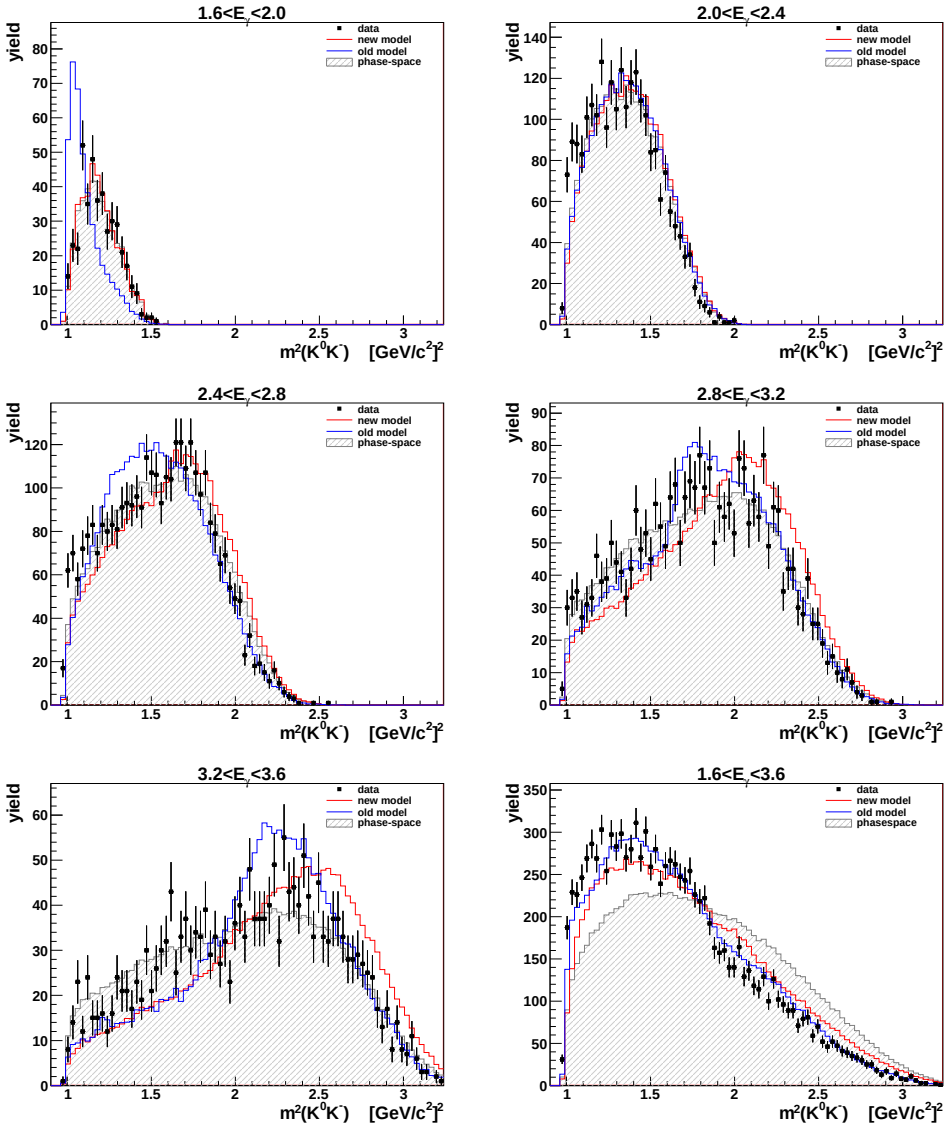

FIGURE 5.24. Invariant mass of the K^0K^- system. The raw data is represented by the points with error bars. The three models, "new" (red), "old" (blue), and phase-space, are corrected by their respective acceptances.

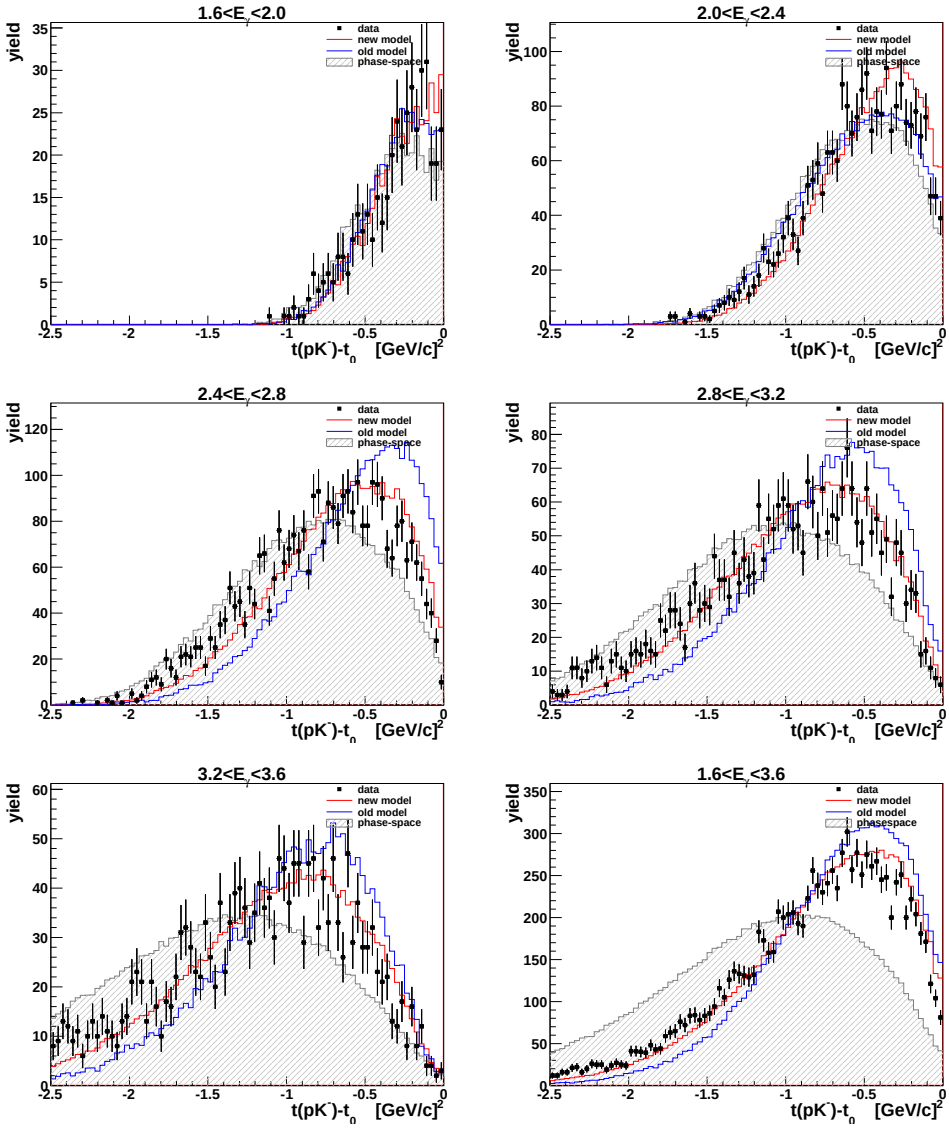

FIGURE 5.25. Momentum transfer from the target nucleon to the pK^-. The raw data is represented by the points with error bars. The three models, "new" (red), "old" (blue), and phase-space, are corrected by their respective acceptances.

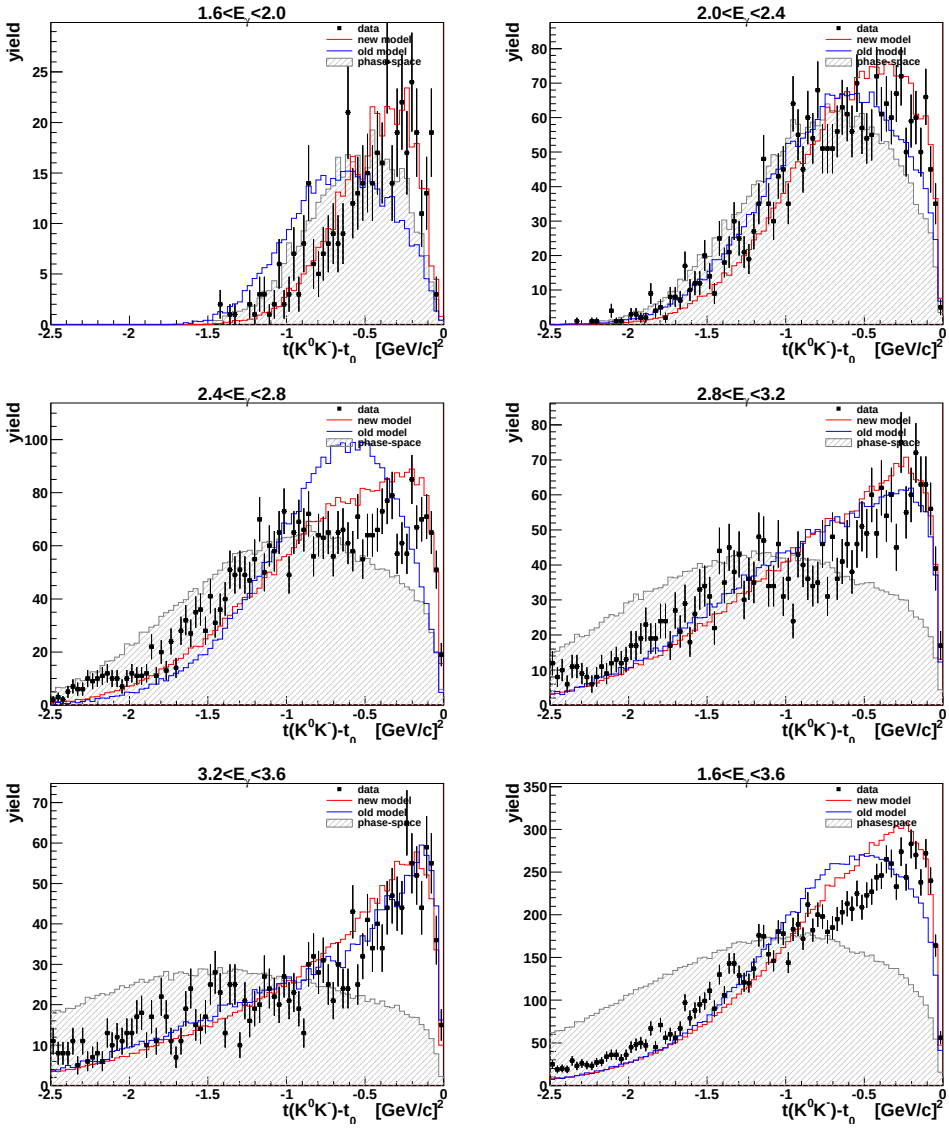

FIGURE 5.26. Momentum transfer from the beam photon to the K^0K^-. The raw data is represented by the points with error bars. The three models, "new" (red), "old" (blue), and phase-space, are corrected by their respective acceptances.

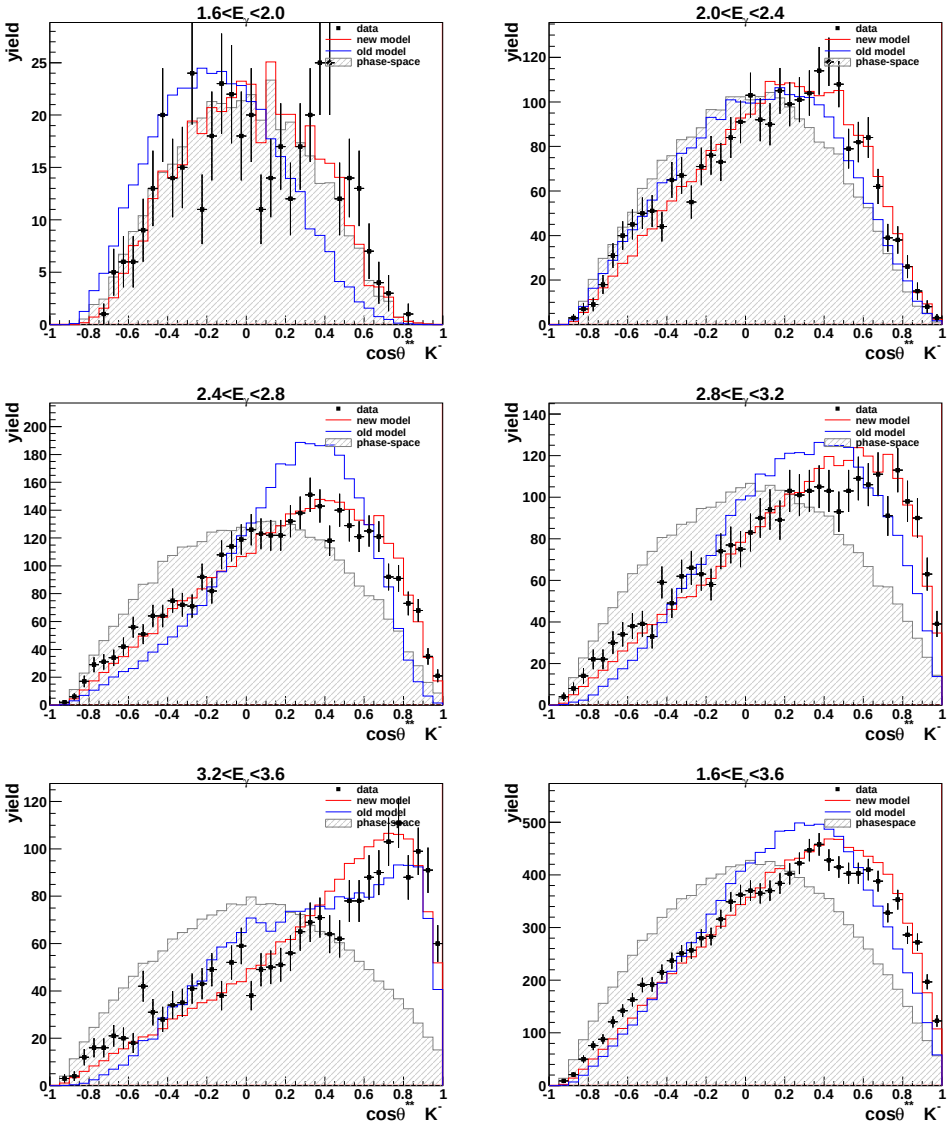

FIGURE 5.27. Polar angle of the K^- in the pK^- helicity frame. The raw data is represented by the points with error bars. The three models, "new" (red), "old" (blue), and phase-space, are corrected by their respective acceptances.

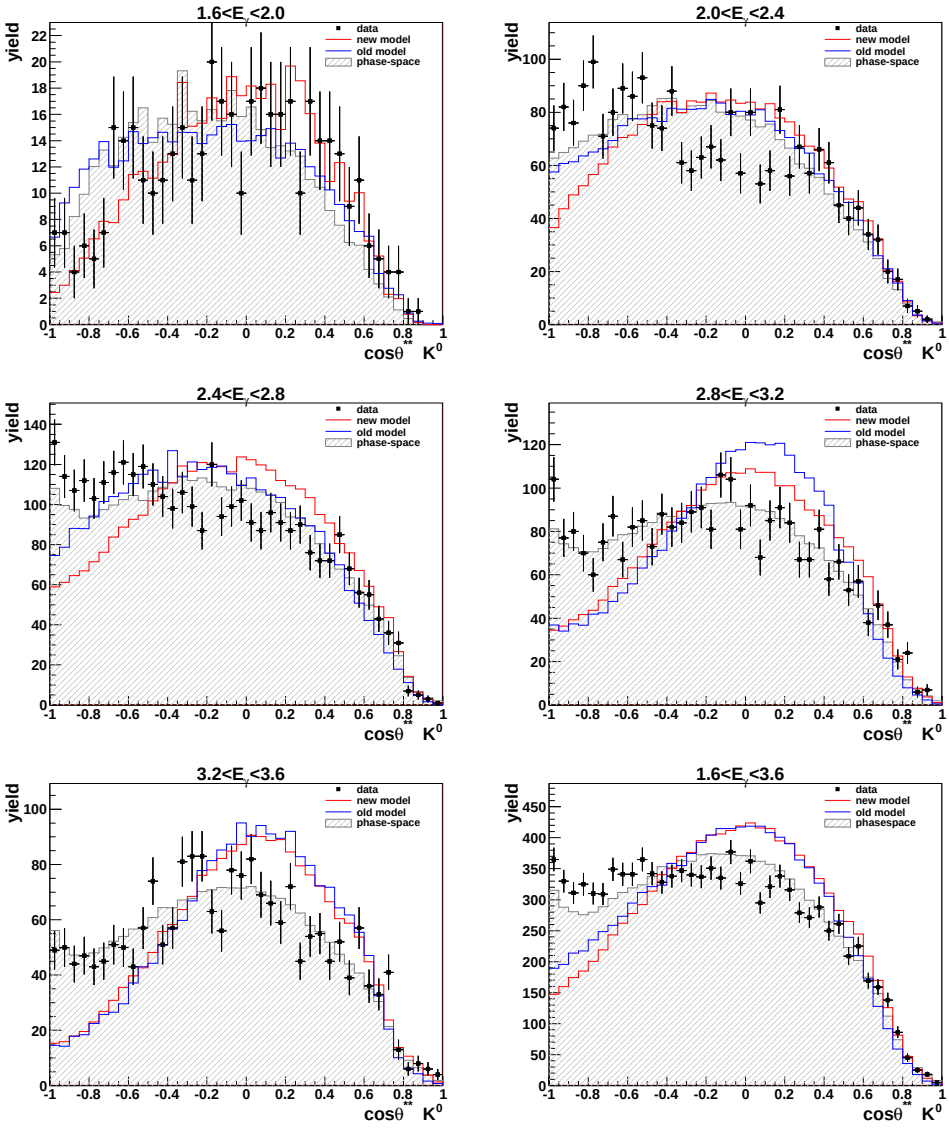

FIGURE 5.28. Polar angle of the K^0 in the K^0K^- helicity frame. The raw data is represented by the points with error bars. The three models, "new" (red), "old" (blue), and phase-space, are corrected by their respective acceptances.

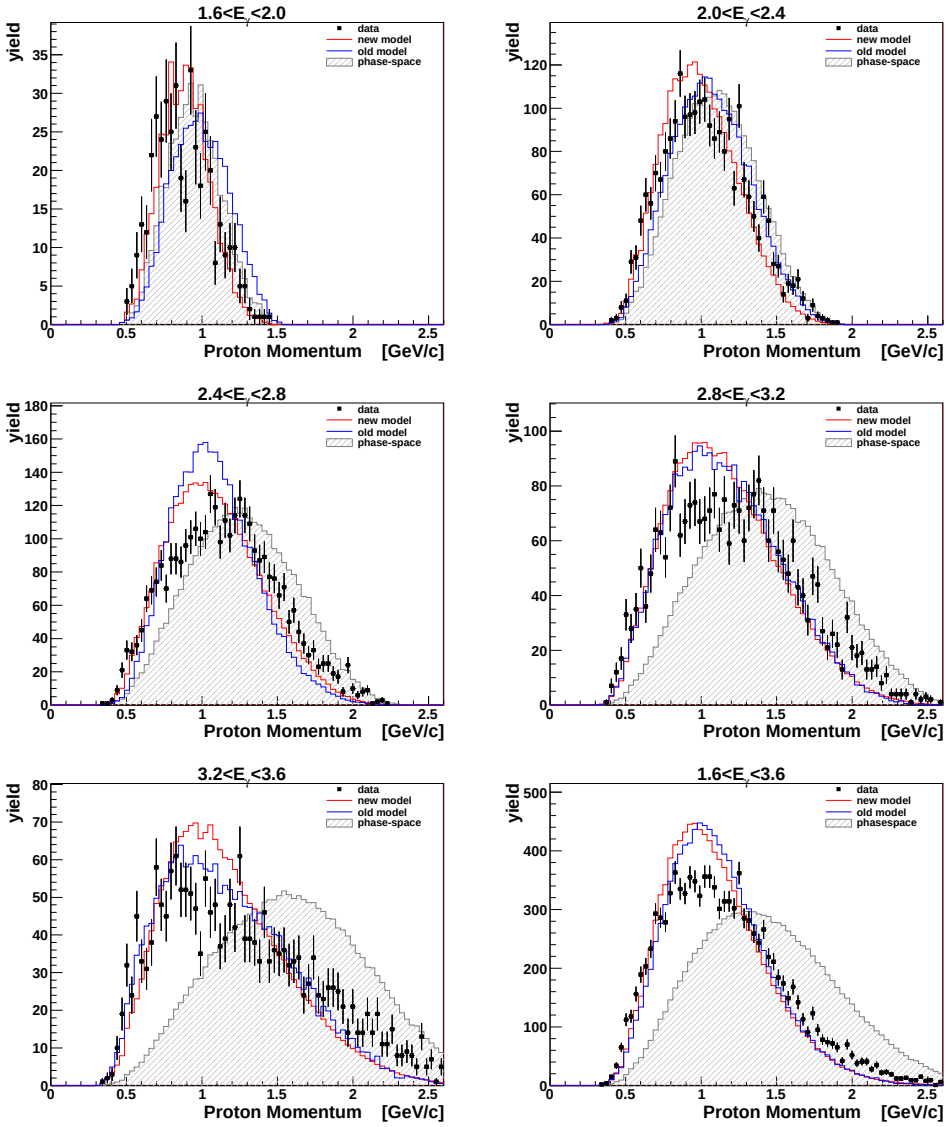

FIGURE 5.29. Lab momentum of the detected proton. The raw data is represented by the points with error bars. The three models, "new" (red), "old" (blue), and phase-space (shaded), are corrected by their respective acceptances.

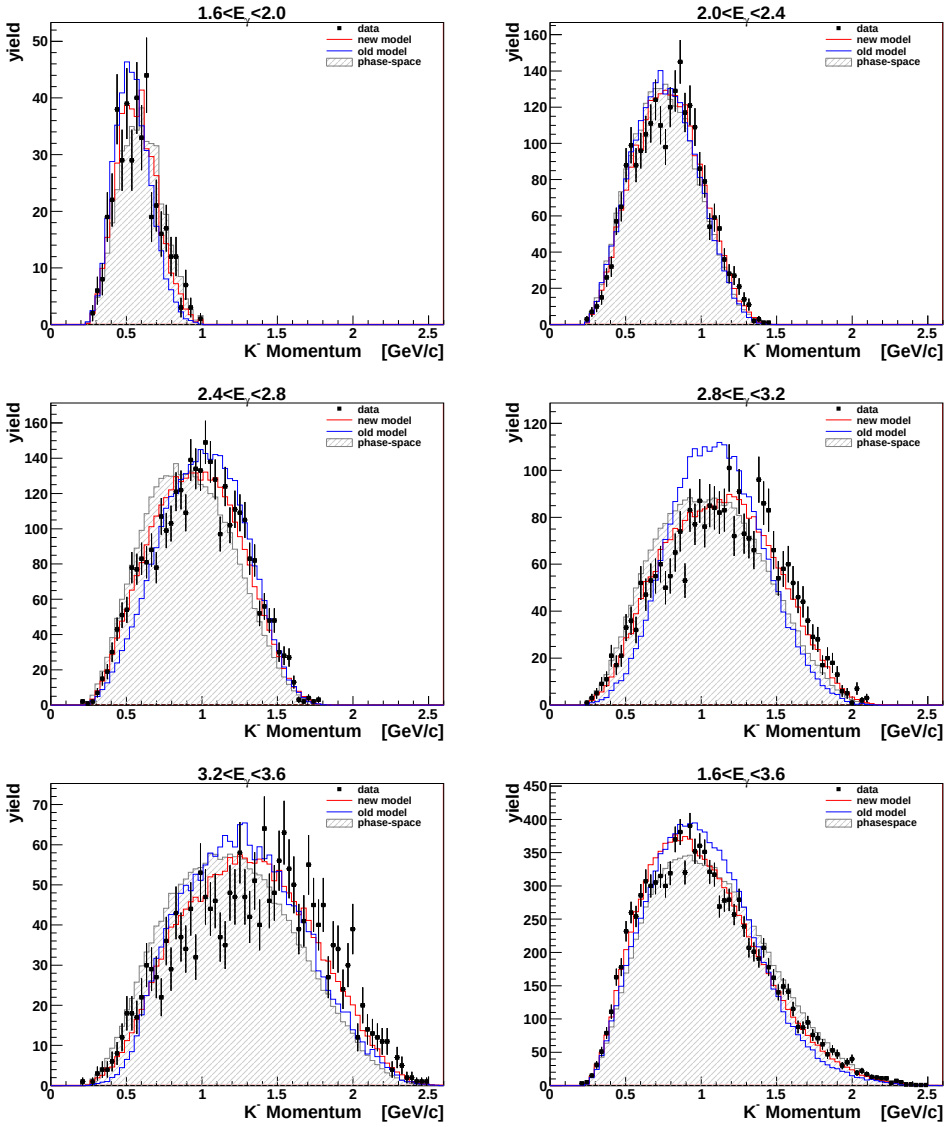

FIGURE 5.30. Lab momentum of the K^- for four photon energy bins. The raw data is represented by the points with error bars. The three models, "new" (red), "old" (blue), and phase-space (shaded), are corrected by their respective acceptances.

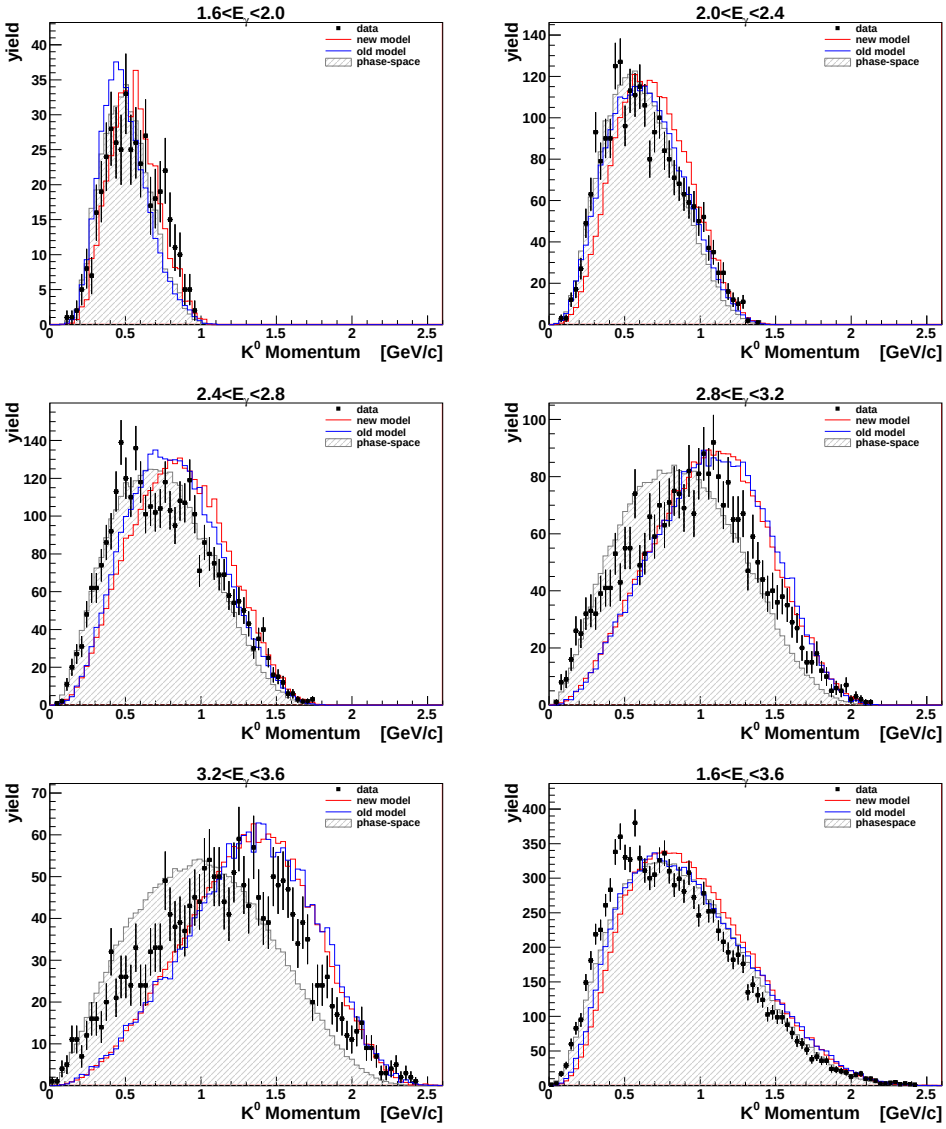

FIGURE 5.31. Lab momentum of the K^0 for four photon energy bins. The raw data is represented by the points with error bars. The three models, "new" (red), "old" (blue), and phase-space (shaded), are corrected by their respective acceptances.

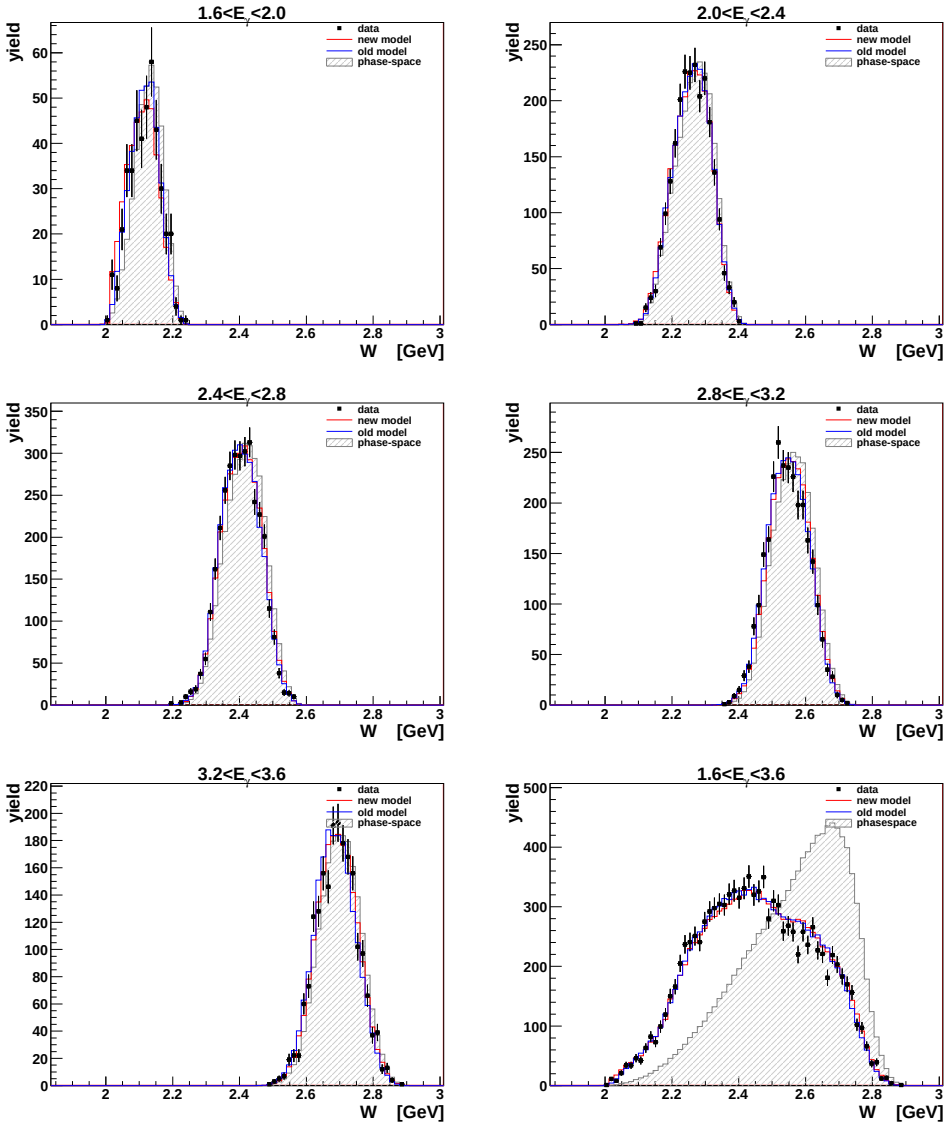

FIGURE 5.32. Total energy $w = \sqrt{s}$ of the reaction $\gamma n \to pK^0K^-$. The raw data is represented by the points with error bars. The three models, "new" (red), "old" (blue), and phase-space (shaded), are corrected by their respective acceptances.

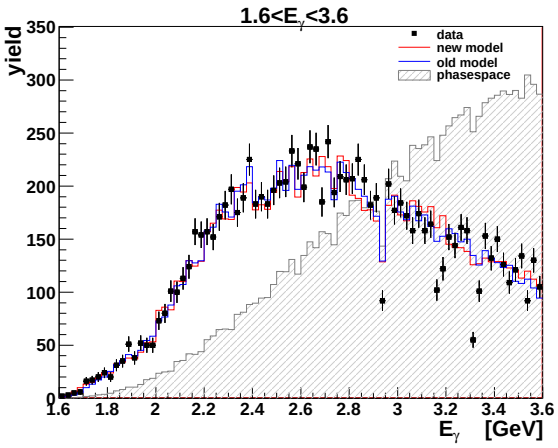

FIGURE 5.33. Lab photon energy. The raw data is represented by the points with error bars. The three models, "new" (red), "old" (blue), and phase-space (shaded), are corrected by their respective acceptances.

5.5.2. "New"-Acceptance-Corrected. The models' raw amplitude functions can be directly compared to efficiency-corrected data. The raw yield histograms from Section 5.5.1 are divided by the efficiency as calculated from the "new" model, shown in Section 5.3. The following figures show this efficiency-corrected data superimposed with the "new" and "old" model amplitudes.

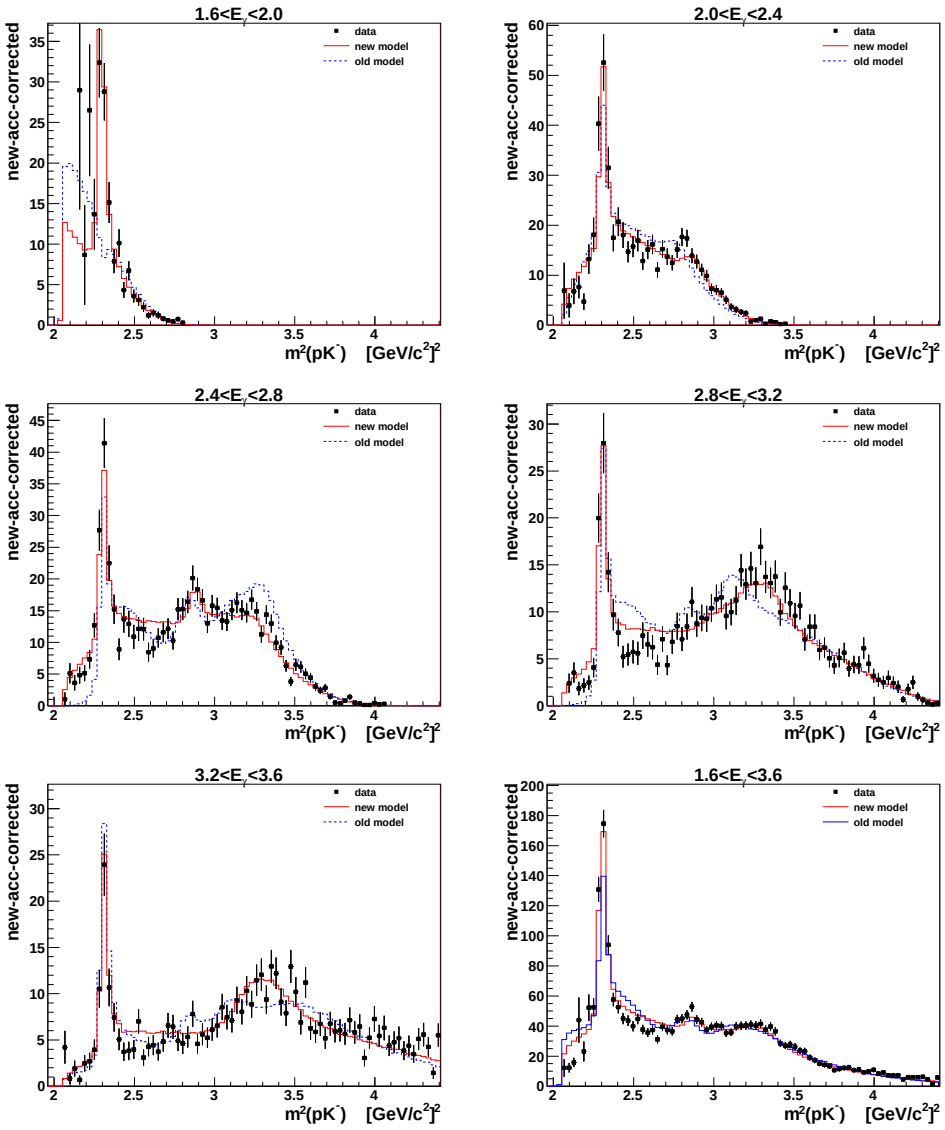

FIGURE 5.34. Acceptance-corrected invariant mass of the pK^- system. The data is corrected by the "new" model acceptance. The "new" (red) and "old" (blue) models are superimposed.

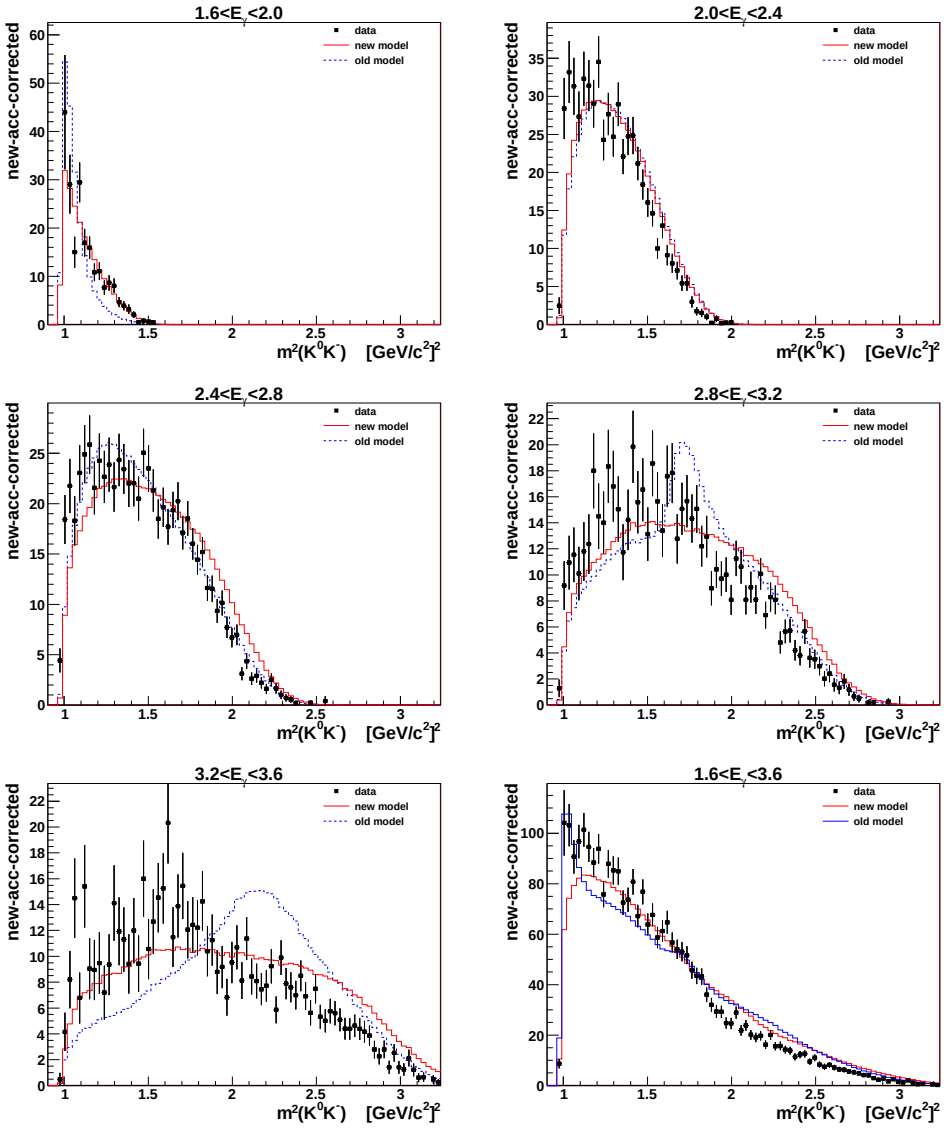

FIGURE 5.35. Acceptance-corrected invariant mass of the K^0K^- system. The data is corrected by the "new" model acceptance. The "new" (red) and "old" (blue) models are superimposed.

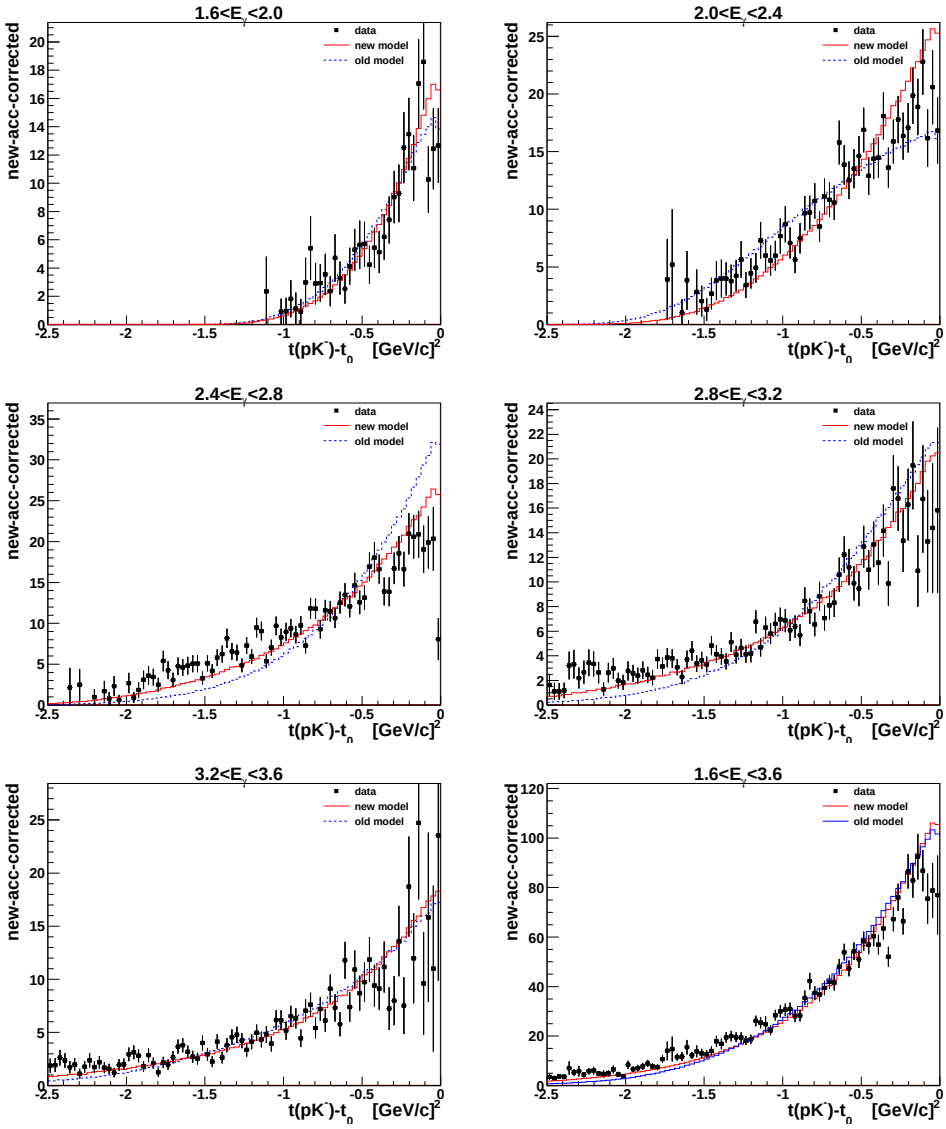

FIGURE 5.36. Acceptance-corrected momentum transfer from the target nucleon to the pK^- system. The data is corrected by the "new" model acceptance. The "new" (red) and "old" (blue) models are superimposed.

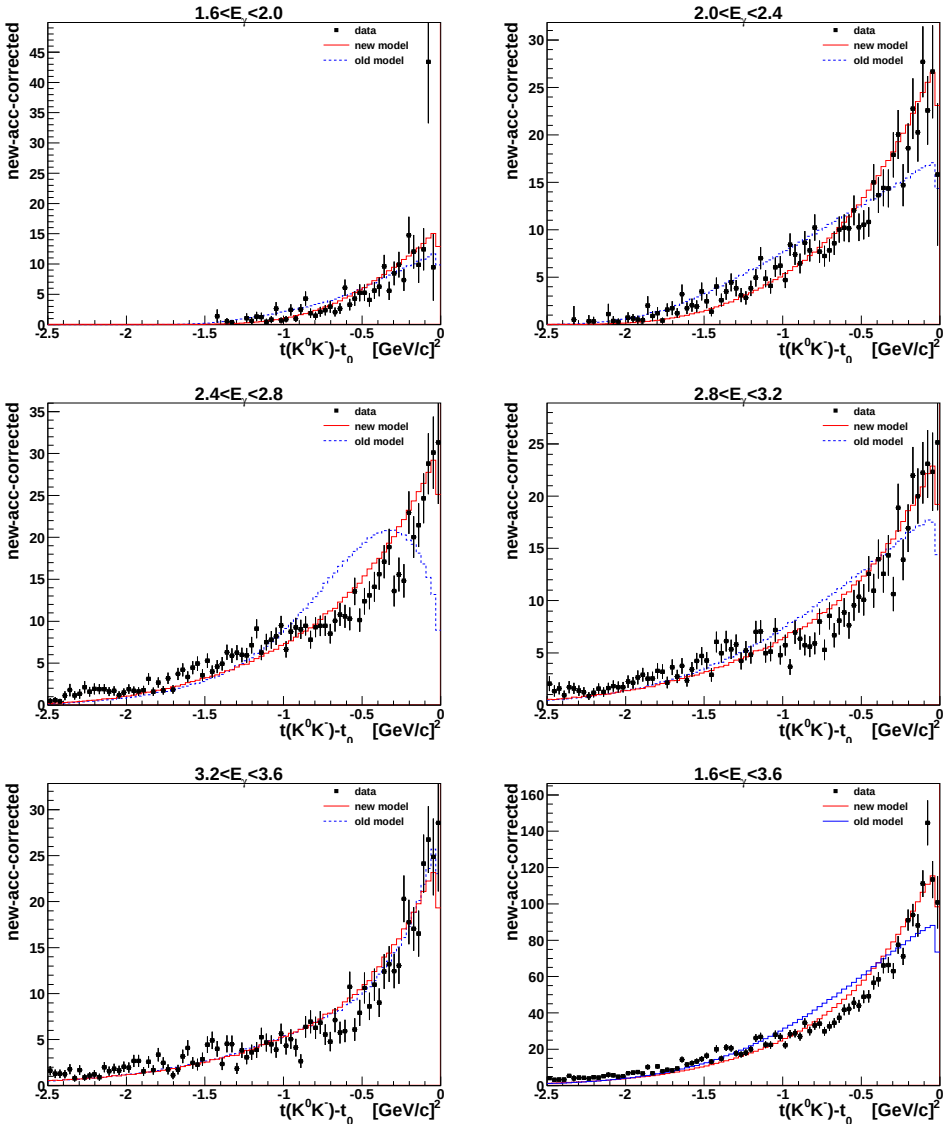

FIGURE 5.37. Acceptance-corrected momentum transfer from the beam photon to the K^0K^- system. The data is corrected by the "new" model acceptance. The "new" (red) and "old" (blue) models are superimposed.

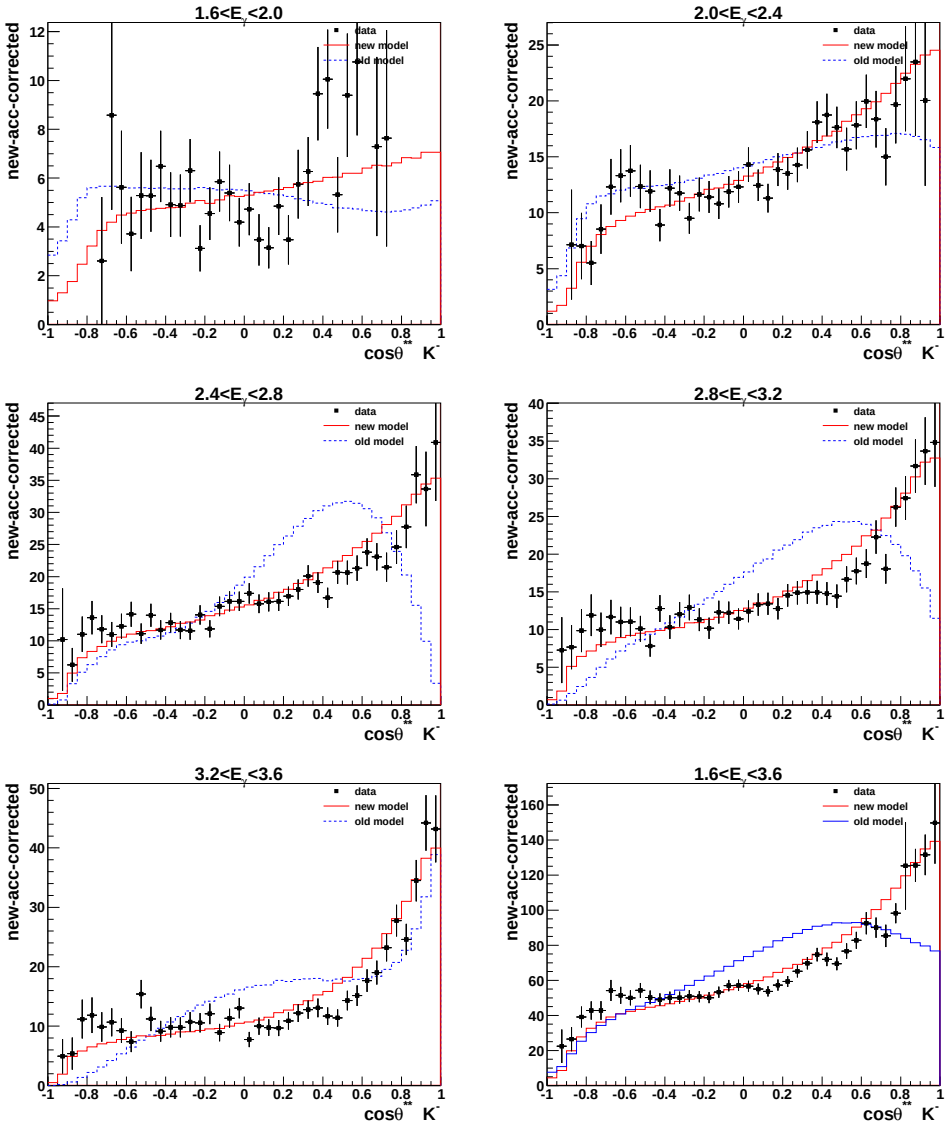

FIGURE 5.38. Acceptance-corrected polar angle of the K^- in the pK^- helicity frame. The data is corrected by the "new" model acceptance. The "new" (red) and "old" (blue) models are superimposed.

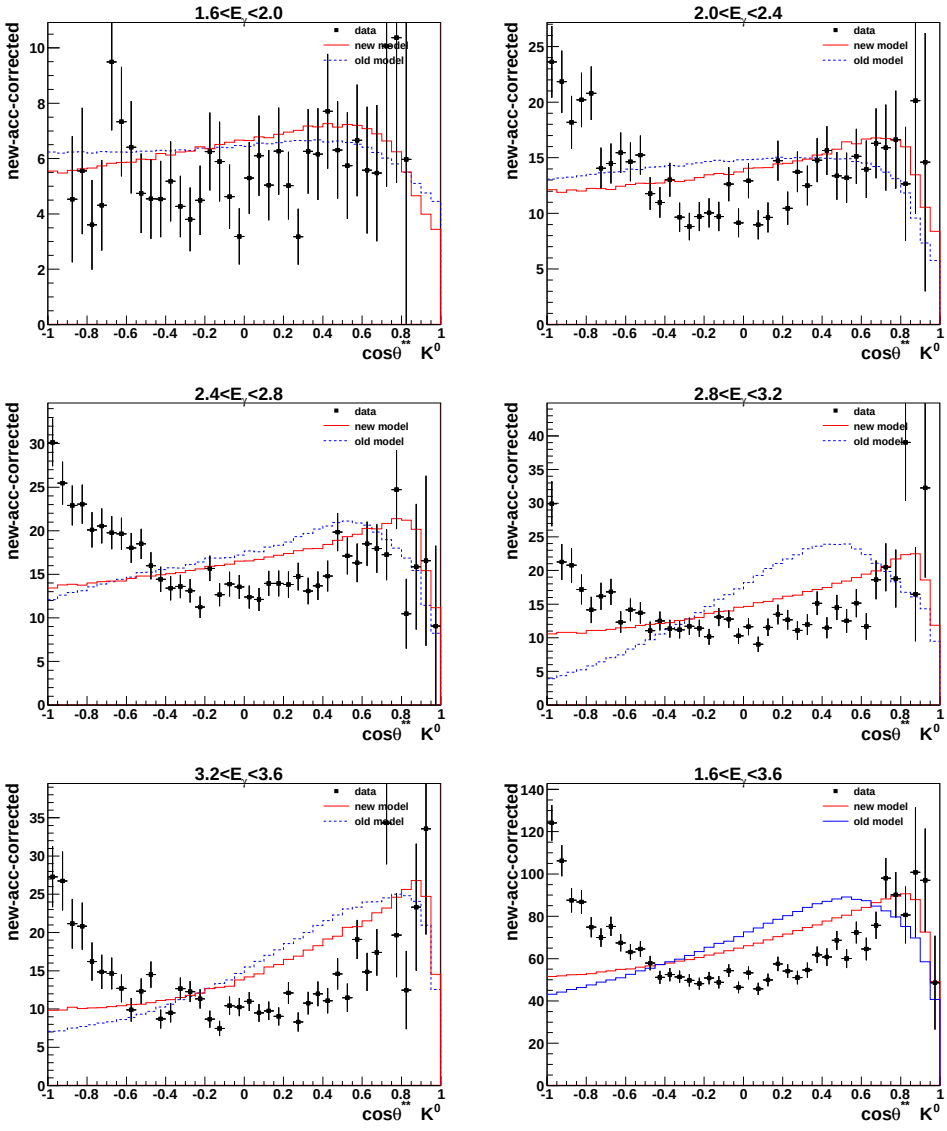

FIGURE 5.39. Acceptance-corrected polar angle of the K^0 in the K^0K^- helicity frame. The data is corrected by the "new" model acceptance. The "new" (red) and "old" (blue) models are superimposed.

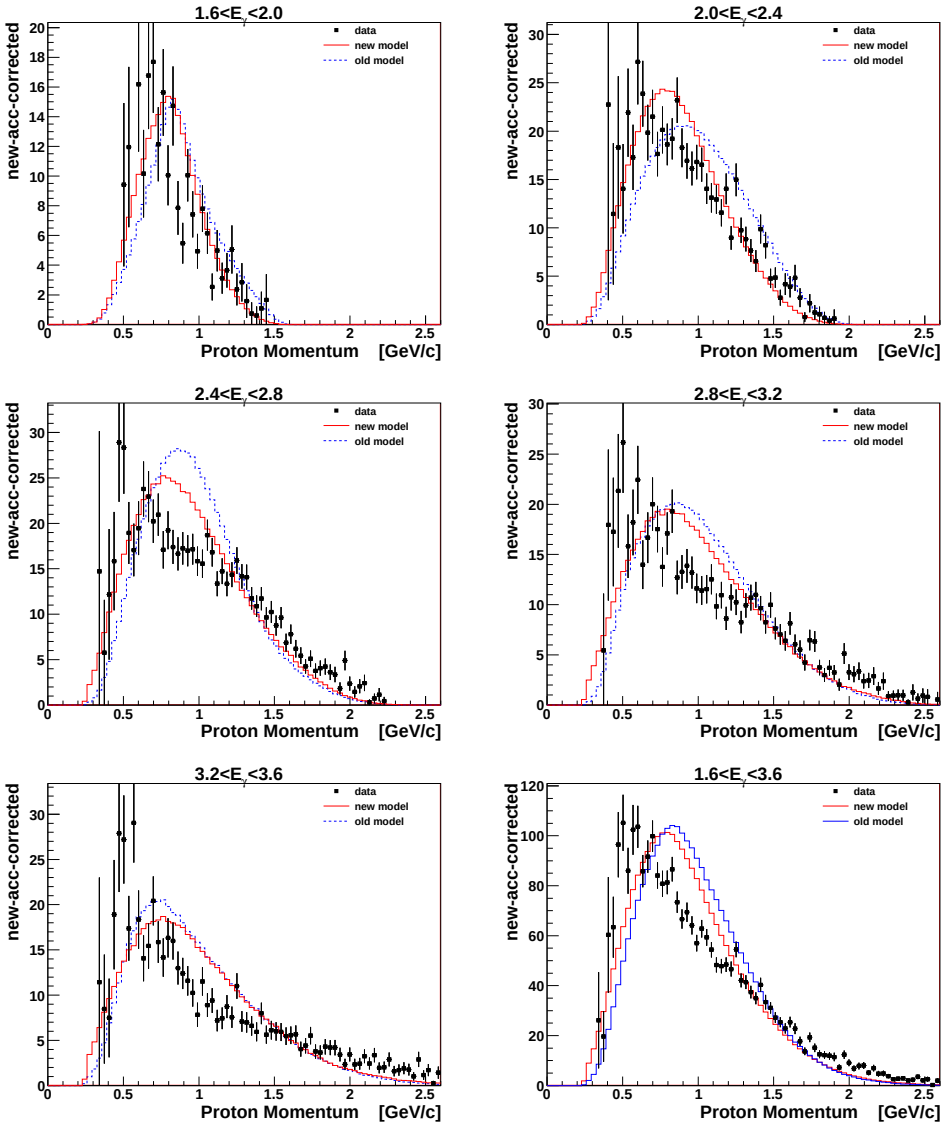

FIGURE 5.40. Acceptance-corrected lab momentum of the detected proton. The data is corrected by the "new" model acceptance. The "new" (red) and "old" (blue) models are superimposed.

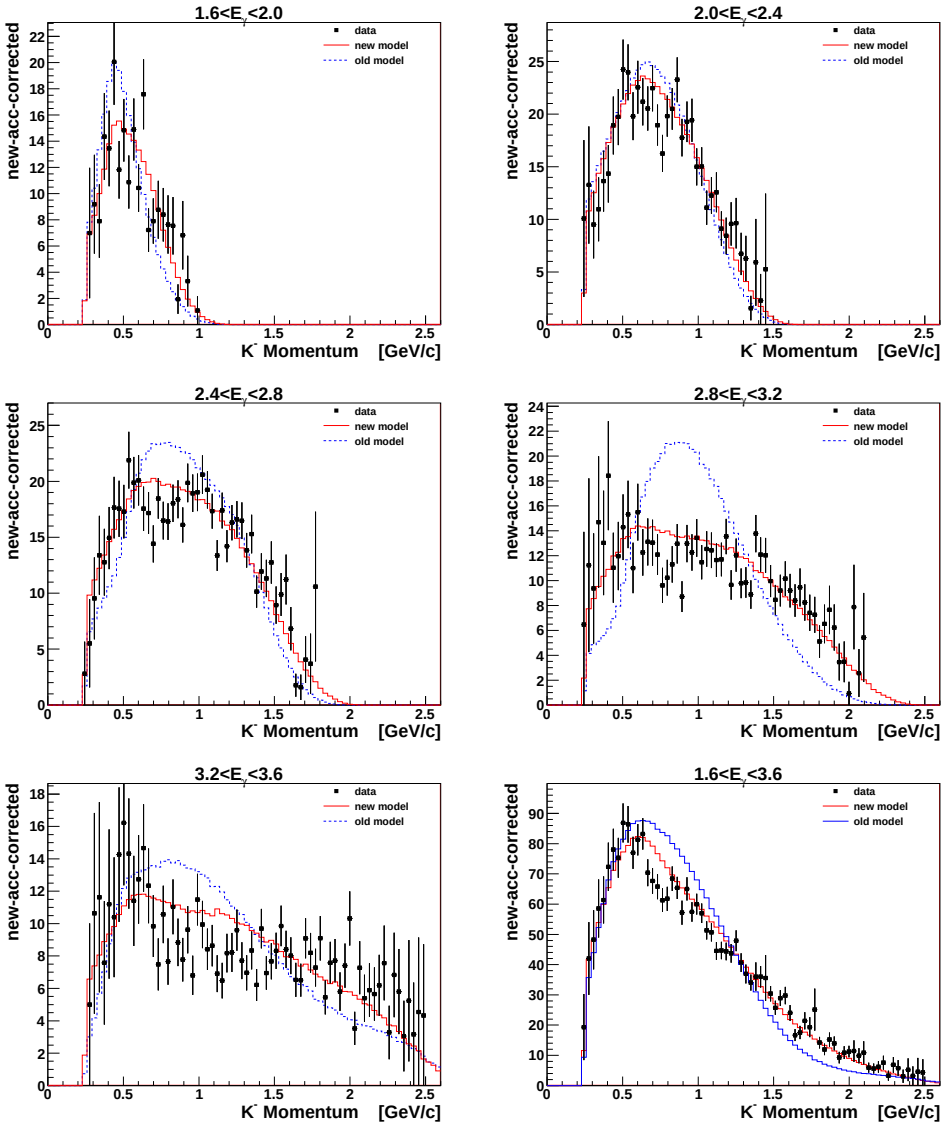

FIGURE 5.41. Acceptance-corrected lab momentum of the K^-. The data is corrected by the "new" model acceptance. The "new" (red) and "old" (blue) models are superimposed.

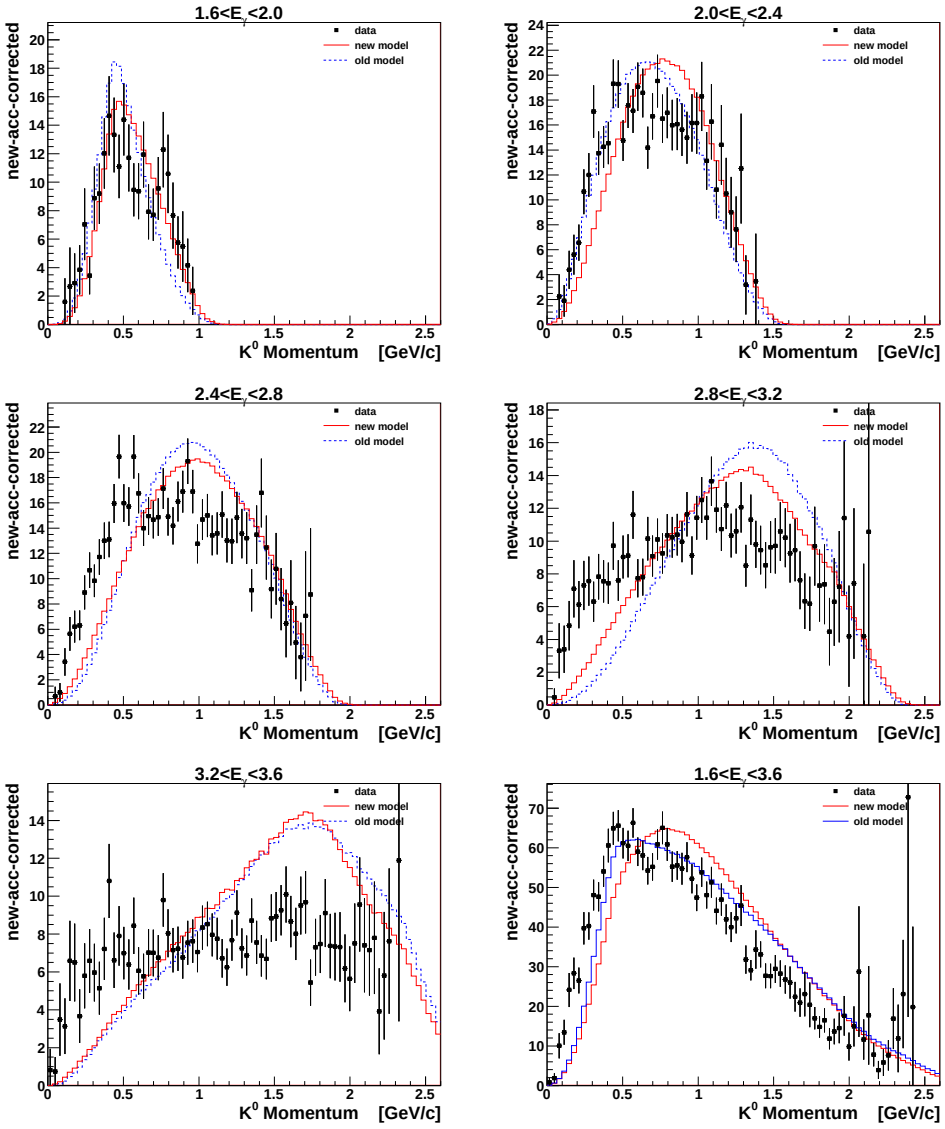

FIGURE 5.42. Acceptance-corrected lab momentum of the K^0. The data is corrected by the "new" model acceptance. The "new" (red) and "old" (blue) models are superimposed.

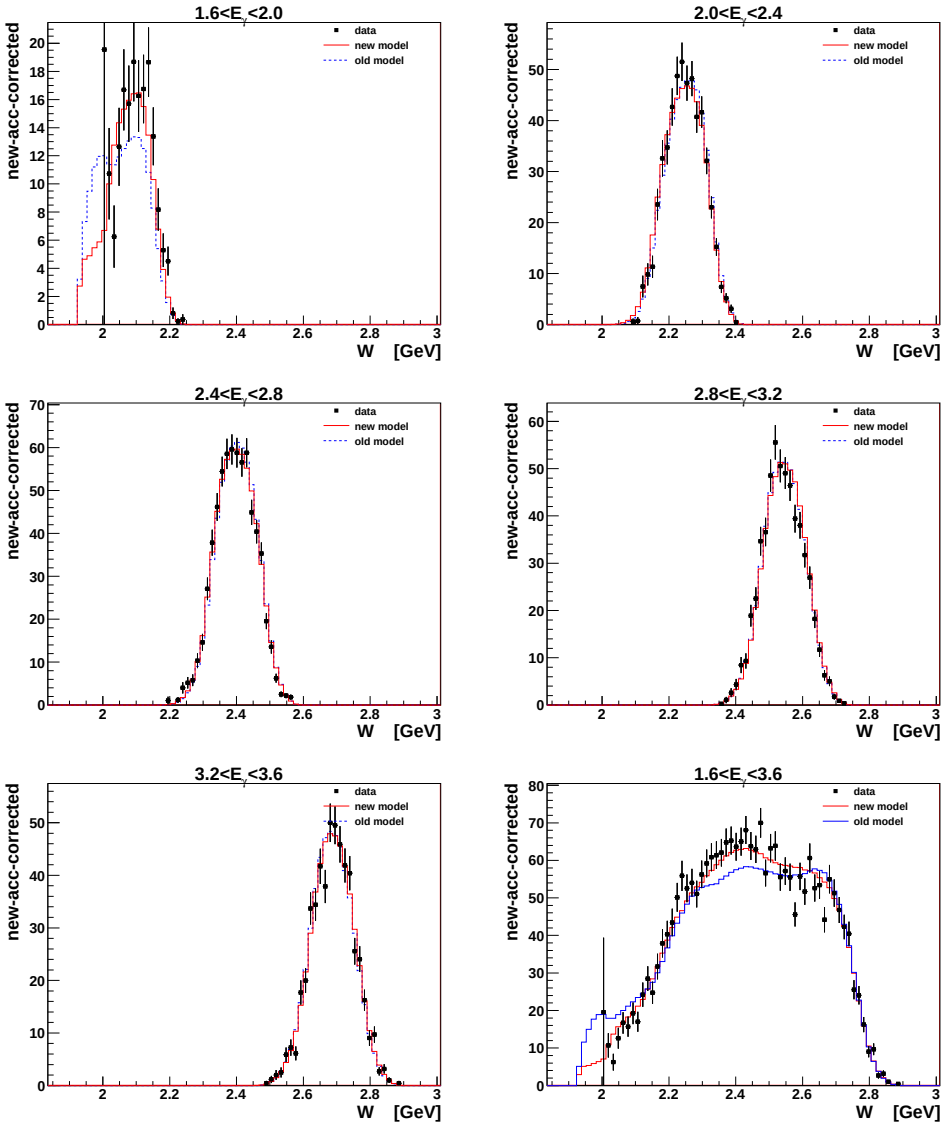

FIGURE 5.43. Acceptance-corrected total energy $w = \sqrt{s}$ of the reaction $\gamma n \to pK^0K^-$. The data is corrected by the "new" model acceptance. The "new" (red) and "old" (blue) models are superimposed.

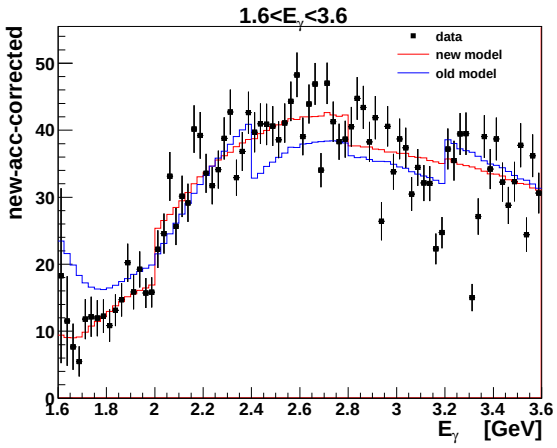

FIGURE 5.44. Acceptance-corrected lab photon energy. The data is corrected by the "new" model acceptance. The "new" (red) and "old" (blue) models are superimposed.

5.5.3. "Phase-space"-Acceptance-Corrected. This is identiacal to Section 5.5.2, except the data is now corrected by the "phase-space" efficiency, as shown in Section 5.3, and the phase-space distribution is superimposed.

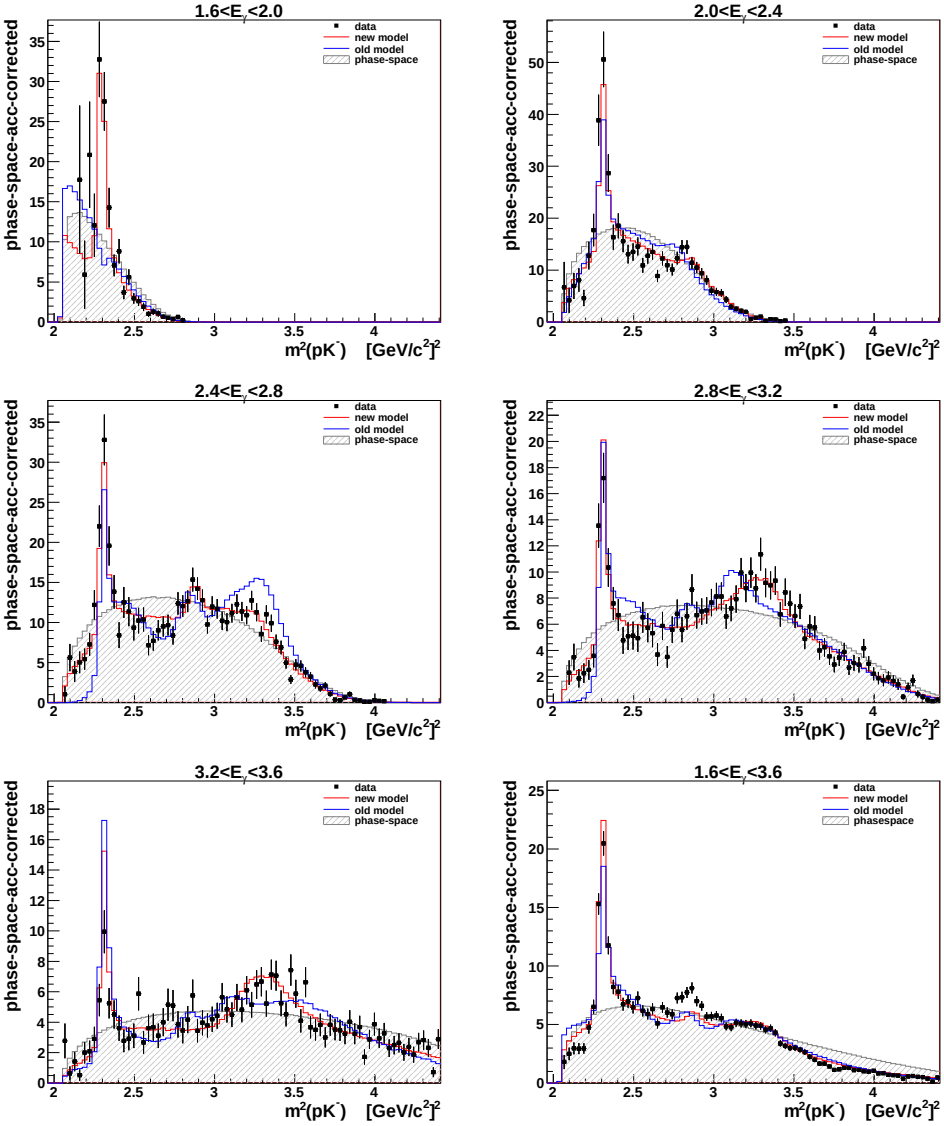

FIGURE 5.45. Invariant mass of the pK^- system. The data is corrected by the 3-body phase-space model's acceptance. The phase-space (green), "new" (red), and "old" (blue) models are superimposed.

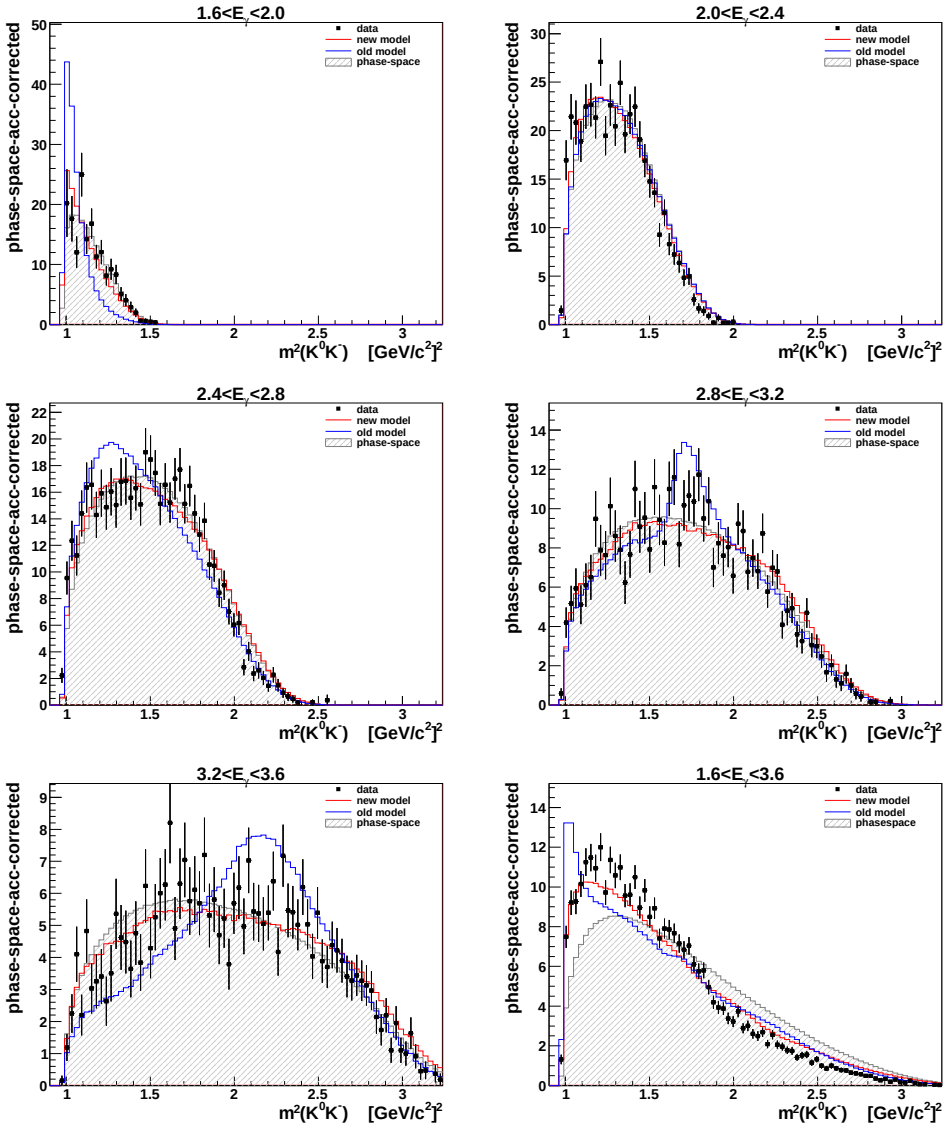

FIGURE 5.46. Invariant mass of the K^0K^- system. The data is corrected by the 3-body phase-space model's acceptance. The phase-space (green), "new" (red), and "old" (blue) models are superimposed.

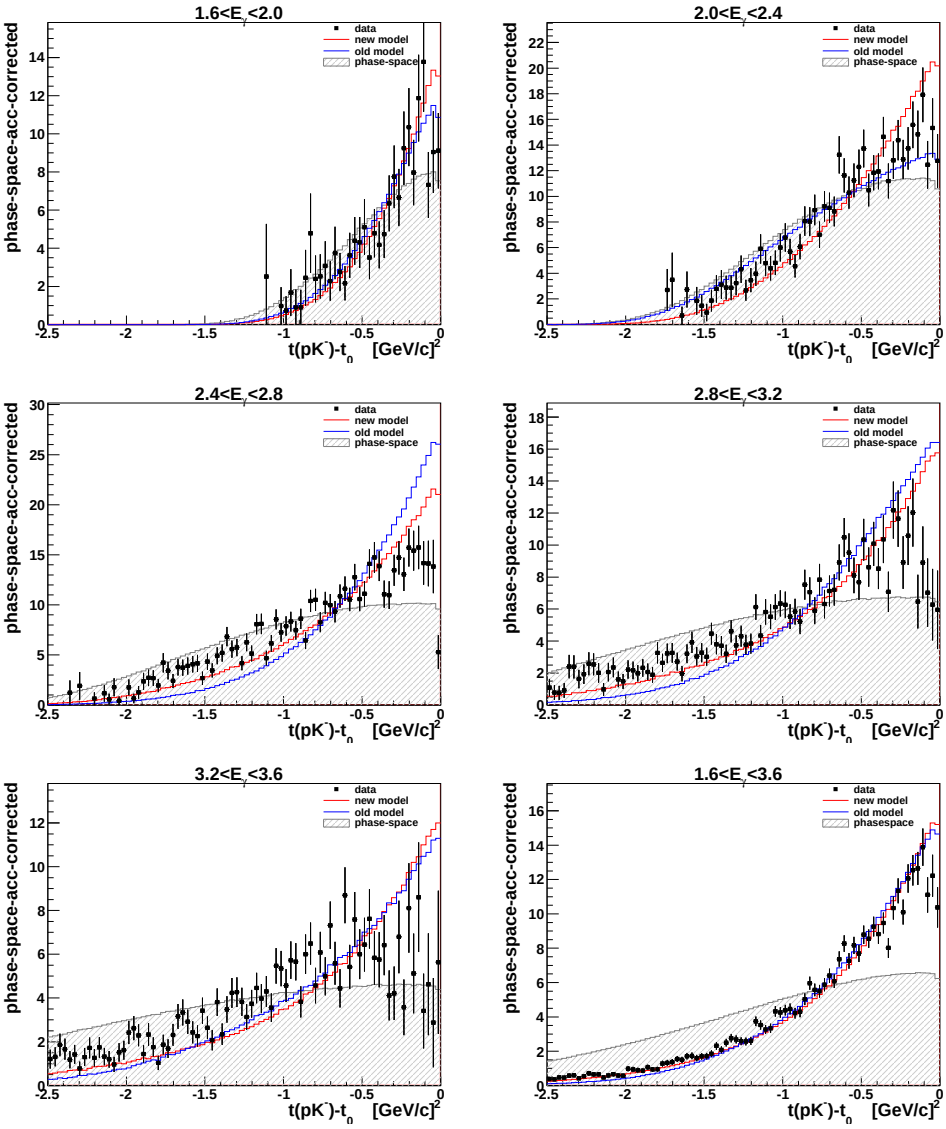

FIGURE 5.47. Momentum transfer from the target nucleon to the pK^- system. The data is corrected by the 3-body phase-space model's acceptance. The phase-space (green), "new" (red), and "old" (blue) models are superimposed.

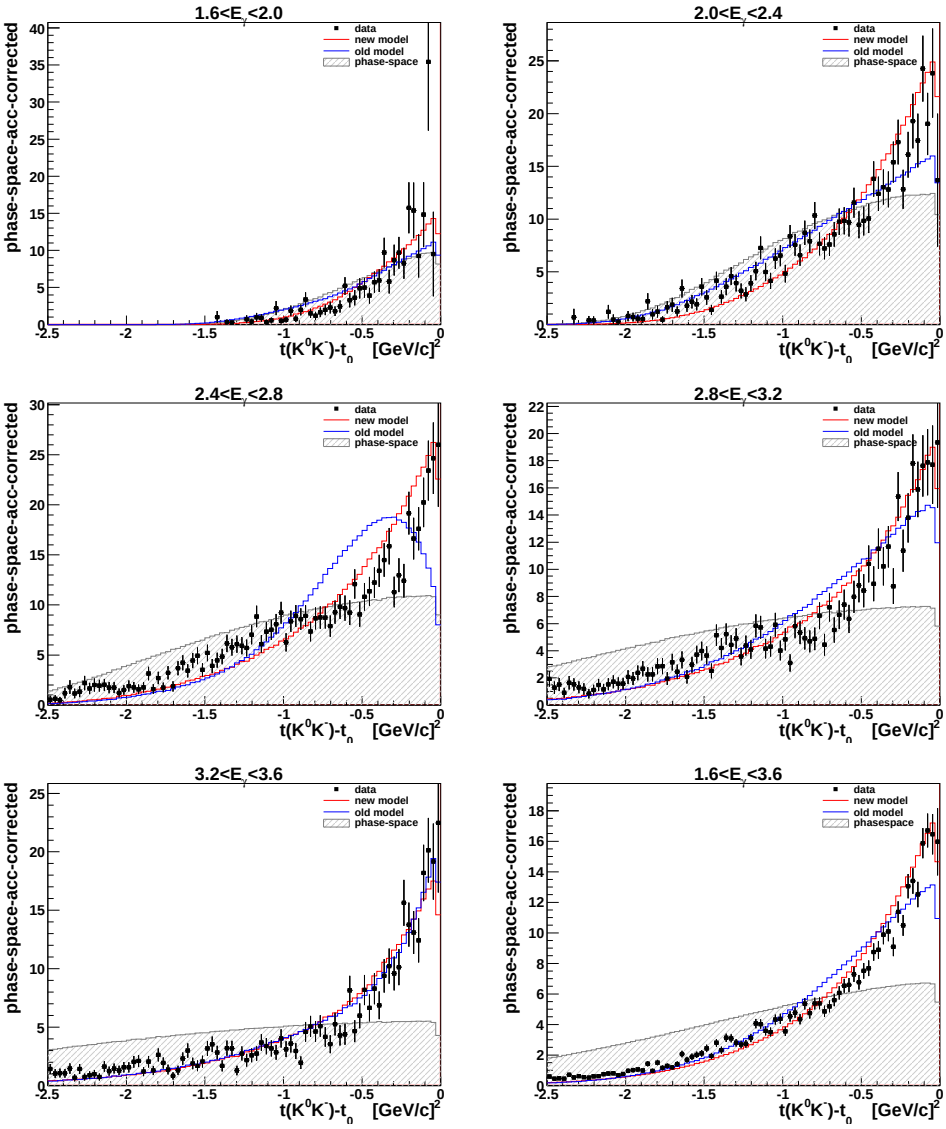

FIGURE 5.48. Momentum transfer from the beam photon to the K^0K^- system. The data is corrected by the 3-body phase-space model's acceptance. The phase-space (green), "new" (red), and "old" (blue) models are superimposed.

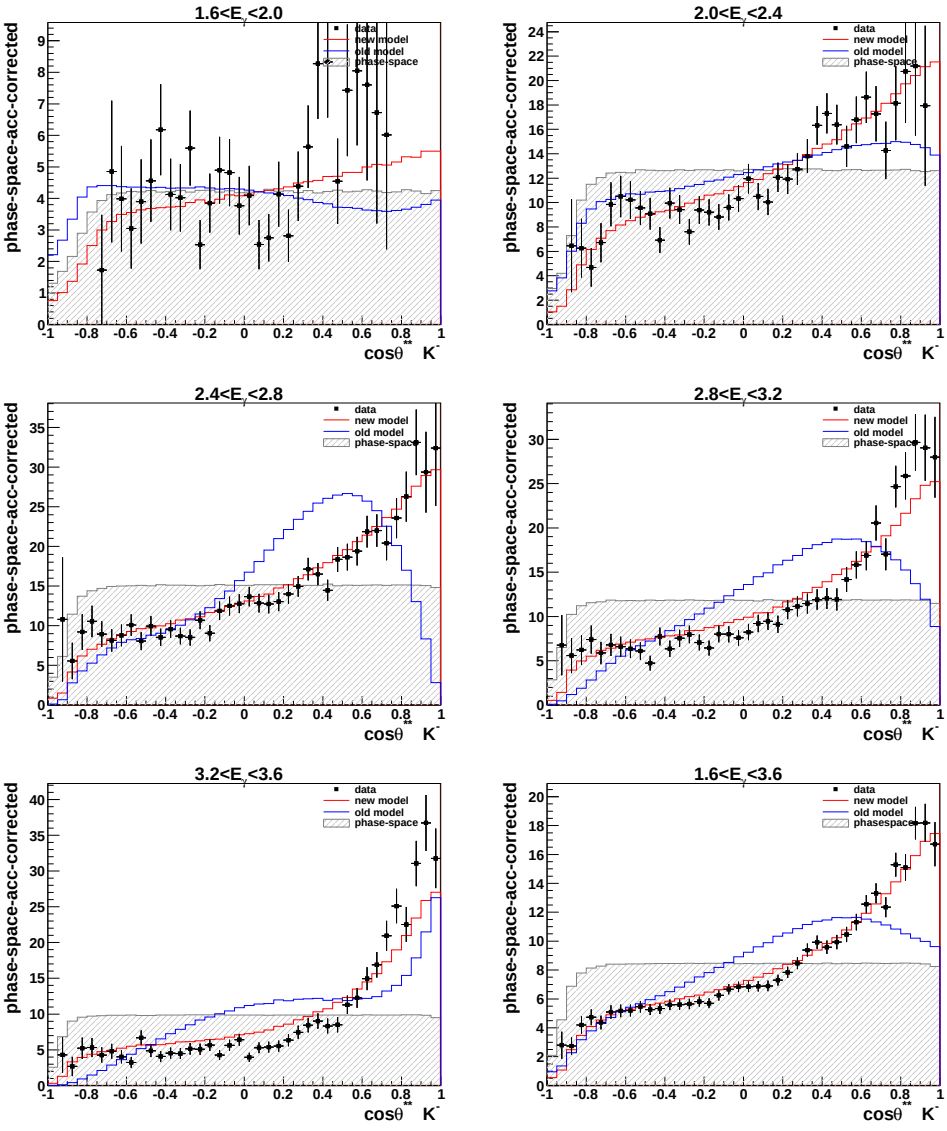

FIGURE 5.49. Polar angle of the K^- in the pK^- helicity frame. The data is corrected by the 3-body phase-space model's acceptance. The phase-space (green), "new" (red), and "old" (blue) models are superimposed.

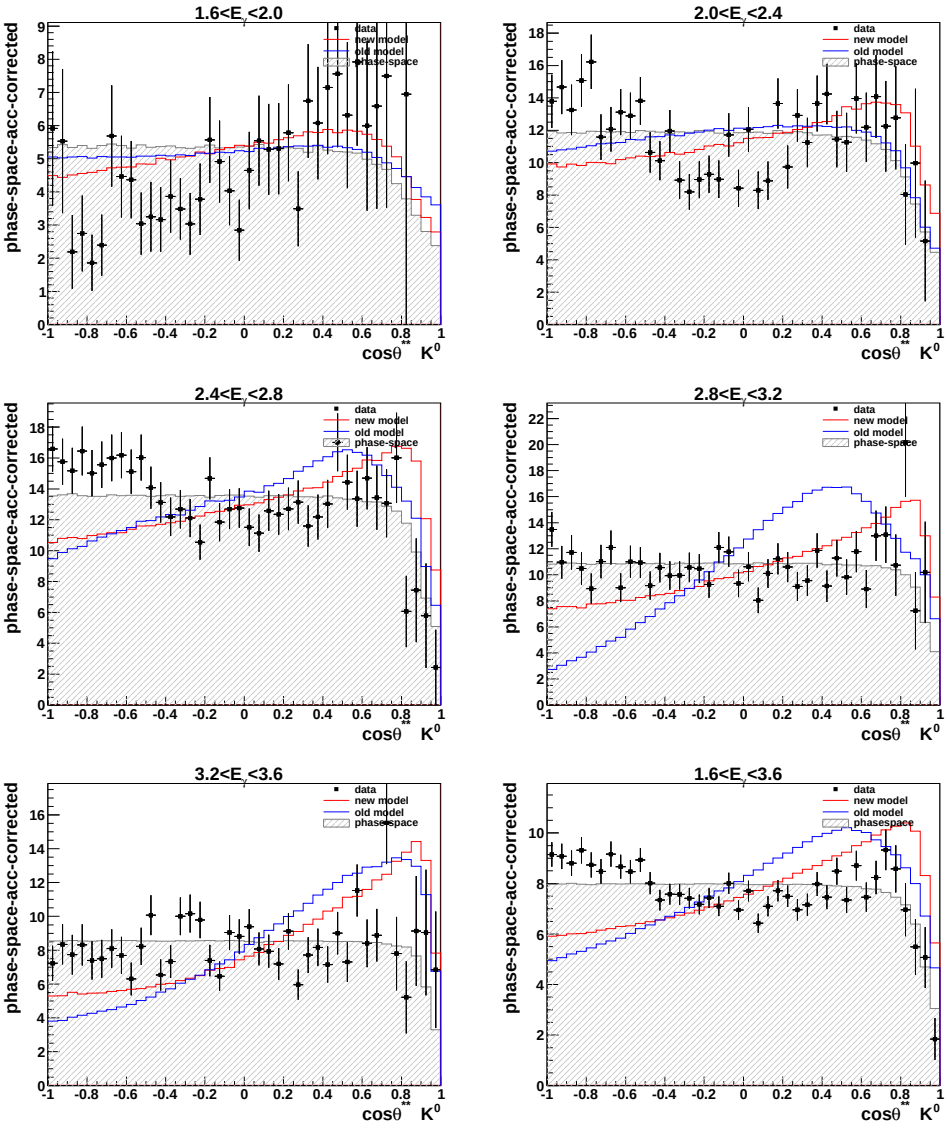

FIGURE 5.50. Polar angle of the K^0 in the K^0K^- helicity frame. The data is corrected by the 3-body phase-space model's acceptance. The phase-space (green), "new" (red), and "old" (blue) models are superimposed.

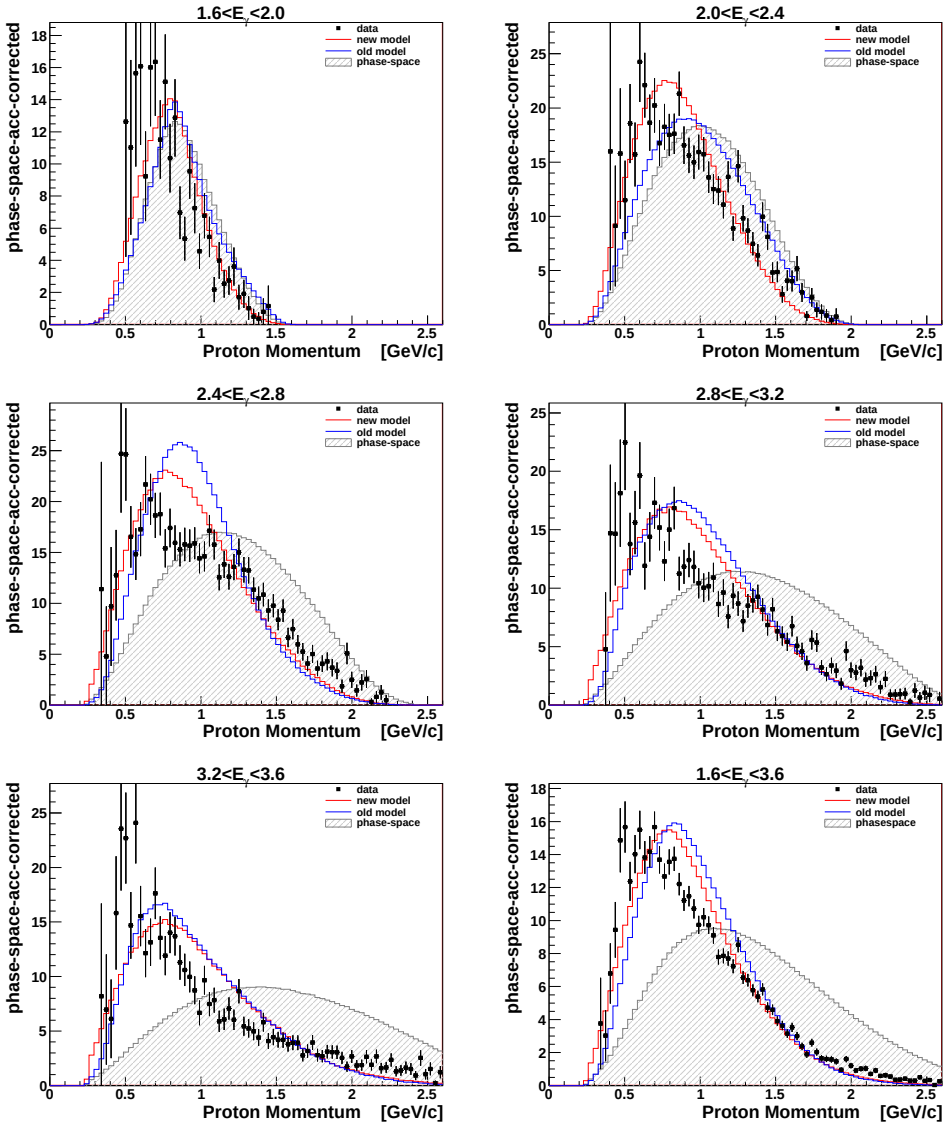

FIGURE 5.51. Lab-frame momentum of the detected proton. The data is corrected by the 3-body phase-space model's acceptance. The phase-space (green), "new" (red), and "old" (blue) models are superimposed.

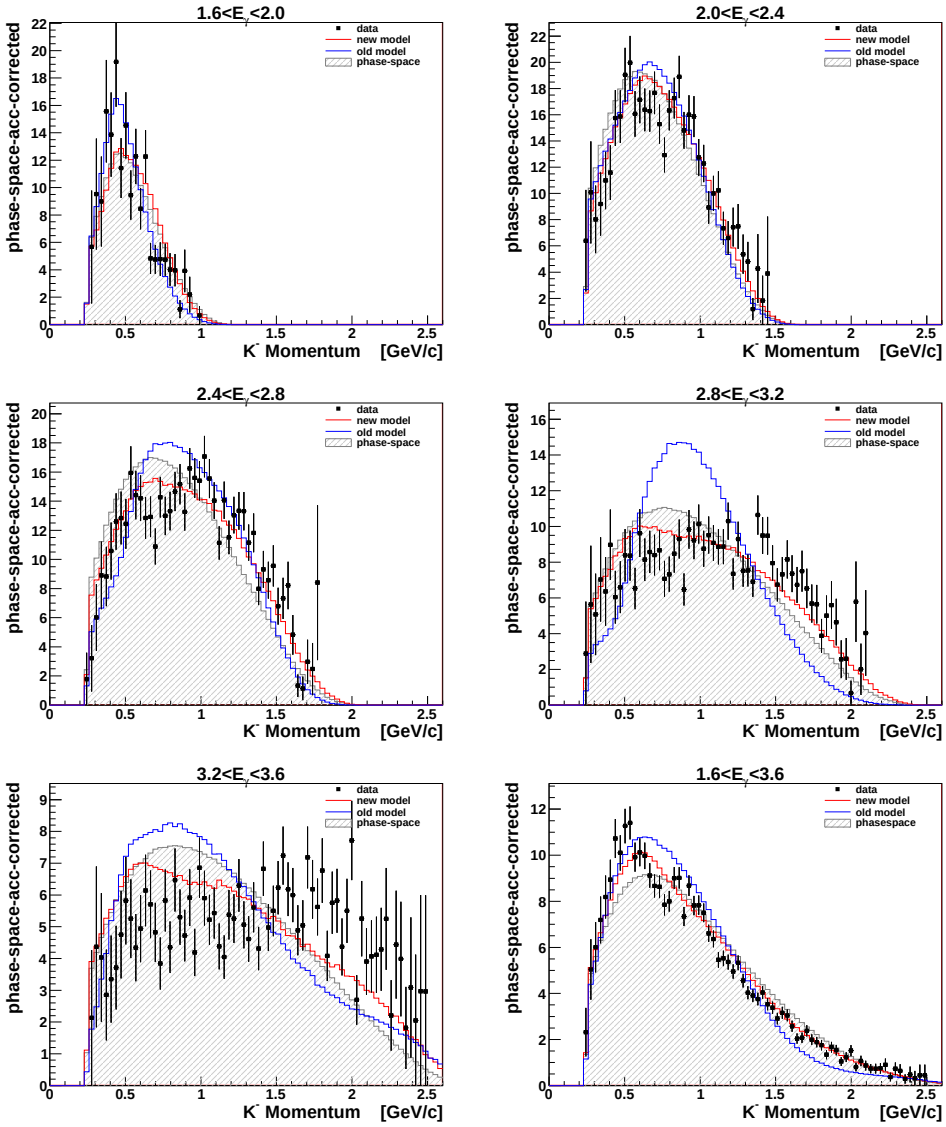

FIGURE 5.52. Lab-frame momentum of the K^-. The data is corrected by the 3-body phase-space model's acceptance. The phase-space (green), "new" (red), and "old" (blue) models are superimposed.

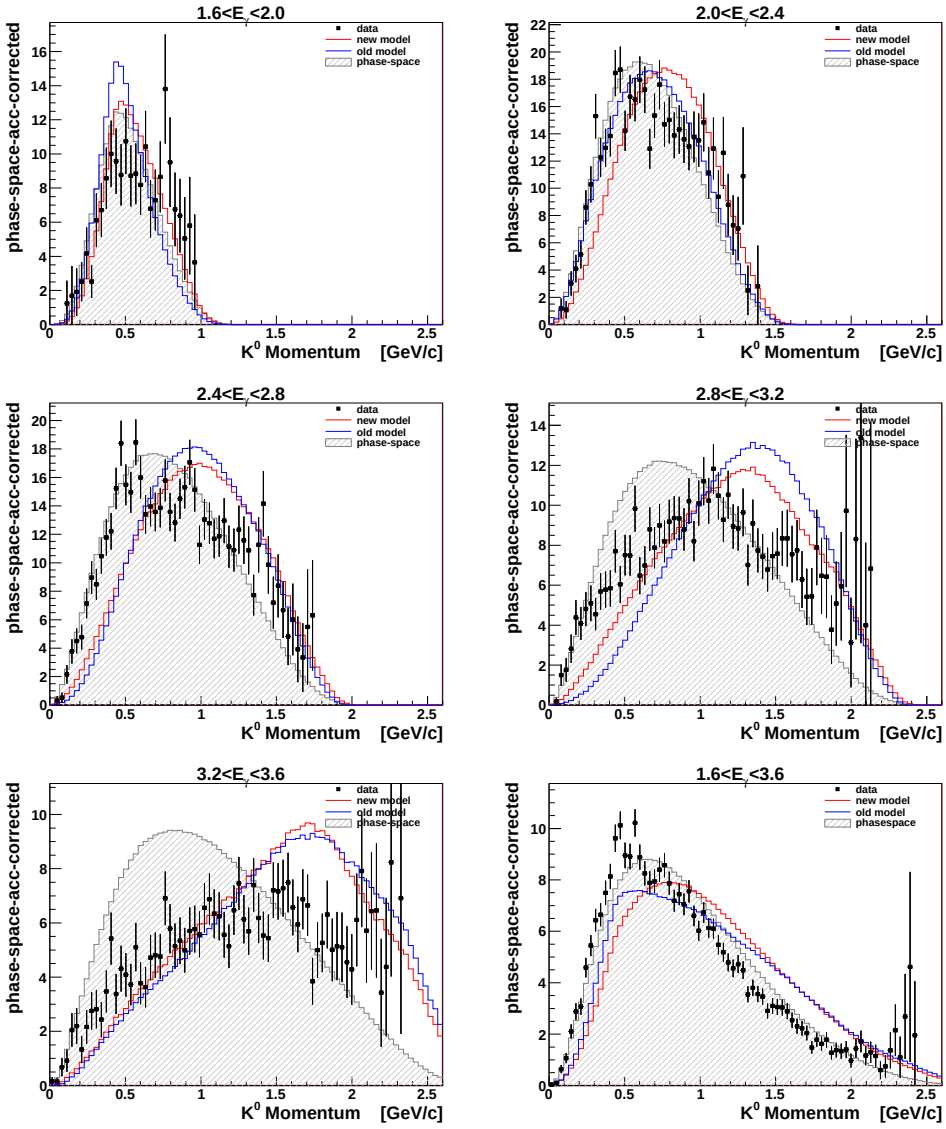

FIGURE 5.53. Lab-frame momentum of the K^0. The data is corrected by the 3-body phase-space model's acceptance. The phase-space (green), "new" (red), and "old" (blue) models are superimposed.

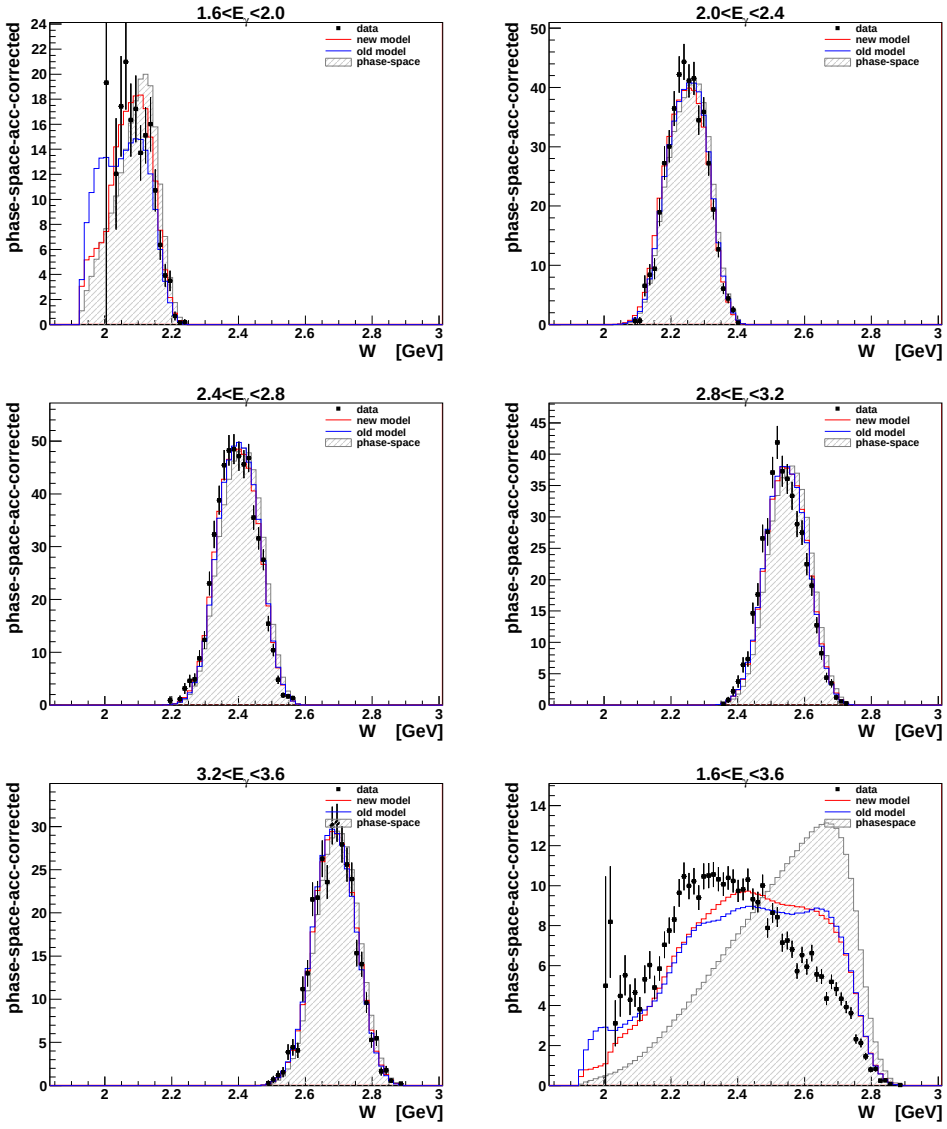

FIGURE 5.54. Total energy $w = \sqrt{s}$ of the reaction $\gamma n \to pK^0K^-$. The phase-space events (shaded histogram) are distinct because thay are not independently weighted in energy bins. The data is corrected by the 3-body phase-space model's acceptance. The phase-space (green), "new" (red), and "old" (blue) models are superimposed.

5.5.4. Invariant Mass of pK^0. The efficiency and three types of data/model comparisons from the previous sections are shown here for the invariant mass of the pK^0 system.

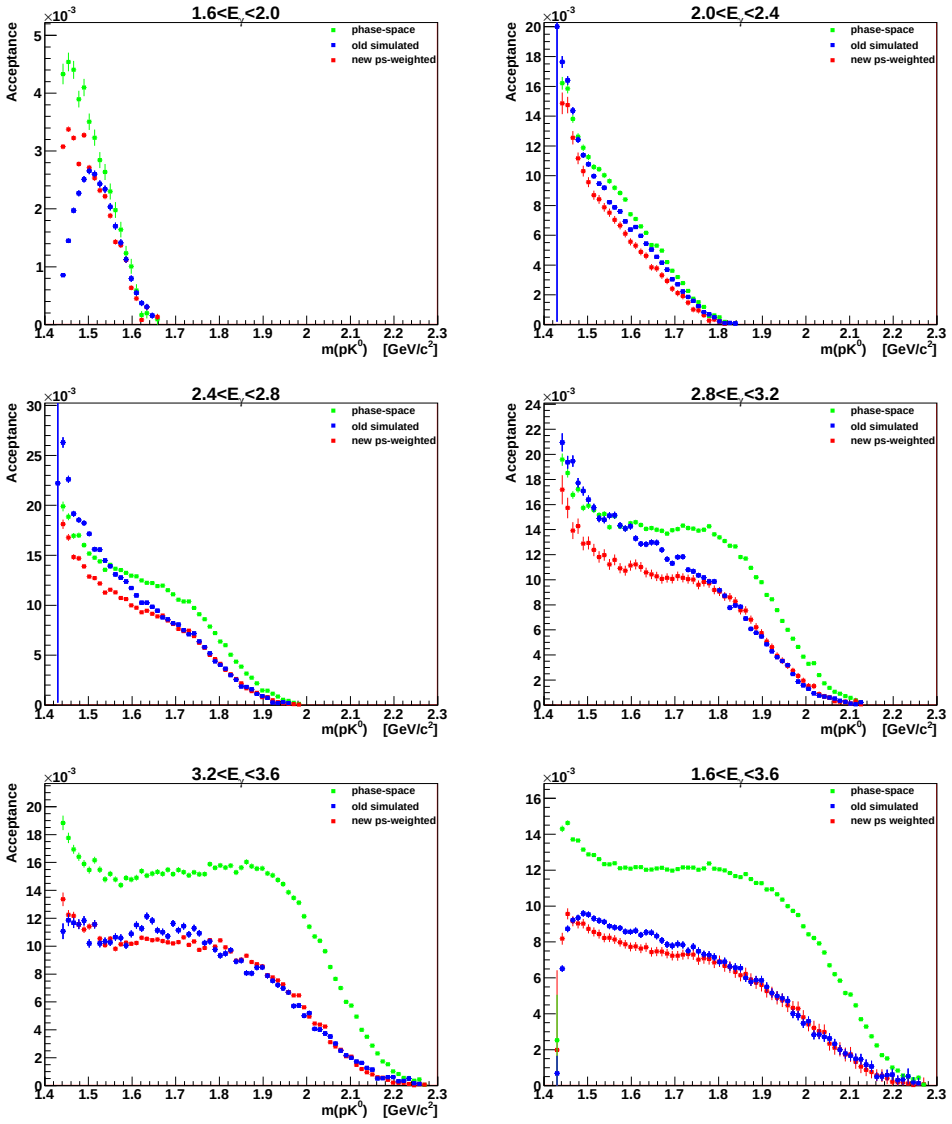

FIGURE 5.55. Efficiency as a function of the invariant mass of the pK^0 system for 3-body phase-space (green), the "old" model (blue), and the "new" model (red).

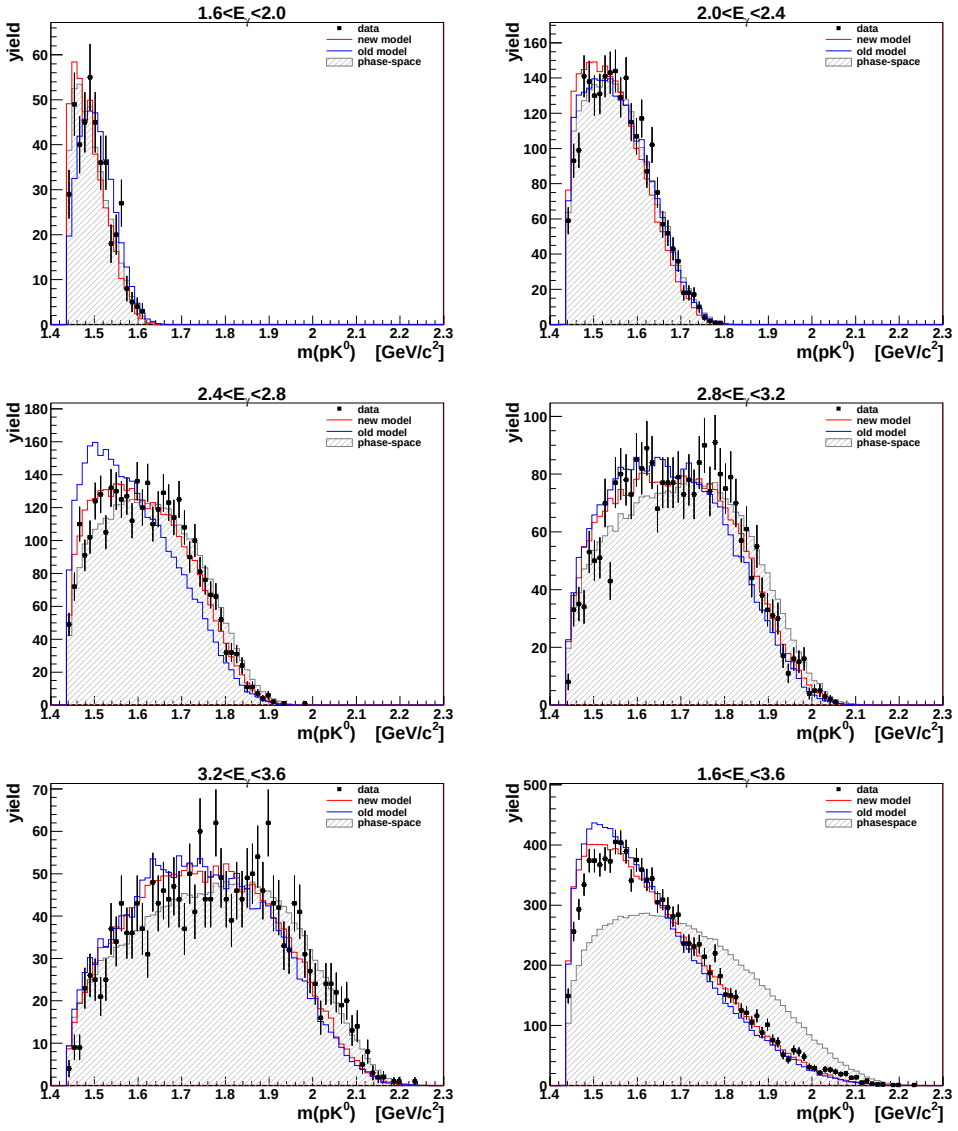

FIGURE 5.56. Invariant mass of the pK^0 system. The three models, "new" (red), "old" (blue), and phase-space (shaded), are corrected by their corresponding acceptances and superimposed.

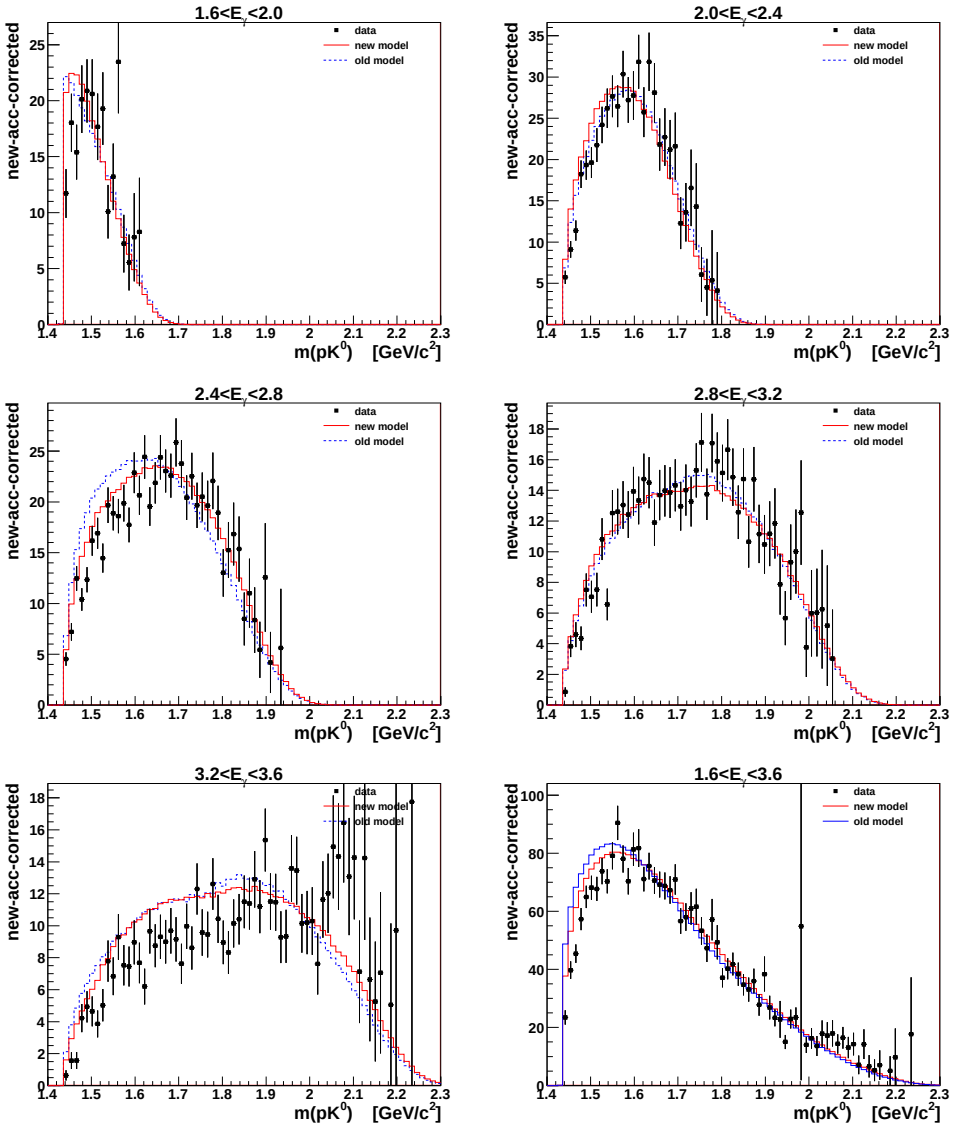

FIGURE 5.57. Invariant mass of the pK^0 system. The data has been corrected by the "new" model acceptance. The "new" (red) and "old" (blue) models are superimposed.

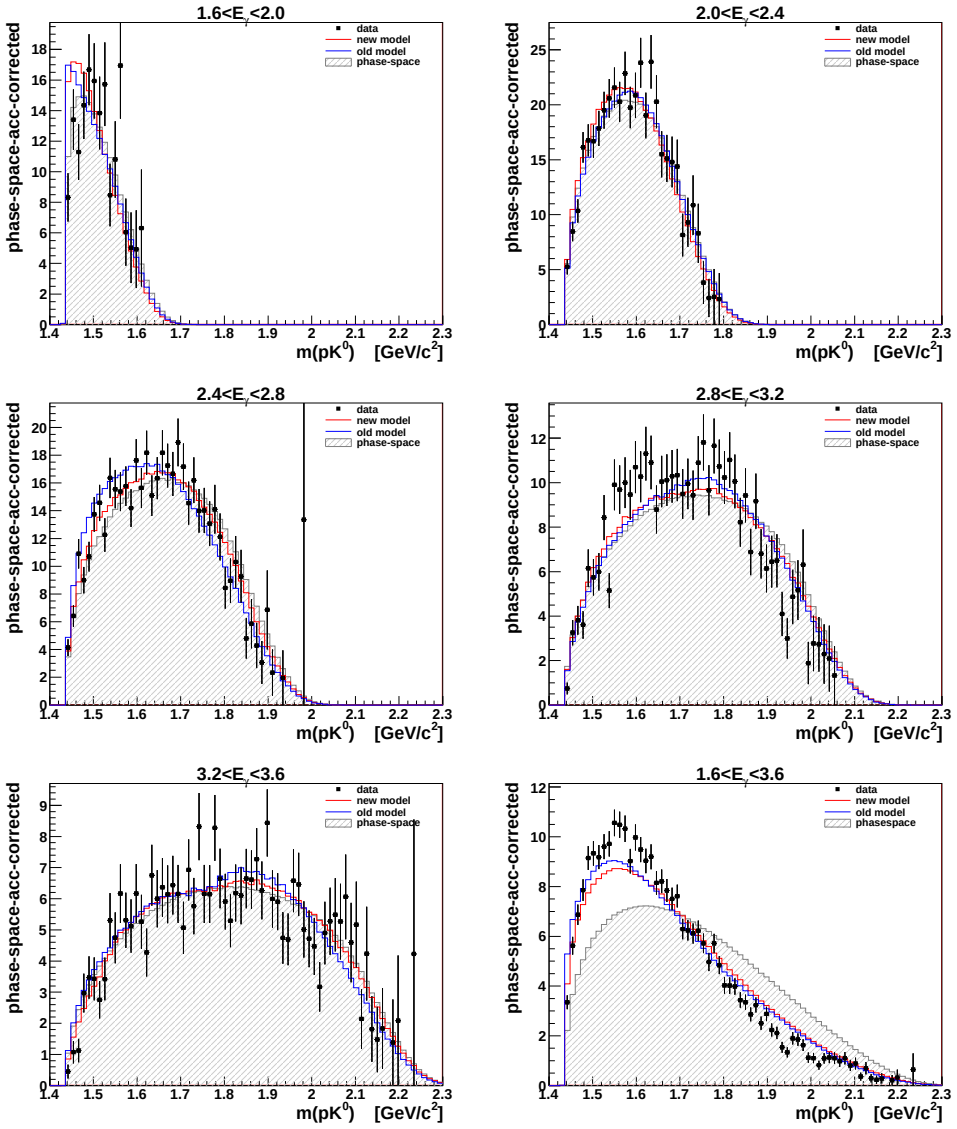

FIGURE 5.58. Invariant mass of the pK^0 system. The data has been corrected by the phase-space acceptance function. The "new" (red), "old" (blue), and phase-space models are superimposed.

CHAPTER 6

UPPER LIMIT

The pK^0 invariant mass spectrum exhibits no evidence of a narrow resonance. With knowledge of the mass resolution, background shape, and efficiency for the reaction in question, an upper limit on Θ^+ production can be calculated. Various methods are used to compute an upper limit.

6.1. MASS RESOLUTION

The detector resolution of the invariant mass of pK^0 is important for estimating the existence of a narrow state in that mass system. The chosen technique uses the width of the $\Lambda(1520)$ as measured in the real data as a reference.

The measured width of $\Lambda(1520)$ is a convolution of its known natural width and the detector resolution, which is assumed Gaussian. A Voigtian, a relativistic Breit-Wigner convoluted with a Gaussian, is fit to the peak in the raw data in Figure 6.1. A polynomial is used as a background under the peak, and the Breit-Wigner mass and width are held fixed. The result is a value for the width of the gaussian, i.e. the detector resolution in the $m(pK^-)$ system. This yields a $m(pK^-)$ mass resolution of 2.5 and 3.5 MeV/c^2 for high and low field settings respectively, and is independent of the order of the background polynomial, as shown in Table 6.1.

TABLE 6.1. Resolution of $m(pK^-)$ measured from the G10 data by fitting the $\Lambda(1520)$ peak with a Voigtian and different order polynomial backgrounds.

	σ [MeV/c^2] (2^{nd} order)	σ [MeV/c^2] (3^{rd} order)	σ [MeV/c^2] (4^{th} order)
$2250A$	3.5 ± 0.9	3.5 ± 0.9	3.5 ± 0.9
$3375A$	2.5 ± 1.9	2.5 ± 1.8	2.5 ± 1.8

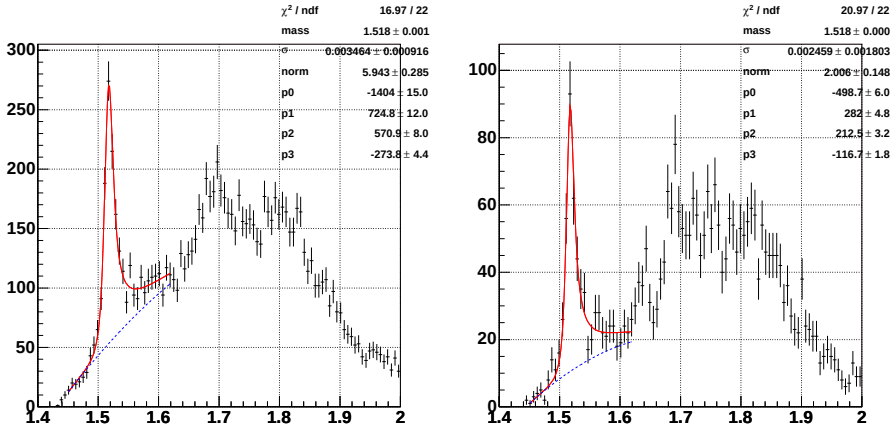

FIGURE 6.1. Voigtian fit to the $\Lambda(1520)$ for $2250A$ (left) and $3375A$ (right) data.

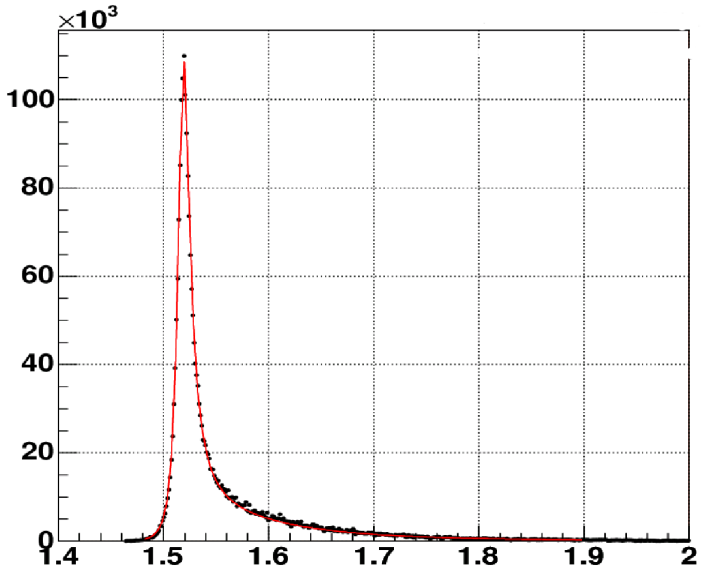

FIGURE 6.2. The invariant mass of the pK^- system. The data points are three-body pK^0K^- phase-space events weighted by a relativistic Breit-Wigner distribution to model the $\Lambda(1520)$ with $l = m = 2$. The red line is a one-dimensional χ^2 fit to the events using the same Breit-Wigner form.

Next, the GPP drift chamber smearing factors are adjusted such that the resolution in simulation for the $m(pK^-)$ system matches that from the data. With that done, the simulation is used to calculate the resolution in the $m(pK^0)$ system in the region of the suspected Θ^+. Phase-space events are generated with a fixed $m(pK^0)$ of $1540\ MeV/c^2$, and the difference between the reconstructed and generated mass is fit with a Gaussian to

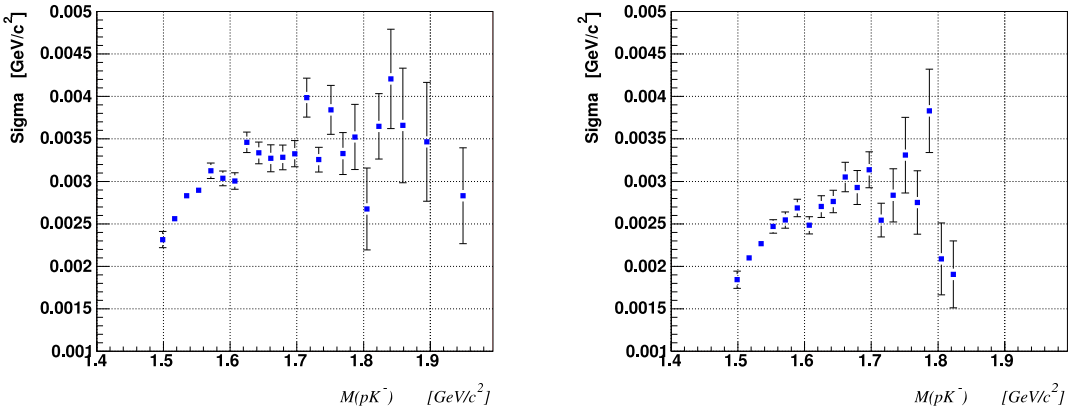

FIGURE 6.3. Sigma of a Gaussian fit to Δm_{pK^-} as a function of m_{pK^-} before and after simulation for $2250A$ (left) and $3375A$ (right) torus settings.

determine the resolution. The results are $m(pK^0)$ resolutions of 2.5 and 3.0 for $3375A$ and $2250A$ respectively.

TABLE 6.2. MC resolution on $m(pK^-)$ when the $\Lambda(1520)$ mass shape is fitted with a pure Voigtian around the peak region only and across the full range, where the Gaussian sigma is in units MeV/c^2 with an uncertainty of $0.2\ MeV/c^2$ for $2250A$ and $0.3\ MeV/c^2$ for $3375A$.

DC-SMEAR	σ_{peak}	σ_{full}	σ_{peak}	σ_{full}
	$2250A$		$3375A$	
1.4	2.7	2.7	2.6	2.7
1.5	2.8	2.8	2.5	2.6
1.7	3.1	3.1	3.8	3.8
1.8	3.2	3.3	3.5	3.5
1.9	3.3	3.3	3.7	3.7
2.0	3.3	3.3	3.8	3.8

TABLE 6.3. MC resolution on $m(pK^-)$ found by fitting the difference between invariant mass before and after simulation, where the uncertainties on sigma from the fit are $(0.1 - 0.4)\ MeV/c^2$ for the slices and very small for the integrated spectrum.

DC-SMEAR	$\sigma\ MeV/c^2$			
	@Λ Mass		Integrated	
	$2250A$	$3375A$	$2250A$	$3375A$
1.7	2.5	2.3	2.9	2.7
1.8	2.6	2.4	3.0	2.8
1.9	2.6	2.4	3.0	2.9
2.0	2.8	2.6	3.2	3.0
2.5	3.1	2.9		

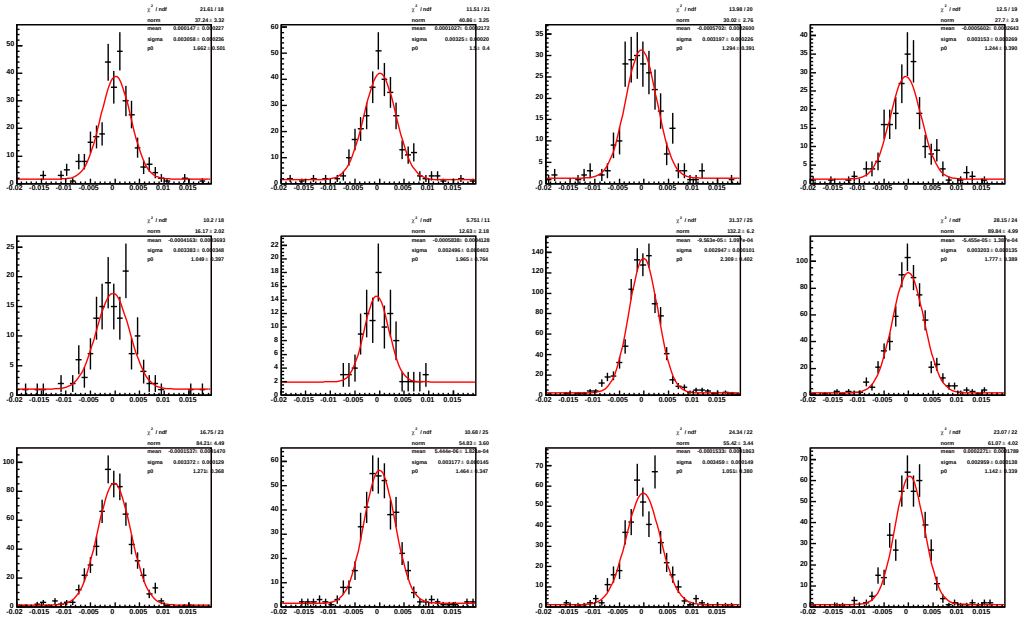

FIGURE 6.4. Example Gaussian fits of Δm_{pK^-} in slices of m_{pK^-}.

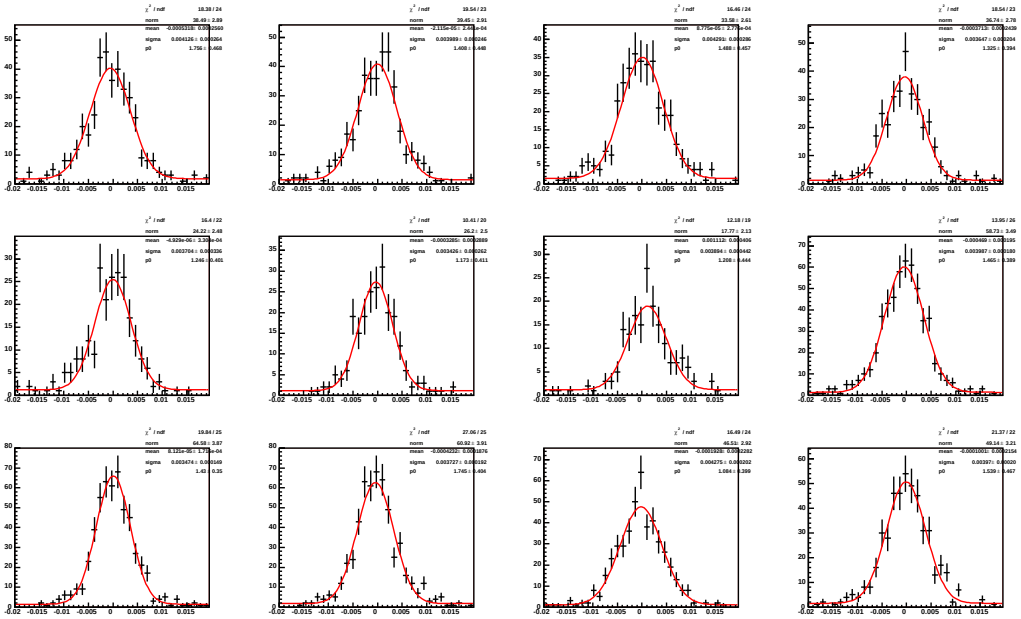

FIGURE 6.5. Example Gaussian fits of Δm_{pK^0} in slices of m_{pK^0}.

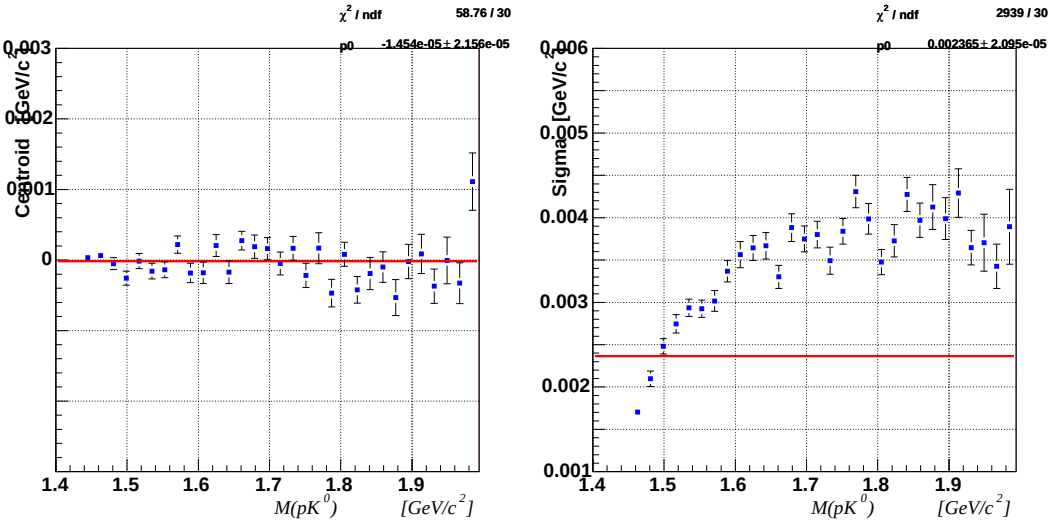

FIGURE 6.6. Sigma and centroid of Gaussian fits to Δm_{pK^0} as a function of m_{pK^0} before and after simulation for $2250A$ torus setting.

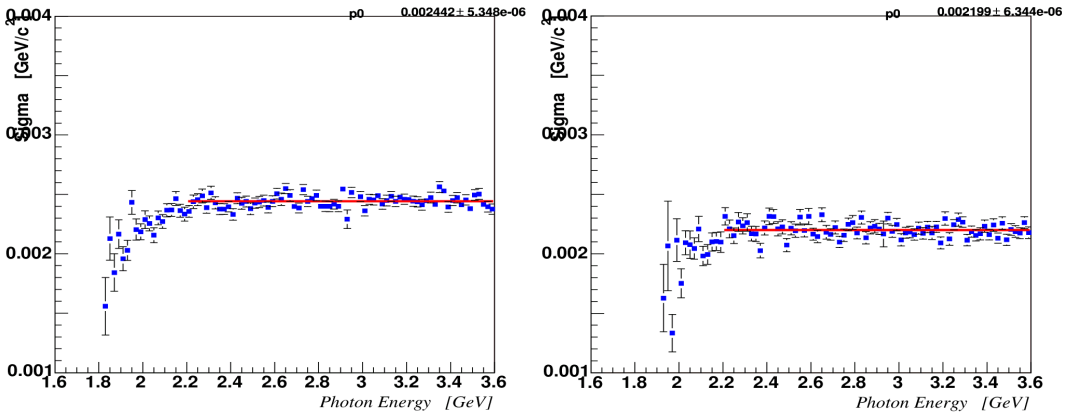

FIGURE 6.7. The resolution of the invariant mass of the pK^0 system as a function of photon energy for $2250A$ (left) and $3375A$ (right) torus settings.

6.2. CROSS SECTION

In order to compare different experiments' results, it is necessary to convert the raw yields into cross section units. The total cross section can be written as:

$$\sigma_{tot} = \frac{N}{\epsilon \cdot \mathcal{L}} \cdot \frac{1}{B} \cdot C_\gamma \tag{23}$$

where N is the number of counts, ϵ is the efficiency, and $\mathcal{L}$ is the luminosity. The parameter B represents the net branching fraction for the decays in the reaction. And, C_γ is the tagger multiplicity factor, which corrects for software event rejection due to multiple beam photons in coincidence. The luminosity can be defined as:

$$\mathcal{L} = \frac{\rho \cdot l \cdot N_A \cdot \gamma}{A} \tag{24}$$

where $A = 2.0140 \ \frac{g}{mol}$ is the atomic mass of the target, $\rho = 0.163 \ \frac{g}{cm^3}$ is the mass density of the target, $l = 24 \ cm$ is the length of the target, N_A is Avagadro's number, and γ is the photon flux. Three decays are involved in the reaction of interest for a total branching fraction of $B = 0.172$.

TABLE 6.4. Three branching fractions in the decay chain $\Theta^+ \rightarrow pK^0 \rightarrow pK^0_s \rightarrow p\pi^+\pi^-$, assuming the Θ^+ would decay exclusively to $N\bar{K}$ with equal probability for nK^+ and pK^0.

B($\Theta^+ \rightarrow pK^0$)	B($K^0 \rightarrow K^0_s$)	B($K^0_s \rightarrow \pi^+\pi^-$)	B(total)
0.50	0.50	0.689	0.172

6.3. GAUSSIAN FIT METHOD

In this method, the upper limit is estimated by fitting the acceptance-corrected data with a Gaussian peak on top of a fixed background shape. The Gaussian approximates a narrow resonance, and the background shape is either the multi-dimensional resonance model or a one-dimensional polynomial. The strength of the Gaussian is the only free fit parameter, while its width is fixed with a σ equal to the detector resolution. The full integral of the Gaussian from $-\infty$ to $+\infty$ is calculated from the resulting fit parameters.

This yield is converted to a 95% confidence level upper limit estimate by adding to it twice its uncertainty.

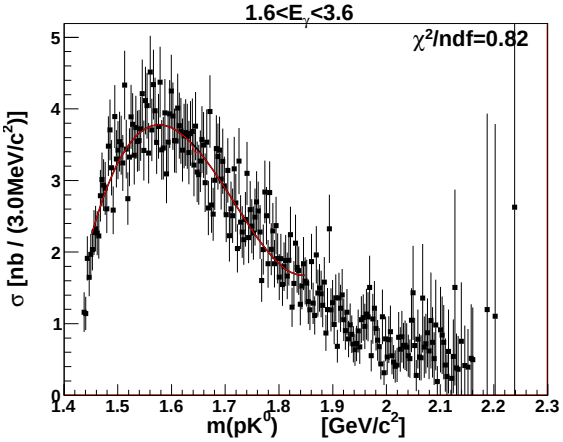

FIGURE 6.8. Example fit of the acceptance-corrected data with the sum of a Gaussian with free normalization and a 5^{th} order polynomial background model.

TABLE 6.5. Gaussian method upper limit in nanobarns on $\gamma d \to \Theta^+ K^-(p)$ for different background shapes and acceptances as a function of photon energy bin..

Back.	Acc	$1.6-2.0$	$2.0-2.4$	$2.4-2.8$	$2.8-3.2$	$3.2-3.6$	$1.6-3.6$
new	new	29.1	18.6	8.6	6.6	4.3	4.7
old	old	11.7	12.2	12.6	4.7	4.2	3.0
poly	new	24.0	12.8	7.8	6.1	6.0	2.9
poly	old	16.3	10.4	6.9	5.3	5.9	3.1

6.4. FELDMAN-COUSINS METHOD

In this method, ROOT's TFeldmanCousins class is used to calculate the upper limit (Brun and Rademakers, 1997). It is an implementation of the statistical methods of Feldman and Cousins (Feldman and Cousins, 1998). The two inputs to the routine are the number of observed events and the expected average background yield. The output is the upper limit on the number of events in excess of the background in a 95% confidence level interval. The number of observed and background events are calculated by integrating the raw data yield and background model. The range of integration is five times the resolution ($\pm 2.5\sigma$)

around the mass value in question. The upper limit returned by the software is converted to a cross-section by treating it as the number of counts in Equation 23.

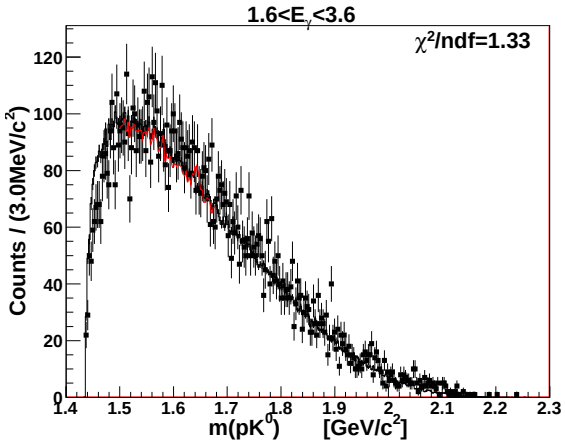

FIGURE 6.9. Example fit of the raw data with the sum of a Gaussian with free normalization and the multi-dimensional background resonance model.

TABLE 6.6. Feldman-Cousins upper limit in nanobarns on $\gamma d \rightarrow \Theta^+ K^-(p)$ for different background shapes and acceptances as a function of photon energy bin.

Back.	Acc.	$1.6-2.0$	$2.0-2.4$	$2.4-2.8$	$2.8-3.2$	$3.2-3.6$	$1.6-3.6$
new	new	19.5	19.6	9.9	6.9	5.8	3.7
old	old	13.2	13.2	14.9	6.0	5.8	3.1
poly	new	15.7	14.5	8.5	6.8	6.3	3.0
poly	old	14.9	12.0	8.2	5.6	6.2	2.8

6.5. SCANNING RESULTS

The upper limit is calculated for both methods as the mass of the hypothetical resonance is scanned across the relevant range (1.5 to 1.68 GeV/c^2). In the Gaussian method, this mass is the centroid of the Gaussian peak; for the Feldman-Cousins method, it is the mid-point of the integration range. The upper limits are plotted in figures Figure 6.10 and Figure 6.11 for two different background shapes: a one-dimensional 5^{th} order polynomial and the multi-dimensional resonance model. For each type of scan, the mass value which maximizes the upper limit is selected. The results are shown in Table 6.5 and Table 6.6.

An upper limit on the reaction $\gamma d \rightarrow \Theta^{+} K^{-}(p)$ is calculated assuming different background shapes, detector acceptances, and mathematical methods. To acccomodate for all systematic uncertainties in the analysis, all the methods are averaged. For the entire integrated photon energy range, 1.6-3.6 GeV, the average upper limit and its standard deviation is $3.3 \pm 0.6\ nanobarns$.

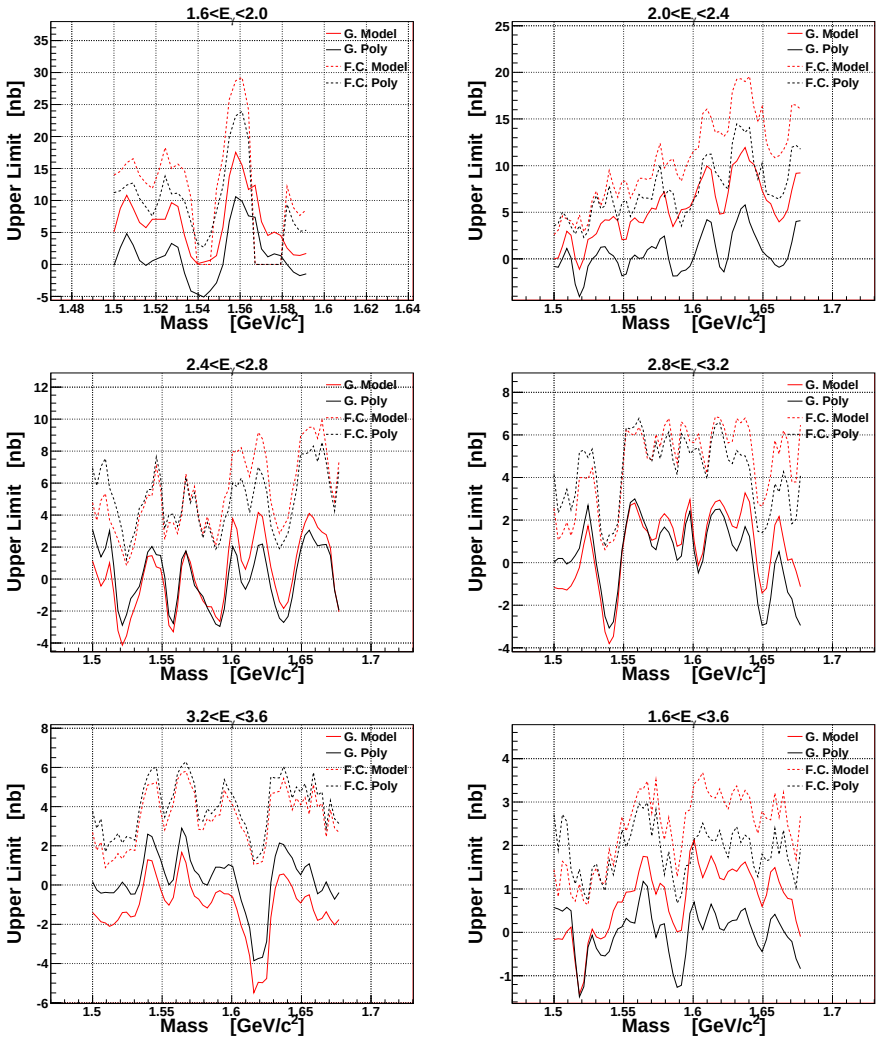

FIGURE 6.10. Upper limit in nanobarns as a function of the invariant mass of pK^0. The Gaussian fits are performed on raw data yields.

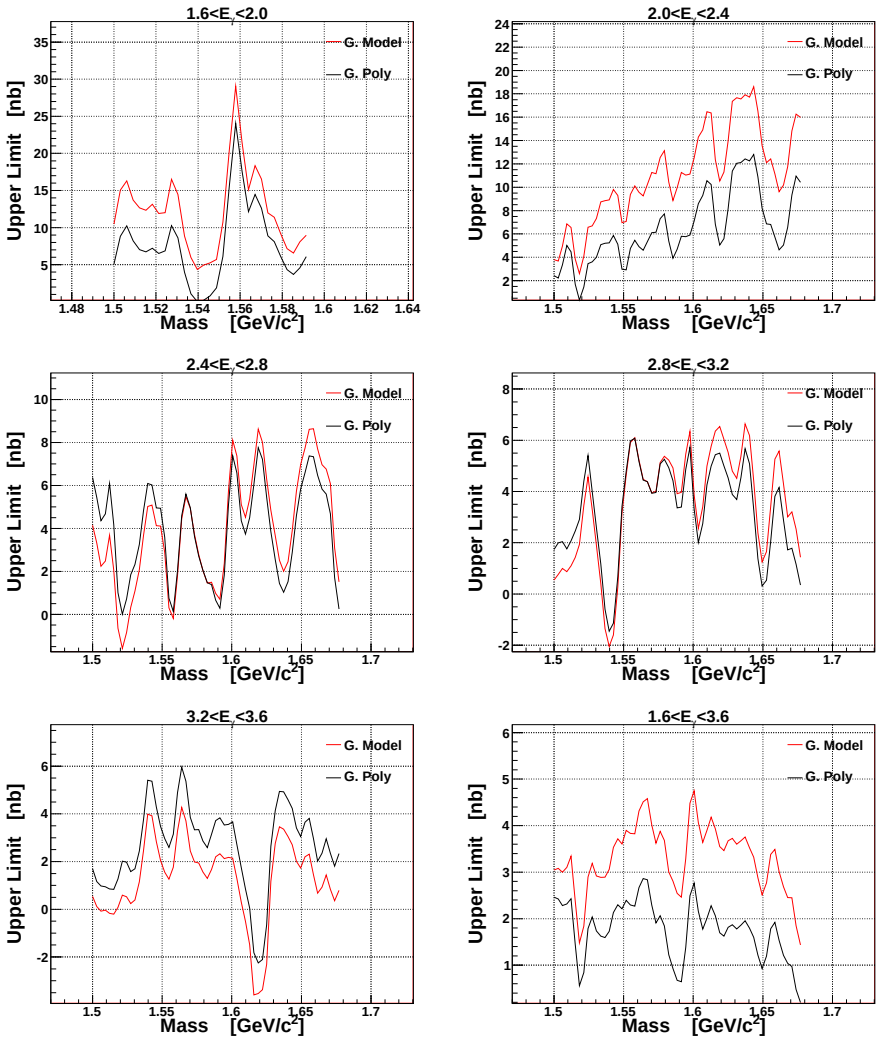

FIGURE 6.11. Upper limit in nanobarns as a function of the invariant mass of pK^0. The Gaussian fits are performed on acceptance-corrected data.

CHAPTER 7

RESULTS AND DISCUSSION

No evidence of the Θ^+ in the pK^0 decay mode is found in this analysis of the reaction $\gamma d \rightarrow ppK^0_s K^-$. The upper limit on the total cross section of the reaction $\gamma n \rightarrow \Theta^+ K^-$ is estimated to be $3.3 \pm 0.6\ nanobarns$ with 95% confidence level in the $m(pK^0)$ mass range 1.5 to 1.68 GeV/c^2. However, the existence of exotic pentaquark states, the Θ^+ included, is not completely definitive. It is necessary to review the world's results, both observations and non-observations.

7.1. POSITIVE Θ^+ EVIDENCE

The published results claiming observation of the Θ^+ are questionable. All suffer severely from low statistics; few have more than 50 signal events. Few claim statistical significance of more than about 5σ, and valid dispute has been raised concerning overestimates (Dzierba et al., 2004). Conclusive evidence would require at least an order of magnitude more statistics.

One observation remains more notable than the others. The LEPS collaboration was the first to publish observation of the Θ^+ in 2003, but their significance of 4.5σ and very low statistics was insufficient. However, since then, LEPS aquired more statistics with the same experimental setup, and, again, found a peak around 1.524 GeV/c^2 in the nK^+ invariant mass spectrum of the reaction $\gamma d \rightarrow K^+K^-np$ shown in Figure 1.5 (Nakano et al., 2009). Unfortunately, the significance of 5.1σ is still inconclusive. But their 279 ± 36 purported Θ^+ events cannot be ignored. In fact, LEPS will be increasing their luminosity by a factor of three in the near future to hopefully resolve the issue.

TABLE 7.1. The world's published positive Θ^+ sightings in both decay modes summarized from (Dzierba, Meyer, and Szczepaniak, 2005) and (Hicks et al., 2005).

Collaboration	Reaction	Decay Mode	N_{Θ^+}	$N_{\Theta^+}/\sqrt{N_{bg}}$
LEPS C_{12}	$\gamma C_{12} \to K^+K^-X$	nK^+	19	4.6
LEPS D_2 (1)	$\gamma d \to K^+K^-np$	nK^+	56	4.4*
LEPS D_2 (2)	$\gamma d \to K^+K^-np$	nK^+	279	5.1
CLAS D_2	$\gamma d \to K^+K^-(n)p$	nK^+	43	5.2 ± 0.6
CLAS p	$\gamma p \to K^+K^-\pi^+(n)$	nK^+	41	7.8 ± 1.0
SAPHIR	$\gamma p \to K^0_sK^+(n)$	nK^+	55	4.8
COSY	$pp \to \Sigma^+K^0_sp$	pK^0_s	57	4-6
JINR	$p(C_3H_8) \to K^0_spX$	pK^0_s	88	5.5
SVD	$pA \to K^0_spX$	pK^0_s	35	5.6
DIANA	$K^+Xe \to K^0_sp(Xe)'$	pK^0_s	29	4.4
ITEP	$\nu A \to K^0_spX$	pK^0_s	18	6.7
NOMAD	$\nu A \to K^0_spX$	pK^0_s	33	4.3
HERMES	quasi-real	pK^0_s	51	$\sim$5
ZEUS (Collaboration, 2004)	$ep \to K^0_spX$	pK^0_s	230	$\sim$5

7.2. NEGATIVE Θ^+ EVIDENCE

Up until the more recent results of the next section, conclusions from the world's experimental searches that did not find evidence of the Θ^+ was far from definitive. For one, few such analyses definitely had the sensitivity to measure the Θ^+ (Hicks et al., 2005). Also, the detector acceptances and event kinematics are very dissimilar between experiments. Only one non-observation had a photon and hadron in the initial state, in contrast to the published Θ^+ sightings. All the non-observations were inclusive searches with missing, unkown particles. Therefore, the strangeness of the neutral kaon, as well as the exotic nature of the pK^0 system, was unknown.

7.2.1. Latest Results from CLAS. Since the inception of this study, the CLAS collaboration has published four null searches in photoproduction data dedicated at ending the confusion over the existence of the Θ^+. All resulted in upper limits on Θ^+ production in their respective channels of a few nanobarns, shown in Table 7.3. The γd channels use the

TABLE 7.2. The world's negative Θ^+ searches summarized from (Dzierba, Meyer, and Szczepaniak, 2005) and (Hicks et al., 2005).

Collaboration	Reaction	Upper Limit
BES	$e^+e^- \rightarrow J/\Psi \rightarrow \Theta\Theta$	$< 1.1 \times 10^{-5}$ B.R.
BaBar	$e^+e^- \rightarrow \Upsilon(4S) \rightarrow pK^0X$	$< 1.0 \times 10^{-4}$ B.R.
Belle	$e^+e^- \rightarrow B^0\bar{B}^{\rightarrow}p\bar{p}K^0X$	$< 2.3 \times 10^{-7}$ B.R.
LEP	$e^+e^- \rightarrow Z \rightarrow pK^0X$	$< 6.2 \times 10^{-4}$ B.R.
HERA-B	$pA \rightarrow pK^0X$	$< 0.02 \times \Lambda*$
SPHINX	$pC \rightarrow K^0\Theta^+X$	$< 0.1 \times \Lambda*$
HyperCP	$pCu \rightarrow pK^0X$	$< 0.003 \times pK^0$
CDF	$p\bar{p} \rightarrow pK^0X$	$< 0.03 \times \Lambda*$
BeO	$\gamma BeO \rightarrow pK^0X$	$< 0.02 \times \Sigma*$
Belle	$\pi + Si \rightarrow pK^0X$	$< 0.02 \times \Lambda*$

same data set as this analysis. The results from all channels are derived from a combination of parallel analyses using the same Feldman-Cousins statistical techniques employed in this work.

Since these results from CLAS use similar experimental conditions and the same detector system, consistency between the different channels' upper limits is expected. The stricter limits for the γp reactions are due primarily to luminosity differences resulting from a much longer target and larger beam flux. In the case of the Λ channel, the two body reaction gives more sensitivity to the detector acceptance and background model, hence the larger upper limit. And, the acceptance is considerably lower for the $\gamma d \rightarrow ppK^0_sK^-$ than $\gamma d \rightarrow npK^+K^-$ due to the detection of an additional particle. The same can be said in comparing the two-K^0 and one-K^0 final states off the proton.

It should be noted that there is, unfortunately, very little overlap between the kinematic acceptance of the LEPS and CLAS detector systems. The majority of events measured by LEPS in their Θ^+ sightings would have exited down the CLAS beam line. It is possible that severe production kinematics could prevent CLAS from seeing the Θ^+ at all. Furthermore, the CLAS analysis requires a final state rescattering for the proton, and so the elementary cross section requires a model dependent extrapolation. As a result, CLAS having exclusively measured the same reaction with larger statistics but a null result does not invalidate the LEPS signal.

TABLE 7.3. Upper limit summary of reactions measured with CLAS using high statistics data dedicated to Θ^+ search. The result of combining the two proton reactions gives an upper limit of 0.7 nb on $\gamma p \to \Theta^+ \bar{K}^0$.

Reaction	Decay Mode	Upper Limit $[nb]$	Reference
$\gamma p \to nK^+K^0$	nK^+	1.3	(DeVita et al., 2006)
$\gamma p \to pK^0\bar{K}^0$	pK^0	2.5	(DeVita et al., 2006)
$\gamma d \to \Lambda nK^+$	nK^+	5-25	(Niccolai et al., 2006)
$\gamma d \to npK^+K^-$	nK^+	3.0	(McKinnon et al., 2006)
$\gamma d \to ppK^0_sK^-$	pK^0	3.3	this work

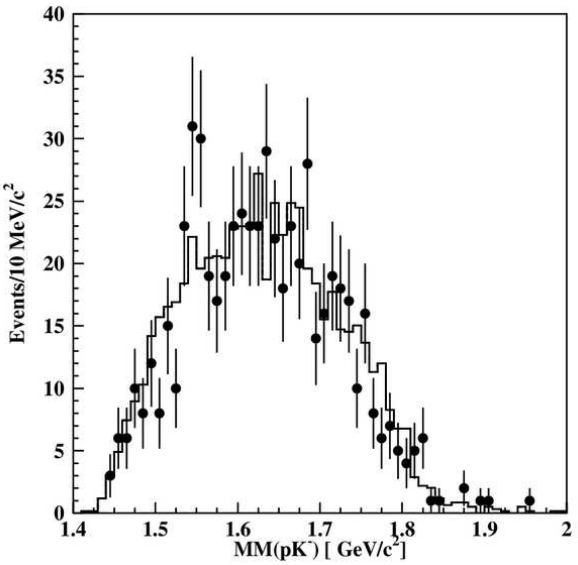

FIGURE 7.1. The CLAS collaboration published a revised analysis of new $\gamma d \to pnK^+K^-$ data (represented by sold line and scaled to the initial publication) in search of $\Theta^+ \to nK^+$.

7.3. COMPARISON WITH THEORY

There are a few theoretical publications reporting cross-sections for Θ^+ photoproduction off neutrons and protons. One estimate uses the isobar and Regge approaches to calculate the cross-section for photoproduction of the Θ^+ off the neutron. The published results are $\sim 100\ nb$ and $< 100\ nb$ for the two models, respsectively (Mart, Salam, Miyagawa, and Benhold, 2004). These predictions are clearly in disagreement with the upper limits measured in this analysis and the others published by CLAS.

A phenomological Lagrangian approach is also considered. It resulted in total cross-sections off the neutron of 1.8-5.9 $nanobarns$, depending on the spin and parity of the Θ^+

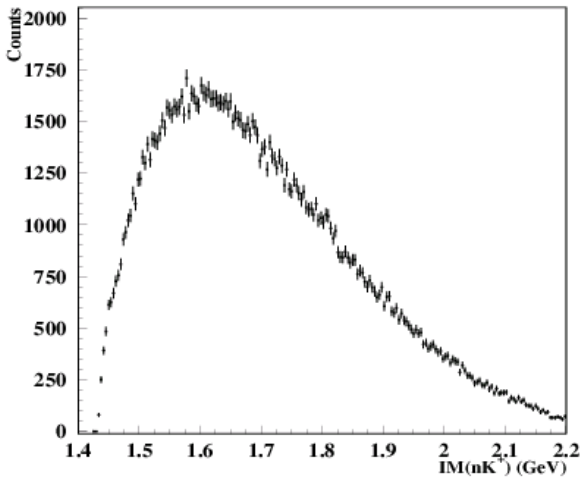

FIGURE 7.2. The CLAS collaboration's high-statistics measurement of $\gamma p \to \bar{K}^0_s K^+ n$ in search of $\Theta^+ \to nK^+$.

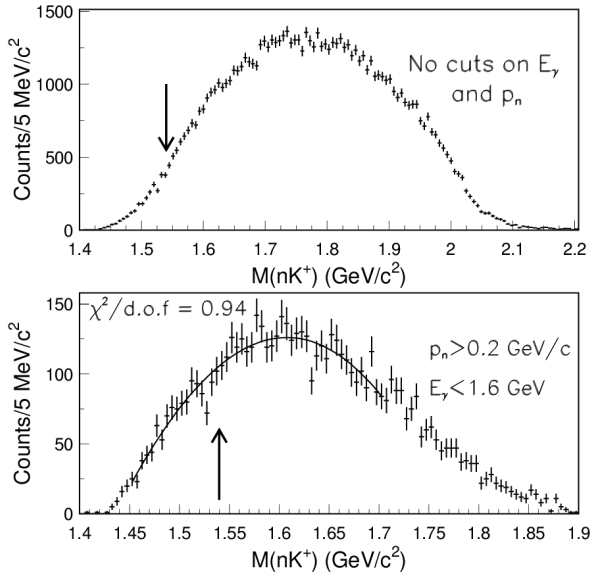

FIGURE 7.3. The CLAS collaboration's high-statistics measurement of $\gamma d \to \Lambda n K^+$ in search of the Θ^+.

(Roberts, 2004). The results from the work presented here are not in disagreement with this prediction.

Another Lagrangian calculation of the Born diagrams found cross-sections of 25 nb for $J^\pi = \frac{3}{2}^+$, 200 nb for $\frac{3}{2}^-$, and 1 nb for $\frac{1}{2}^+$ (Nam, Hosaka, and Kim, 2005). Given these theoretical predictions, if the Θ^+ does exist, it is most likely spin-$\frac{1}{2}$ with positive parity.

The comparisons between experimental and theoretical data are indecisive. The models' predictions range from few-nb to hundreds of $nanobarns$. All the recent experimental upper limits are of the order of a few $nanobarns$. The current experimental upper limits on Θ^+ production from CLAS cannot entirely refute all the theoretical predictions.

7.4. CONCLUSION

A null search has been made for the Θ^+ pentaquark. With strangeness $+1$ and minimal quark content $uudd\bar{s}$ in a constituent model, it is a manifestly exotic baryon. Using quasi-free photoproduction off a neutron, the channel $\gamma d \rightarrow ppK^0K^-$ is analyzed for evidence of $\gamma n \rightarrow \Theta^+K^-$ and the decay $\Theta^+ \rightarrow pK^0_s$. The CLAS detector system, with 1.6-3.6 GeV tagged photons and nearly 4-π acceptance for charged particles, can exclusively reconstruct the channel over a large range of kinematics. A background model has been developed based upon Breit-Wigner distributions for known mesons and baryons and used to describe the data with an unbinned maximum likelihood fit. No statistically significant evidence of an exotic baryon is found. An upper limit on the total cross section of $\gamma d \rightarrow \Theta^+K^-(p)$ in the photon energy range $1.6 - 3.6\ GeV$ of $3.3 \pm 0.6\ nb$ is estimated using different background models and statistical techniques.

The question over the existence of the exotic Θ^+ pentaquark is not entirely answered. As more data is acquired around the world, stricter upper limits are placed on its production. The excitement of 2003 due to a few theoretical predictions and experimental observations has diffused. Many of the positive sightings have been superceeded by dedicated high statistics experiments, yet at least one notable exception remains. This analysis is one of numerous null searches that have contributed.

BIBLIOGRAPHY

G. D. Abrams et al. *Phys. Rev. Lett.*, 13:670, 1964.

C. Amsler et al. *Phys. Lett. B*, 677:1, 2008.

A. E. Asratyan, A. G. Dolgolenko, and M. A. Kubanstev. *Phys. At. Nucl.*, 67:682, 2004.

Ya. I. Azimov and I. I. Strakovsky. *arXiv:hep-ph/0406312*, 2004.

N. Baltzell. *http://www.jlab.org/hall-b/secure/g10/baltzell/eloss*, 2005.

V. V. Barmin et al. *Yad. Fiz.*, 66:1763, 2003.

V. E. Barnes et al. *Phys. Rev. Lett.*, 12:204, 1964a.

V. E. Barnes et al. *Phys. Lett.*, 12:134, 1964b.

J. Barth et al. *Phys. Lett. B*, 572:127, 2003.

R. Brun and F. Rademakers. *Nucl. Inst. & Meth. in Phys. Res. A*, 389:81, 1997.

S. U. Chung. *Phys. Rev. D*, 48:1225, 1993.

The ZEUS Collaboration. *Phys. Lett. B*, 591:7, 2004.

R. DeVita et al. *Phys. Rev. D*, 74:032001, 2006.

R. Diakonov, V. Petrov, and M. Polyakov. *Z. Phys. A*, 359:305, 1997.

A. R. Dzierba, C. A. Meyer, and A. P. Szczepaniak. *J. Conf. Ser.*, 9:192, 2005.

A. R. Dzierba et al. *Phys. Rev. D*, 69:051901, 2004.

S. Eidelman et al. *Phys. Lett. B*, 592, 2004.

G. Feldman and R. Cousins. *Phys. Rev. D*, 57:3873, 1998.

M. Gell-Mann. *Phys. Rev.*, 125:1067, 1962.

M. Gell-Mann. *Phys. Lett.*, 8:214, 1964.

L. Glozman and D. Riska. *Phys. Rep.*, 268:263, 1996.

O. W. Greenberg and D. Zwanziger. *Phys. Rev.*, 150:1177, 1966.

D. J. Gross and F. Wilczek. *Phys. Rev. D*, 8:3633, 1973.

F. Gursey and L. Radicati. *Phys. Rev. Lett.*, 13:173, 1964.

M. Y. Han and Yoichiro Nambu. *Phys. Rev. B*, 139:1006, 1965.

K. Hicks et al. *Prog. Part. Nucl. Phys.*, 55:648, 2005.

N. Isgur and G. Karl. *Phys. Rev. D*, 18:4187, 1978.

R. Jaffe. *Phys. Rev. Lett.*, 38:195, 1976.

R. Jaffe. *Phys. Rev. D*, 15:267, 1977a.

R. Jaffe. *Phys. Rev. D*, 15:281, 1977b.

R. Jaffe and F. Wilczek. *Phys. Rev. Lett.*, 91:232003, 2003.

F. James and M. Roos. *Computer Physics Communications*, 10:6, 1975.

M. Jezabeck and M. Praszalowicz. *World Scientific*, 112, 1987.

M. Karliner and H. J. Lipkin. *Phys. Lett. B*, 575:249, 2003.

M. Karliner and P. Mattis. *Phys. Rev. D*, 34:1991, 1986.

V. Kubarovsky et al. *Phys. Rev. Lett.*, 92:032001, 2004.

D. B. Lichtenberg. *Phys. Rev.*, 178:2197, 1969.

H. Lipkin. *Phys. Lett. B*, 172:242, 1986.

T. Mart, A. Salam, K. Miyagawa, and C. Benhold. *arXiv:nucl-th/0412095*, 2004.

B. McKinnon et al. *Phys. Rev. Lett.*, 96:212001, 2006.

T. Mibe, M. Mirazita, and N. Baltzell. *http://www.jlab.org/Hall-B/secure/g10*, 2005.

T. Nakano et al. *Phys. Rev. Lett.*, 91:012002, 2003.

T. Nakano et al. *Phys. Rev. C*, 79:025210, 2009.

Seung-Il Nam, Atsushi Hosaka, and Hyun Chul Kim. *arXiv:hep-ph/0505134*, 2005.

S. Niccolai et al. *Phys. Rev. Lett.*, 97:032001, 2006.

M. Praszalowicz. *Phys. Lett. B*, 575:236, 2003.

W. Roberts. *Phys. Rev. C*, 70, 2004.

K. Schilling, P. Seyboth, and G. Wolf. *Nucl. Phys. B*, 15:397, 1970.

T. H. Skyrme. *Proc. Soc. Lond. A*, 260:1975, 1961.

T. H. Skyrme. *Nucl. Phys.*, 31:556, 1962.

Fl. Stancu and D. O. Riska. *arXiv:hep-ph/030701*, 2003.

S. Stepanyan et al. *Phys. Rev. Lett.*, 91:252001, 2003.

S. Stepanyan et al. *Nucl. Instrum. Methods A*, 572:654, 2007.

D. Strottman. *Phys. Rev. D*, 20:748, 1979.

E. Witten. *Nucl. Phys. B*, 223:433, 1983a.

E. Witten. *Nucl. Phys. B*, 223:422, 1983b.

G. Zweig. *CERN-8182-TH-401*, 1964.